© Copyright 2016

Md Golam Rabbani

Modeling and characterization of photoresponse of nanowires with asymmetric contacts and bending strain

Md Golam Rabbani

A dissertation

submitted in partial fulfillment of the

requirements for the degree of

Doctor of Philosophy

University of Washington

2016

Reading Committee:

Manjeri P. Anantram, Chair

Robert Bruce Darling

Lih Y. Lin

Program Authorized to Offer Degree:

Electrical Engineering

University of Washington

Abstract

Modeling and characterization of photoresponse of nanowires with asymmetric contacts and bending strain

Md Golam Rabbani

Chair of the Supervisory Committee:
Professor Manjeri P. Anantram
Electrical Engineering

This work investigates (i) contact asymmetry induced response of semiconductors, with emphasis on nanowire photo response, and (ii) strain induced electronic and optoelectronic properties of narrow silicon nanowires. Contact area asymmetry is shown to produce large zero-bias photo response in bulk silicon, which is explained by TCAD modeling. Modeling also shows that both short circuit current and open circuit voltage in nanowire solar cells and photo sensors can be enhanced by using contact metals with large work function difference. This does not need any p-n junction type asymmetric band structure device that requires high and controlled doping. However, two-contact large nanowires are found to suffer from low current density due to minority carrier recombination and inefficient carrier collection at contacts. As a solution, multi-contact and grounded-gate designs are modeled and found to enhance photo response. By simple fabrication and characterization, we show that nanowire networks with dual-metal contacts produce large photo currents. Interestingly, a sparse network gives larger response than a relatively dense network. High resistance nanowire-nanowire contact is shown to place a limit on electrical transport and explains such unintuitive response. Finally, Molecular dynamics and quantum mechanical transport simulation of bent narrow silicon nanowires show that bending strain causes larger decrease in transmission gap compared to the usually investigated uniaxial strain and that a moderate amount of bending strain may be capable of causing a semiconductor to metal transition.

TABLE OF CONTENTS

LIST OF FIGURES

LIST OF TABLES

ACKNOWLEDGEMENTS

I am grateful to my advisor, Professor Manjeri P. Anantram, for his guidance, encouragements as well as support throughout my doctoral study. His vast knowledge, great courses, and attention to details have helped my research move forward and be less error prone.

I would like to thank Professors R. Bruce Darling and Lih Y. Lin for serving in my reading committee. Professor Darling has also been a great help throughout my PhD study in UW by sharing his vast knowledge, teaching me device and fabrication, and allowing me access to his lab. In addition to teaching two valuable courses, Professor Lin has often lent helping hands with access to her lab and instruments.

I am fortunate to have had an impressive list of collaborators: Professors Amit Verma, Reza Nekovei, and Mahmoud Khader. Professor Verma's constant interest, motivation and support helped me move ahead during rough periods in my research. Professor Nekovei provided important characterization instrument. Professor Khader made great efforts so that I had had access to useful instruments. I thank also Professor Brian Korgel and Julian Villarreal from UT Austin for providing nanowires and helps in improving a research paper. I highly appreciate help and guidance from Professor Sunil Patil of Pune College of Engineering.

I thank National Science Foundation and QNRF for generously supporting my research.

My research was partly carried out in EE fabrication and characterization lab, Washington Nanofabrication Facility and Molecular Analysis facility. My thanks go to the helpful staffs in

these facilities. I will be forever indebted to EE department and its staffs and the UW as a whole for my happy and fruitful time in Seattle.

Finally, I thank my family for their love, support and sacrifice. My mother was not pleased with my leaving Bangladesh for my PhD but would be so happy when I would call her on phone. Unfortunately, she suddenly passed away while I was so far away from her. I love you Ma and miss you every single day. My father has had to work really hard to raise my brother and me. He always believed in me and my education. I hope to be as good a father as he is. My wife, Sheuli, has taken care of my whole family, always encouraged me, and reminded me of how important it was to not give up when I was down. My son, Anubhav, has been a great source of joy. Every day I look forward to returning home for his welcoming smile and hug. He is my sweetheart #0-13.

DEDICATION

To the loving memory of my mother.

Chapter 1. INTRODUCTION

Over the past two decades, semiconductor nanowires have received widespread attention in nanoscale research areas such as nano-electronics and nano-photonics. Nanowires can function as miniaturized devices as well as electrical interconnects. As such, they are being considered as important building blocks in nanotechnology. They have unique shapes, sizes, compositions, chemical and physical properties, which can now be controlled with relative ease as a result of worldwide efforts in nanomaterials research. Their high aspect ratio allows the bridging of the nanoscopic and macroscopic worlds, which is fundamental to the integration of electronics and photonics.

Bulk silicon is the most widely used semiconductor in electronics and photovoltaics. Recently, silicon nanowire has also been established as a major player in nanotechnology. The nanowires can be fabricated in both top-down and bottom-up approaches, and have been fabricated in a range of diameters, from a few nanometers to a few hundred nanometers. Due to its indirect band gap, bulk silicon's photo absorption efficiency is low. Hence a thick film of silicon is necessary for the complete absorption of solar spectrum. Thick film requires more materials and increases the associated material cost. However, silicon nanowires (SiNWs) have been found to have a considerably improved light absorption property [1]–[6]. Since a smaller amount of material (i.e. nanowires) can absorb a larger fraction of the incident light, this may result in huge saving in the material cost. SiNWs are thus very promising for photosensing and photovoltaic applications, and have already been used in many photodetectors [7]–[10] and solar cells [1], [3], [11]. In addition to SiNWs, our results are relevant to other nanowires in general and we have also studied germanium nanowires (GeNWs).

Many of the improved properties of nanowires have been attributed to their having a large surface to volume ratio [12]–[16]. However, the large surface is also often associated with a large surface roughness [17], [18], which increases scattering and thereby degrades thermal and electrical mobility, and reduces carrier lifetime (or diffusion length). Low minority carrier lifetime (diffusion length) is a big issue in the photosensing and photovoltaic applications of nanowire devices because the collection of the photo generated carriers, hence the efficiency, in such devices is greatly reduced. This issue can be alleviated through improved device designs, such as using a core-shell structure [11], [19], [20] instead of an axial device. I present a distributed contact design to increasing the photo generated carrier collection, especially in long nanowires, as discussed in Chapter 3. The distributed contacts divide a long (compared to the carrier diffusion length) nanowire into many small wires in parallel, and improve both short circuit current and open circuit voltage.

Some sort of asymmetry in the device improves the carrier collection efficiency as photo generated electrons can flow towards one contact while holes flow towards the other. The usual approach to introducing asymmetry is through the formation of a p-n junction by doping [21]–[23]. Achieving a precisely controlled doping in nanodevices is, however, difficult [24]–[27]. As a solution, we show that appropriately chosen metal pairs (that is, metal contacts having sufficient work function difference) can achieve the same performance as a p-n junction type device without any need for large and controlled doping densities. In such a design, compared to the nanowire work function, one contact has a higher work function while the other contact has a lower work function. We develop a guideline for choosing the metal pair which has the required work function asymmetry and avoids deleterious effects such as reduction of minority carrier lifetime.

Study of very narrow silicon nanowires have revealed that, unlike bulk silicon and wide nanowires, they have a direct bandgap [28], [29], which is essential for efficient light absorption and emission. More importantly, it has also been found [30] that mechanical strain can change the amount of bandgap and turn a direct bandgap semiconductor into an indirect bandgap semiconductor, and vice versa. These results are very promising for optoelectronic applications of SiNWs, such as for fabricating tunable lasers. So far, strain dependent electronic studies of nanowires have exclusively focused on uniaxial strain, despite most real nanowires having some bending inherently present in them. Such as, bottom up synthesized nanowires are usually not perfectly straight, rather they are twisted as well as jumbled [31], [32]. In reference [33], Bertagnolli grew wires with a predefined rectangular shape. Zhu et al. [34] demonstrated over 40% bending strain in nanowires with tungsten tip. In an ultimate bending strength experiment, Cook *et al.* [35] bent silicon nanowires lying on a flat substrate through sequential atomic force microscope (AFM) tip manipulations. They could get a U-shape bending, and found that, as diameter decreased, the amount of bending that the nanowires could withstand before breaking increased. This might mean that the narrower nanowires are more stable under larger bending stresses. Although these bending studies have been done mostly on bottom up nanowires, even top-down fabricated nanowires can be bent intentionally [36], [37] or unintentionally [38], [39]. Moreover, top down and bottom up approaches can be combined [40] to get horizontally suspended, well-oriented and size-controlled nanowire arrays. Due to bending, as opposed to uniaxial straining, different atoms in the nanowire are under different amount of strain. This may open up new possibilities, and electronic and optoelectronic studies of bent wires are necessary.

In view of the opportunities and challenges discussed above, we study the response of nanowires to light as well as to strain. Figure 1.1 below lists the exploration paths as well as the application areas of this work. The targeted fields are photodetection, photovoltaic and strain dependent electro-optic devices. In these areas, we explore how asymmetry - in both size and work function - in device metal contact affects device characteristics under light. We show that, depending on the nanowire length, the optimum number of contacts may be different for efficient carrier collection. Besides single nanowires, devices consisting of nanowire networks are relatively easier to fabricate. Our investigation shows that they produce considerable amount of photo response which depends on network density in an unintuitive way. Role of strain in modifying electrical properties, such as bandgap, conductivity, are also to be studied through simulations.

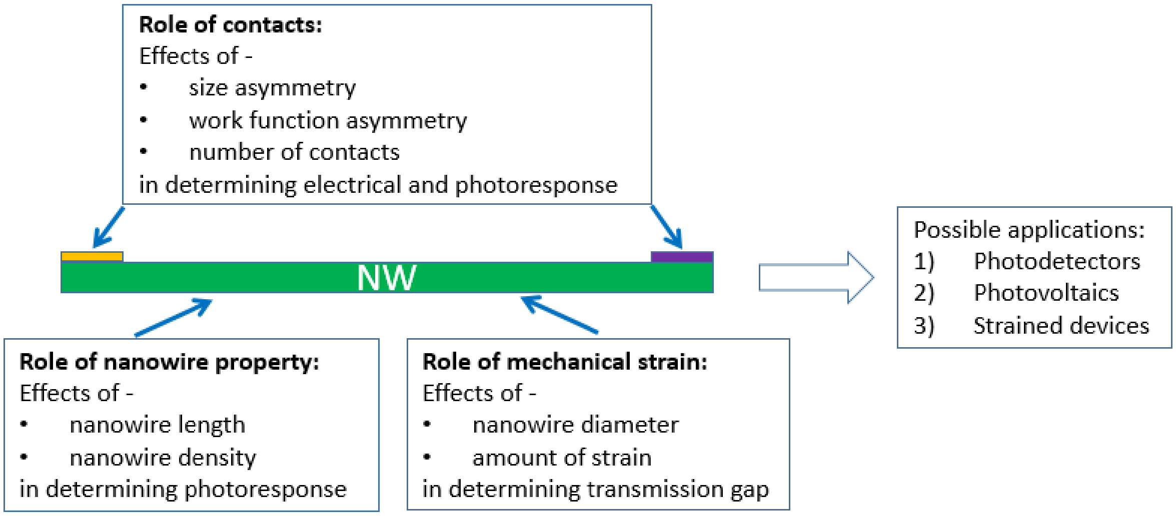

Figure 1.1. Paths of exploration of this work.

Figure 1.2 schematically specifies the various components of the proposed work. In Figure 1.2(a), a nanowire is lying on an insulating substrate. The substrate mainly provides mechanical support. There is one metal contact on each of the two ends of the nanowire. This device is also assumed to be in the dark (no light) condition. Such is the reference device. The other parts of

Figure 1.2 all show some particular changes with respect to the reference device. Figure 1.2(b) turns on illumination. Figure 1.2(c) depicts the case with a different metal for the second contact while the nanowire is under illumination. The nanowire is under strain in Figure 1.2(d).

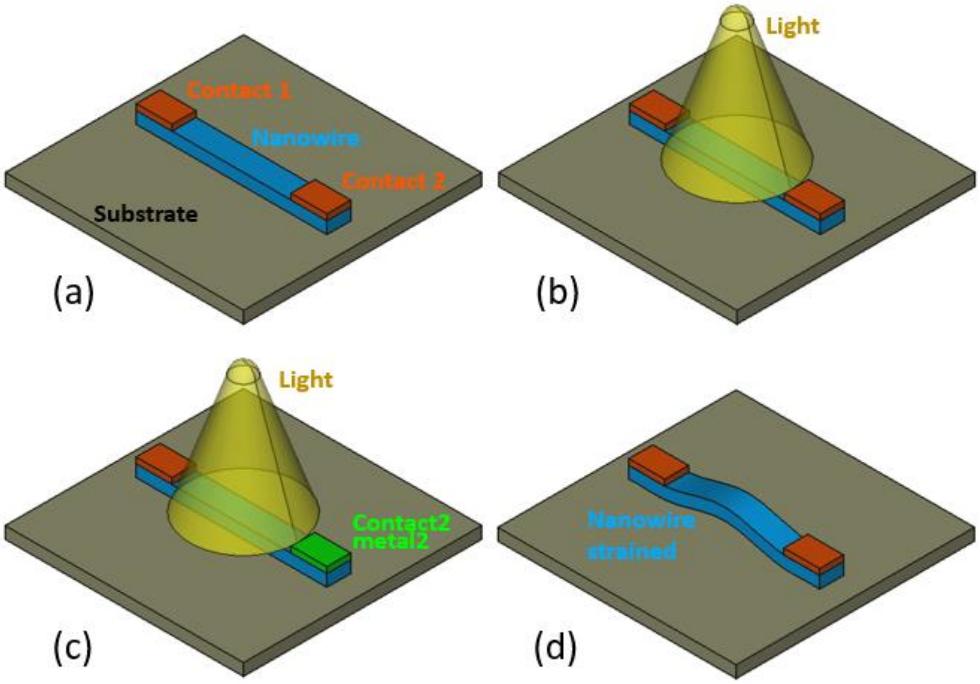

Figure 1.2. Graphical representation of various components of the work.

The major divisions of this work are briefly touched upon in the following sections. Later chapters will have more on each of these.

1.1 ASYMMETRIC CONTACT SILICON PHOTO SENSOR

Although we will be mostly dealing with nanowires in this study, first, we want to present some interesting results from metal-on-bulk-silicon based photo sensors. Sensing of light is useful in numerous fields such as radiation detection, smoke detection, flame detection, street light switching, atomic force microscopy, security alarm, etc. This is a mature field, and there exist various device designs for realizing a photo sensor. Some examples are photodiode, avalanche photodiode, PIN photodiode, Schottky diode, phototransistor, and photomultiplier. In the very first of our experimental processes, we fabricated metal-semiconductor-metal (MSM) devices with only a single metal deposited on bulk silicon with native oxide. Such simpler devices can have significant dark leakage suppression [41] and our measurements also reveal that they can have large photocurrent response, even at zero bias. We show that asymmetry in the physical size of, and asymmetry in the light position relative to, the metal contacts are the bases for such excellent photosensing device. Its fabrication process is very simple and low cost. At the same time, its output photocurrent is large. In Chapter 2, I detail this photo sensor's theory and fabrication along with the experimental results.

1.2 LIGHT-NANOWIRE INTERACTION

Due to its indirect band gap, bulk silicon's photo absorption efficiency is low. However, silicon nanowires have been found to have a considerably improved light absorption property. This is very promising for photosensing and photovoltaic applications. These fields are recently seeing huge research efforts, and there are also increased government subsidies for designing low cost solar cells. Taking these as motivations, we have simulated both short circuit current and open circuit voltage of nanowire based photo sensing devices. A simple device with dual-metal contacts has been studied. Detailed understanding of the influence of wire dimensions, minority carrier lifetimes, and metal work functions on the optical characteristics has been made. Based on our findings, we put forth guidelines for choosing the contact metals for higher output efficiency. Distributed electrode structure has also been shown to increase the short circuit current of long wires and improve their current density.

Experimental realization of the modeled device has also been done. First simple metal depositions are performed to fabricate ‘oxide test benches’, each with lines of two different metals forming gaps on an oxide wafer. Next a nanowire suspension is drop casted on the metal gaps in the oxide test bench. This deposits a nanowire network which bridges the two metals and forms a device. Current—voltage and photo switching measurements are done and an appreciable photo response is achieved. When nanowires are longer than the metal gap size, sparse network gives larger current than a relatively denser network. We consider details of electronic transport toe explain such unintuitive phenomenon. We have studied both GeNW and SiNW networks to show that the results are quite general.

1.3 PROPERTIES OF BENT SILICON NANOWIRES

A strained semiconductor device can have many useful electronic and optoelectronic properties. Strained bulk silicon has higher electron and hole mobilities [42], [43], which has been found to improve the switching speed of the transistors. It has also been predicted [30] that strain can change both size and directness (or indirectness) of the bandgap of narrow silicon nanowires. Such a property may be important in optoelectronic applications. These works mostly employ uniaxial or biaxial strain. However, due to intentional or unintentional reasons [44], [45], silicon nanowires can actually be under quite a large amount of bending strain. Naturally, it is desirable to investigate their electronic and optoelectronic properties. So we do classical molecular dynamics and quantum mechanical simulations to understand the strain profile and electronic transmissions in such nanowires in Chapter 5. Uniaxially strained silicon nanowires of similar sizes have also been simulated. Comparison shows that, for same average strain, bent nanowires have a larger decrease in their transmission gap, which represent a larger increase in conductivity.

1.4 OUTLINE OF THE THESIS

This thesis is organized as follows.

1) Before delving into nanowires, we discuss the theory, fabrication and experimental measurements of photocurrent characteristics of bulk silicon MSM photo sensor devices in Chapter 2. We describe that asymmetry in (i) physical sizes of two metal pads and (ii) light position with respect to contact electrodes can produce large photocurrent.
2) In Chapter 3, we describe simulation and modeling of asymmetric-work-function metal contacts based nanowire photo sensing devices. Short circuit current, open circuit voltage and photocurrent densities are studied in detail. Guideline for choosing appropriate metals is given. Long nanowires with contacts only at the ends are found to be less efficient in terms of current density. An improved design with distributed contacts to maximize their output is then proposed. Finally, it is shown that further performance enhancement can be achieved with gated diode design, which also produced a small negative differential resistance (NDR) effect.
3) In Chapter 4, fabrication and characterization of nanowire network based two contact photo sensors are presented. It is found that, although the fabrication approach is very simple, the devices produce appreciable amount of photo currents. Depending on the relative lengths of the nanowires with respect to the contact to contact distance, either dense or sparse network may produce more current. The case of some sparse networks producing relatively larger currents is explained by considering the detail of the current transport mechanism in the network.

4) Chapter 5 investigates electronic transport properties of strained narrow silicon nanowires using molecular mechanics and non-equilibrium Green's function (NEGF) simulations. Strain variations in the bent nanowires are analyzed in detail. Then, electronic transmission, and the energy gap therein, are correlated with the nanowire diameter as well as the amount of bending. Finally, the strain induced transmission gap change in bent nanowires is compared with the same effect in similar uniaxially strained nanowires, and it is shown that bent nanowires show a larger gap decrease for similar strain.
5) The last chapter, Chapter 6, summarizes the thesis and discusses future work directions

Chapter 2. PHOTORESPONSE OF SILICON WITH ASYMMETRIC AREA CONTACTS

We report metal-semiconductor-metal (MSM) photo sensors based on asymmetric metal pad areas. Our photosensor devices displayed strong absorption properties upon exposure to electromagnetic radiation. Our devices are simple to fabricate, requires a single-step metal deposition, and exhibit photoresponse even at zero bias conditions. In this chapter, we present a brief discussion on the theory behind the necessity of asymmetry in contact pads to enhance photoresponse in short circuit, which is generally achieved by variation in metal work function. In addition, we present the theoretical explanation and experimental verification with our proposed prototype devices made of platinum deposited on bulk silicon. Our results display a large photo current and a zero dark current under zero applied voltage at ambient environmental conditions. Our device offers excellent light switching behavior that are fast and stable at room temperature, which make them excellent candidates for innovative devices with extreme stability and reliability.

2.1 INTRODUCTION

Silicon based photosensing is an exciting area of research that finds numerous applications in high-tech device fabrication industry for integrated active/passive optical components such as filters, sensors, detectors [46], [47]. These devices are compatible with the low cost complementary metal oxide semiconductor (CMOS) fabrication process which makes possible having both optical and electronic circuits in a single microchip [41]. Silicon photo sensors are found in various device configurations such as photodiode [48], phototransistor [49], [50], simple Schottky diode [51], and MSM dual Schottky diodes [41], [50]–[56]. The MSM devices hold great potentials due to their simple fabrication process, low capacitance, ease of integration with preamplifier circuits, large bandwidth as well as high sensitivity [41], [53]. MSM photo sensors with a single as well as double metals have been demonstrated in both III-V [54] and IV [41], [52] semiconductors. They, however, have a relatively large dark current [55], which causes additional power dissipation in the already hot and densely packed integrated circuits. Most of the remedial efforts so far [41], [52], [54] are focused towards achieving an asymmetry in the contact metal work functions as well as replacing the high cost direct bandgap materials with the low cost silicon. Significant contribution by Okyay et al. [53] discusses the importance of asymmetric area electrodes that can be utilized to suppress the Schottky diode leakage current. A recent study by Zhang et al presents the simulation study on the influence of asymmetric electrode structures for effective dark current suppression in silicon based photodetectors [57]. However, a detailed experimental study of the photoresponse of such devices, specifically under zero bias conditions is still missing.

In this chapter, we present a thorough experimental analysis on MSM device with metal contacts of similar workfunction but dissimilar contact areas. The photosensor devices involves a very simple and cost-effective CMOS fabrication process which includes a one-step metal deposition on a standard silicon wafer. A large photoresponse is observed, even under low light and low or zero bias conditions. In addition, we also present the simulation studies on our device structure which validates the experimental results. This chapter presents a complete discussion on the theoretical background of the device model followed by the fabrication process, experimental studies and simulation results. Both dark and light currents measurements were performed with the prototype devices. Photoresponse of the detector device as a function of laser power and wavelength is presented here.

2.2 THEORY OF METAL-SEMICONDUCTOR-METAL PHOTO SENSORS

When semiconductor materials, such as silicon, are exposed to electromagnetic radiations, they absorb part of the light that results in the excitation of its valence band electrons to its conduction band. The absorption properties of semiconducting materials are dependent upon the electronic structure of the semiconductor as well as the thickness of the material. The excited electrons in conduction band participate in charge transport thereby increasing the electrical conductivity of the material resulting in an improved electrical signal.

In order to obtain a photo current signal from light shining on a piece of semiconductor, the photo generated carriers inside the material must be collected through the metal contacts. However, if the numbers of photo-generated electrons (holes) collected at the two contacts are equal, the net photo current due to electrons (holes) will be zero. This is the general observation in semiconductors if the two metal pads are identical and the light intensity is uniform all over the device. Such circumstances are normally overcome by employing either a p-n junction inside the semiconductor or using two dissimilar metals as two contacts. However, both of these approaches will take more than one photolithography step. Creating the p-n junction in semiconductor wafer requires at least one step for doping and another step for the metal deposition. Similarly, constructing dissimilar metal contacts on semiconductors involve two separate metal deposition steps.

Here, we propose a one-step lithography process for fabricating asymmetric electrical contacts based photo sensors. In case of a Schottky contact, the electron transport property of the device depends upon the contact area between the metal and the semiconductor since the amount of tunneling is directly proportional to the contact area. Amount of surface recombination will also depend on the contact size. Hence, if we make the two contacts of a photo sensor with the same metal but of dissimilar contact areas as displayed in Figure 2.1(a), the device will have the required asymmetry for photo current. Therefore, a single step photolithography process is sufficient to achieve the asymmetry which is ideal in creating a non-zero photocurrent. Since amount of surface recombination depends on the contact area, even dark current will have an asymmetry in it, as verified by both simulation and experimental results.

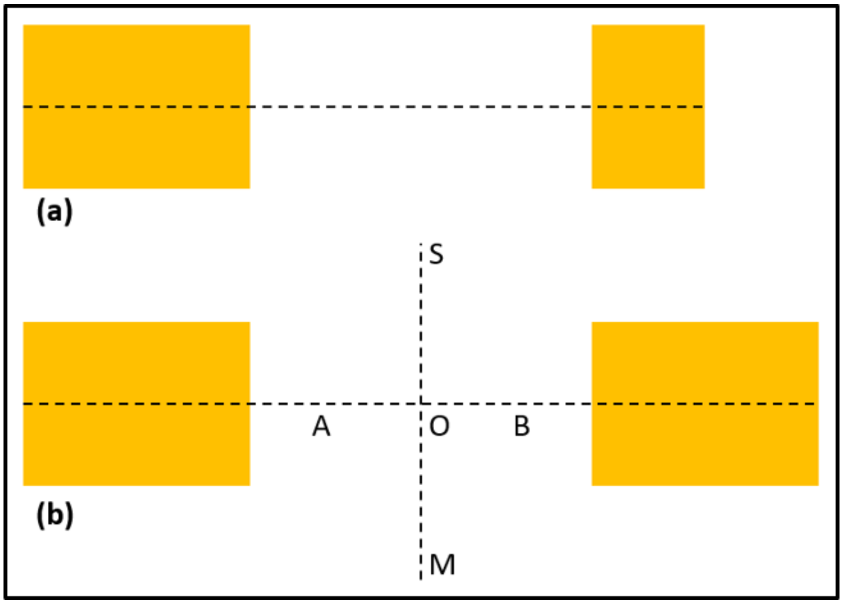

Figure 2.1. Asymmetric contact photo sensors; asymmetry due to (a) contact size, (b) light position.

Alternatively, the position of the light spot that is being detected by the semiconductor can itself introduce an asymmetry into an otherwise symmetric metal contact pair as illustrated in Figure 2.1(b). The semiconductor between two similar metal pads of equal size when exposed to the spotlight that is smaller than the gap size between the metal pads as indicated in the figure (i.e. at the midpoint O), the total system is still symmetric, and there will be no net photo current at zero bias. In fact, position of the spotlight at any point along the line, SOM, will lead to a symmetric device and hence a zero photocurrent at zero bias condition. However, if the position of the spotlight is deviated from the line SOM, for example at point A or B, an asymmetry is introduced in the circuit thereby generating a photo current at short circuit.

For both the photo sensors in Figure 2.1, the degree of asymmetry will depend on the light position with respect to the two contacts, and as a result, the magnitude of photo current will vary depending on the light position. Considering the device in Figure 2.1(b) and a light source with constant spot size, light location at point O will give zero photo current due the symmetry as already discussed. Now as light position moves towards the left contact, along line OA, the current magnitude will first increase, reach a maximum and then fall off as some of the incident light will be obstructed by the metal pad, assuming the pad reflects off most of the incident light. If this current is assumed positive, then a mirror symmetric (negative) current profile will be generated as the light position moves starting from point O towards the right contact, along line OB.

2.3 DEVICE FABRICATION

Fabrication was done on p-type, 100 mm diameter, and 500 um thick silicon wafer. The process flow is shown in Figure 2.2. First, the wafer was run through a spin, rinse, dry (SRD) cycle to clean it. Then, to remove any organic contaminants, barrel etching was done for 5 minutes at 100 W power. Next, standard photolithography was used to pattern resist on the wafer. Briefly, NR7-1000PY negative resist was spun coated and then baked at 150 C on a hot plate for 60 seconds. The resist was then exposed and again baked at 100 C for 50 seconds. TMAH based developer, RD6, was used to develop the resist. This was followed by an SRD cycle. Immediately before metal deposition, barrel etching was done to remove residual photoresist from the developed away regions. This etching was done for 30 seconds at 50 W power. Then electron beam assisted evaporation was done to deposit 10 nm chromium adhesion layer and then 20 nm platinum layer. Finally, metal liftoff was done in acetone.

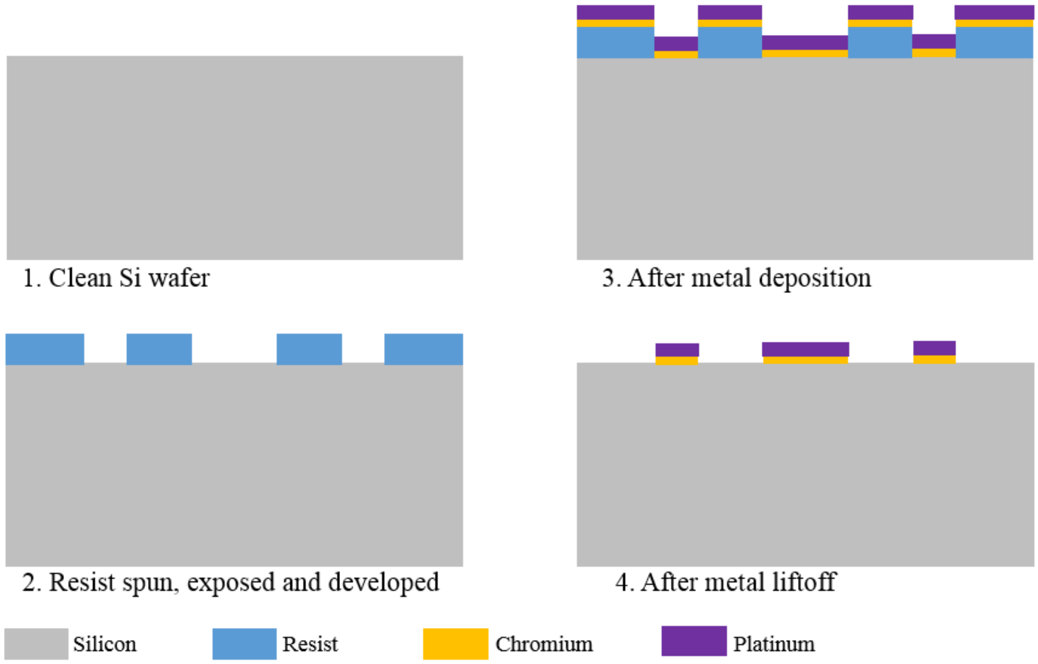

Figure 2.2. Device fabrication steps.

2.4 Experimental Results and Discussions

Figure 2.3 shows both dark and photo current as a function of device bias for five different devices with one large and one small pads. Two probe IV measurements performed to characterize each and every contact pad revealed the absence of the commonly existing Ohmic behavior in nanodevice transport properties. This is a clear evidence of the formation of rectifying junction in our devices. The graph clearly shows the asymmetry in dark current (Figure 2.3(a)) and displays zero current at zero bias conditions. Our devices exhibited a slow increase in current until a threshold voltage is achieved due to the presence of the rectifying junction beneath the pads. Upon exposure to electromagnetic radiations in the visible range, the same set of devices exhibited photovoltaic properties in all five cases as displayed in Figure 2.3(b). A huge elevation in photocurrent, up to four orders of magnitude of increase, was observed in all our devices. It is essential to mention that the position of the spotlight is fixed at the midpoint between the two pads.

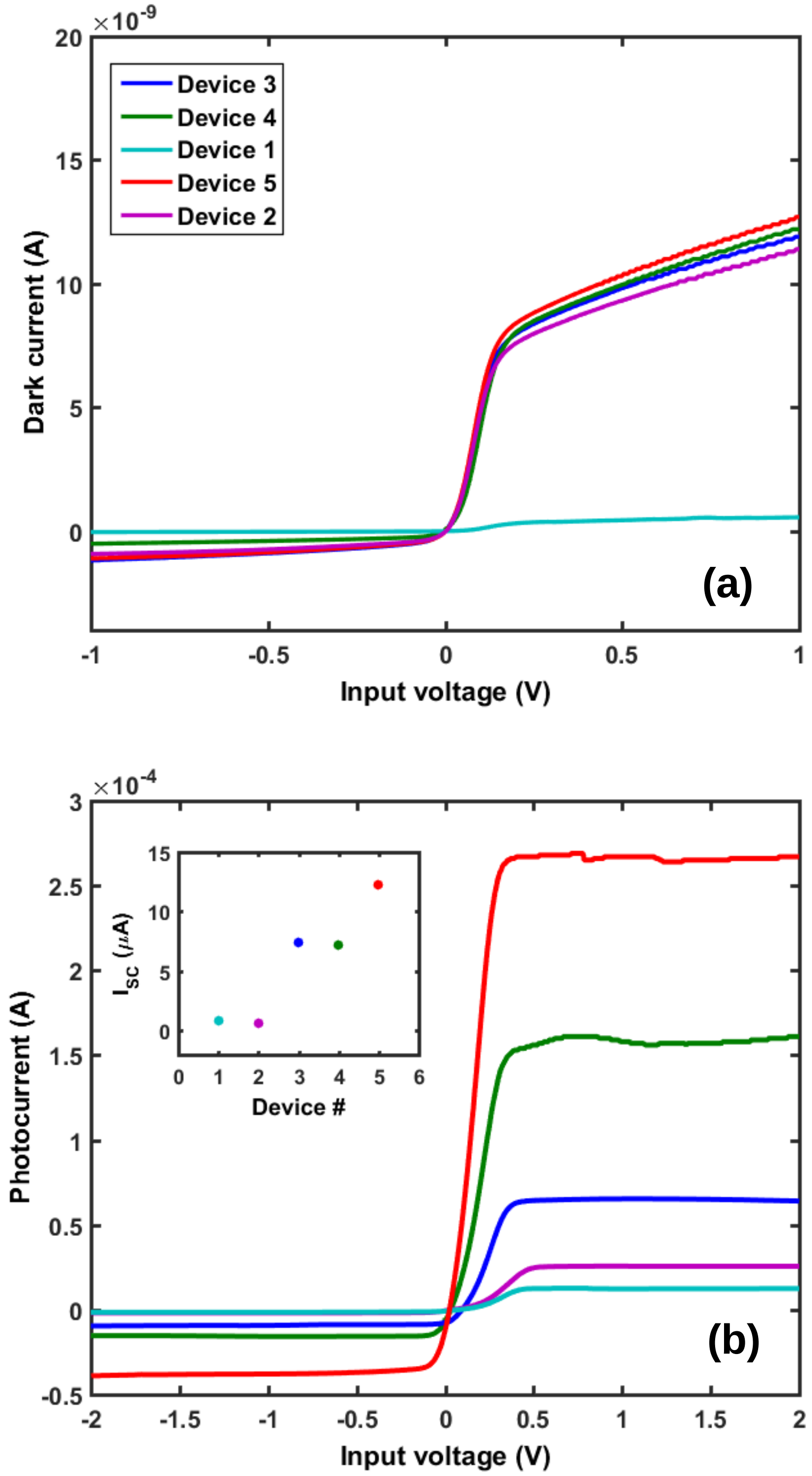

Figure 2.3. Dark (a), and photo (b) current with bias for different prototype asymmetric-area contact devices. Inset of (b) shows the zero bias photocurrent for the same devices.

In both photocurrent and dark current asymmetry is observed with bias polarity. Such asymmetry, we believe, is due to the asymmetry in contact pad areas. In addition, we observed a photocurrent at zero bias, as shown in the inset of Figure 2.3(b). Our experimental results clearly show that the contact area asymmetry is effective at producing large photocurrent and dark current at zero bias.

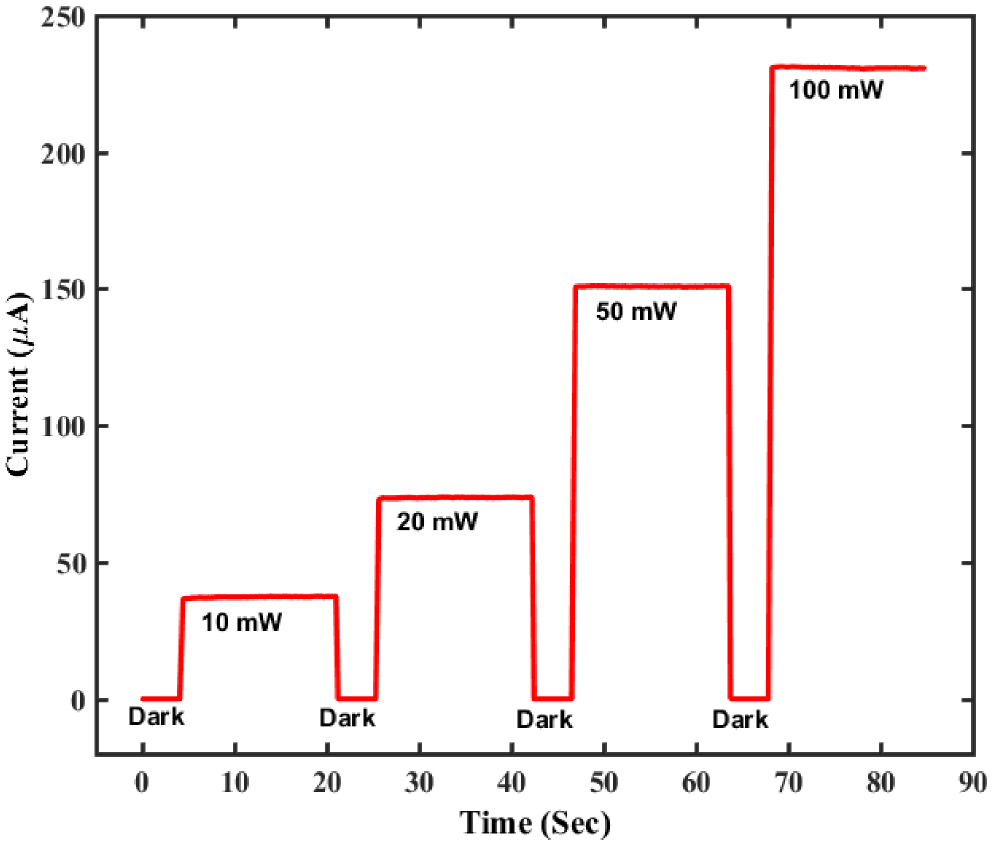

Figure 2.4. Current vs time graph display of the light switching with red laser of varying intensity at zero bias conditions.

In an attempt to further explore the robustness of our devices, we have also investigated the instant photoresponse which is primarily determined by the rate of photo-generation of the charge carries and we studied the light intensity dependence on the transport properties in asymmetric contact pads. This study was carried out by shining a red laser of wavelength 650 nm between the asymmetric contact pads at regular time intervals. The results displayed in Figure 2.4 confirms the switching behavior of our devices when the light source is turned ON/OFF and its dependence to variation in intensity, exhibiting larger photocurrent for high power lasers. The dark current is zero due to the zero applied bias while the observed photocurrent is in tens or hundreds of micro Amperes. The improved response in the optoelectronic transport properties of our devices can be explained by the asymmetry in area of contact pads which cause asymmetry in carrier collection. Area asymmetry is also a factor in I-V characteristics of a Schottky junction [58]. This stimulates photocurrent. For the results in Figure 2.4, the applied bias between the two metal pads is kept at zero volt. The laser intensity is varied from 10 mW to 100 mW. However, during each laser ON period, the intensity is kept constant.

The laser spot position was fixed to a location between the asymmetric metal pads, which produced maximum photocurrent. As the light source was turned ON and OFF, a rapid switching behavior is observed. The dark current is zero due to the zero applied bias while the photocurrent, due to contact area asymmetry, is tens or hundreds of micro Amperes. Based on the behavior of our devices to high power laser exposure, we believe that a significant photocurrent can be observed with low power lasers and low intensity light sources.

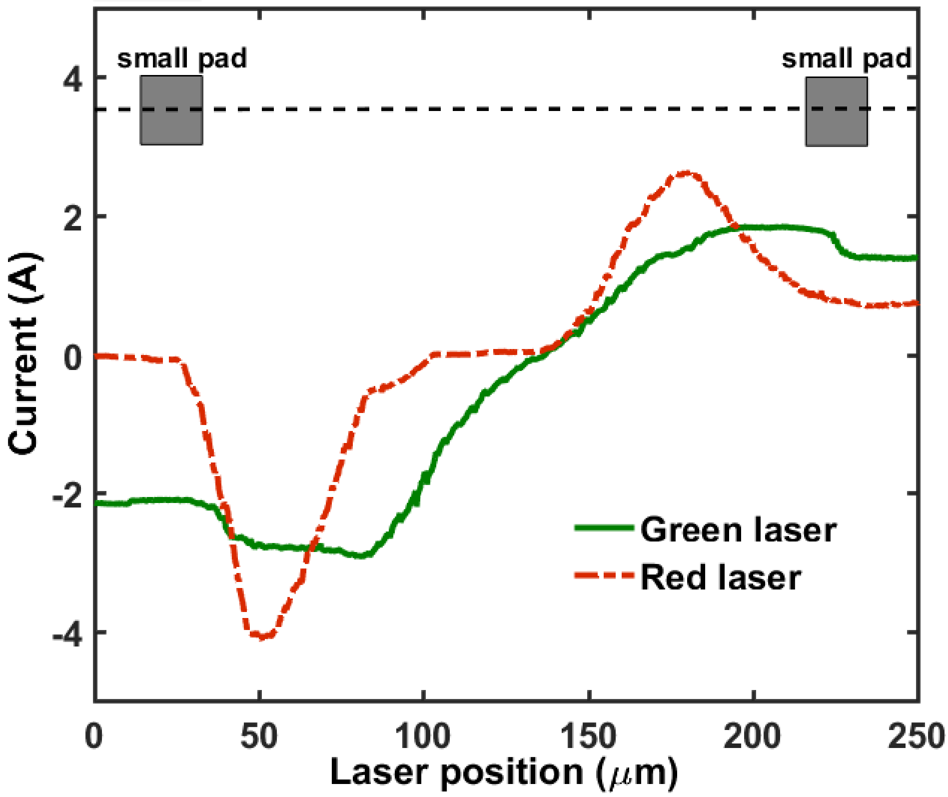

Figure 2.5. Photocurrent as a function of position. Solid line for green laser and dashed line for red laser.

We also explored the possibilities of introducing asymmetry in transport properties of our devices with symmetric contact pads. In such devices, the spot size and position of the light source played a major role in determining the changes in the magnitude of photocurrent. We were able to observe the variation in transport properties as the laser spot is swept from one metal pad to the other. Figure 2.5 present the photocurrent vs time graph of the devices upon exposure to green and red lasers. The position of the laser spot is moved from the left end toward the right at an approximately constant velocity. This is achieved by mounting the laser source on a micrometer moving and rotating the later at a constant speed. As the figure displays, a gradual decrease in photocurrent was observed as the laser spot moves from left to right. This continued until the photocurrent attained a negative maximum. With any further change in the position of the laser spot towards the right contact pad, the photocurrent increased to zero approximately around the midpoint between the contact pads. Moving on further we observed a similar change in photocurrent, this time attaining a positive maximum closer to the right contact pad. Based on our studies on symmetric contact pad devices, we conclude that fixing the position of the light source at any on the peak positions will yield a significant increase in photocurrent at zero bias conditions, given that the spot size of the laser is much smaller than the gap between the metal pads. All these studies are carried out at ambient temperature and pressure conditions using red and green laser source of approximately 10mW power.

A greater photoresponse with a well-defined peak is observed with red laser which also exhibited a better symmetry with respect to the midpoint of the contact pads. The larger current can be attributed to the band gap of the semiconductor silicon and the workfunction of the metal pads. Also responsivity of silicon increases with wavelength until it reaches a maximum at about 950 nm and then falls of as we approach and go beyond the bandgap.

2.5 DEVICE SIMULATION AND MODELING

Experimental results from our prototype devices verify the theory we presented. Next to gain a better understanding of the device physics and phenomena responsible for asymmetry and large short circuit current under light, we model an asymmetric-area-contact device using state-of-the-art TCAD simulations [59]. For simplicity, we consider a two dimensional (2D) device. Such a device maintains the underlying physics that we are interested in, i.e., contact size asymmetry, but reduces the computation cost to a manageable level. It can be assumed that the 2D structure is taken from a vertical cross-section along the horizontal dashed line in Figure 2.1(a). Figure 2.6 depicts the device that we simulate.

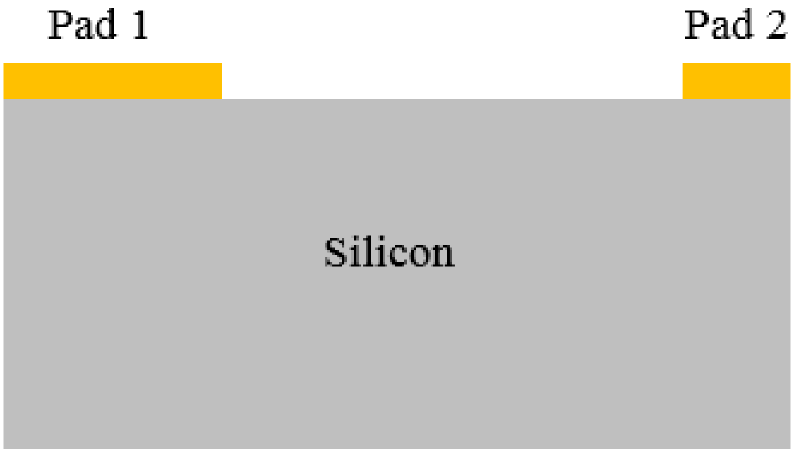

Figure 2.6. Structure of the simulated 2D device where Pad 1 is larger than Pad 2. Silicon size is 25 μm (horizontal) by 10 μm (vertical). Pad 1 length is fixed at 2 μm while Pad 2 length is varied.

The silicon size is 25 μm by 10 μm. Doping density is n-type 10^{15} cm^{-3} and minority carrier lifetime of 1 μSec is assumed. Pad 1 length (Figure 2.6) is kept fixed at 2 μm while the length of Pad 2 is varied to achieve a device with varying amount of asymmetry. The recombination processes that we consider are Shockley-Read-Hall (SRH) and Auger recombination. In addition, surface recombination as well as barrier lowering effects have been taken into account as they are important for a Schottky junction and found to give better match with trends in experimental results.

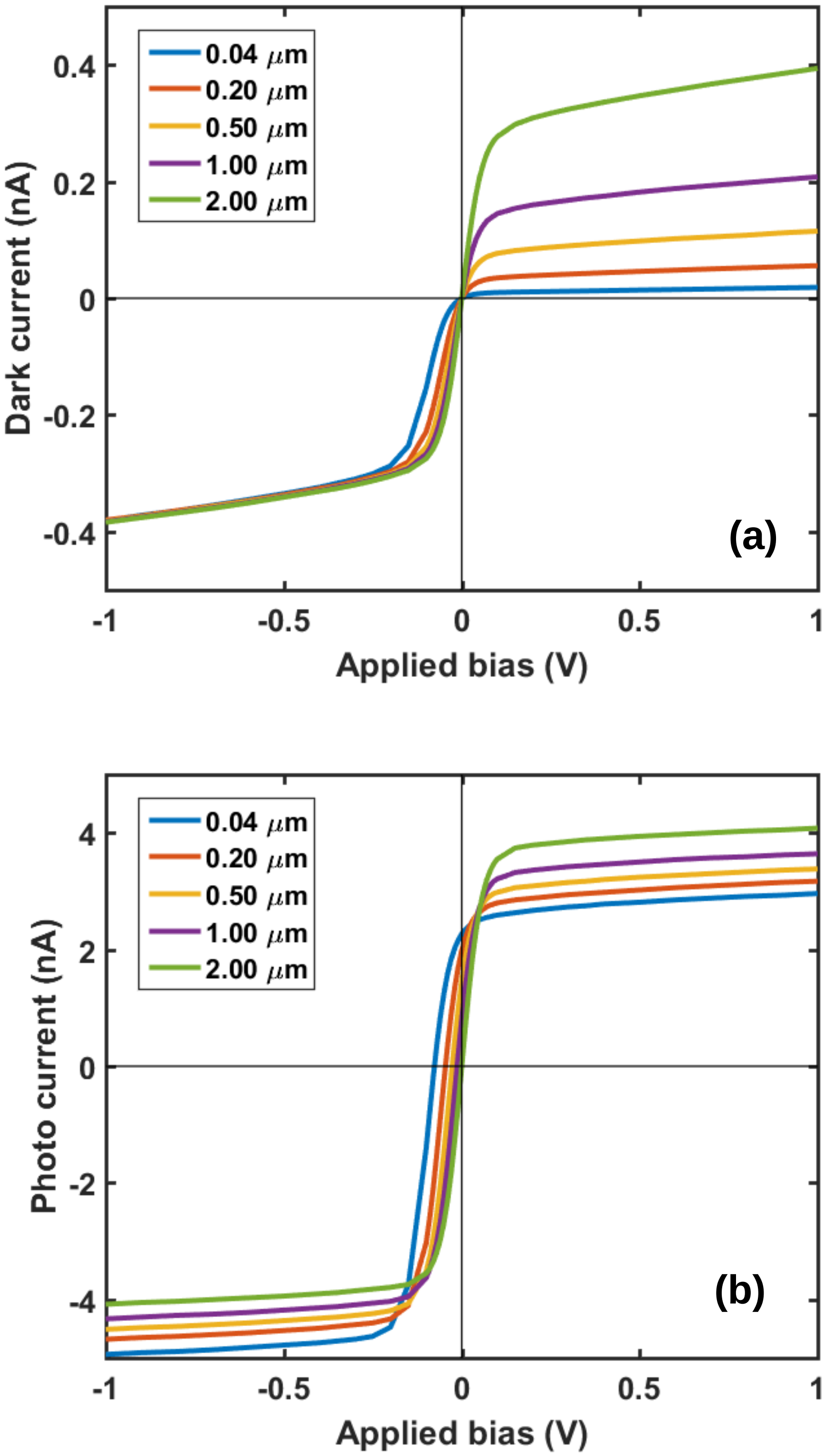

Figure 2.7. Current vs voltage profile of two contact device. One contact size is fixed while the size of the other varies. (a) dark, (b) with light.

Figure 2.7 presents the current versus voltage profile of the device in Figure 2.6 for bias range of -1 V to +1 V in both dark (a) and light (b). The length of Pad 2 is varied from 40 nm to 2 μm. The asymmetry is obvious; the larger the contact size asymmetry, the larger the asymmetry in current. At zero applied bias, the dark current is zero irrespective of the contact asymmetry, which is necessary. However, the zero bias photocurrent is zero only for the symmetric case, that is, when both contacts are 2 μm long. For asymmetric contacts, large photocurrent, which follows the contact length asymmetry, is achieved. The current versus voltage profile has some interesting features: at lower voltage current increases sharply. But at higher voltage, it saturates. The saturation region has a slope due to barrier lowering in Schottky contact. As the length of the Pad 2 increases, its saturation current also increases, as there are larger and larger contact area for surface recombination as well as current conduction. The simulation characteristics (Figure 2.7) match quite well with the experimental results (Figure 2.3).

Some comments on the shape of saturation current versus bias follow. Simulation suggest that surface recombination alone can account for overall current asymmetry but once saturation is reached, the current remains flat if only surface recombination effect is taken into account. However, Schottky barrier lowering with bias is an important effect for metal-semiconductor junctions and we found that once barrier lowering is considered we recover the slowly increasing linear I-V in the saturation current as we saw in the experimental I-V.

Next we consider device of the type shown in Figure 2.1(b). As already mentioned, physically the device is symmetric, but the light spot position can cause an asymmetry if it is smaller than the anode to cathode gap. Figure 2.8 plots the zero bias photocurrent for three different laser lights as the position of the light is varied from the leftmost edge to the rightmost of the device shown in the inset of Figure 2.8. The flat regions are due to the metal contact which does not absorb any light.

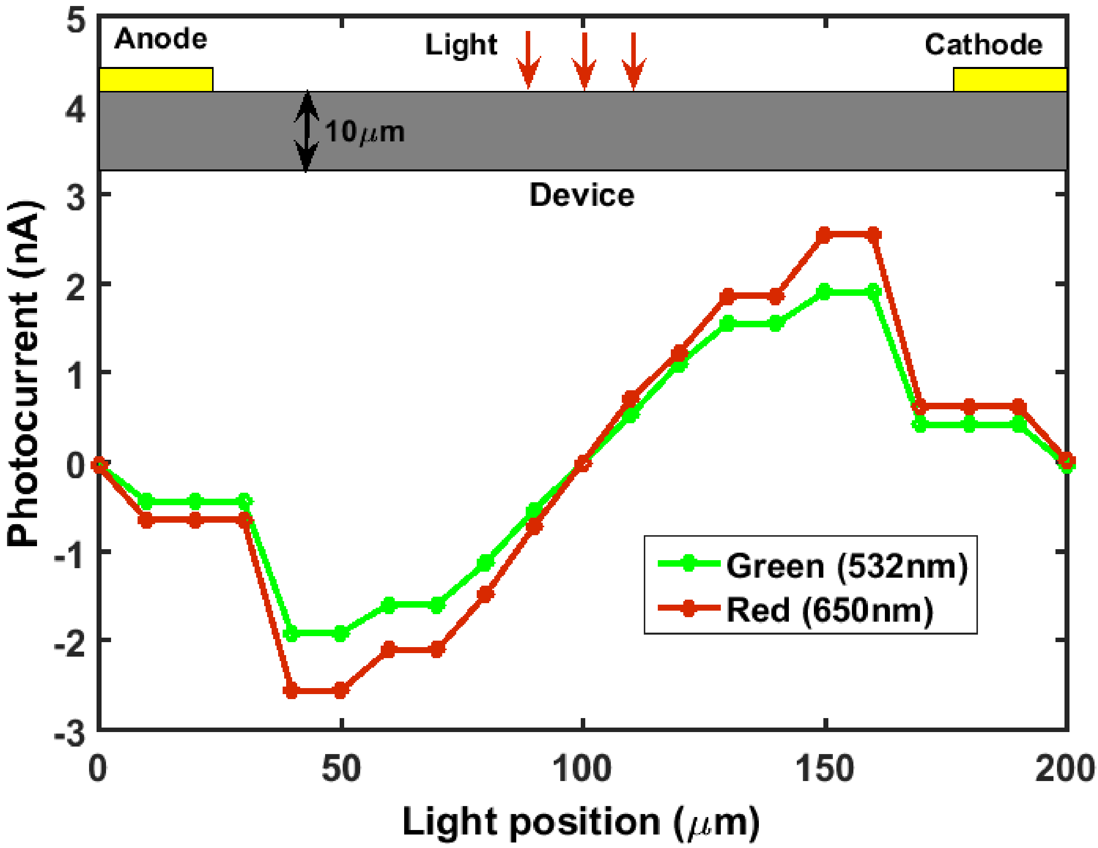

Figure 2.8. Current vs light position profile of symmetric device. Light position is varied.

Two different discrete wavelength lasers - green (532nm) and red (650nm) - have been used and the photocurrent is found to increase with wavelength for the two values used. As expected, the photocurrent is zero when the laser is at the midpoint between the two pads but its magnitude increases as the laser moves towards either of the pads because the amount of asymmetry increases. Since the contact pads are symmetric the current is mirror symmetric. Note that the current magnitude is largest when light is shone close to a contact, but not exactly at the edge. The reason is when light is at the pad edge, half of the width of the light beam will be reflected by the metal pad.

2.6 CONCLUSION

In summary, we have successfully demonstrated the experimental verification of employing asymmetric-size contact pads in MSM devices to produce large photocurrent based on our studies in both dark and light conditions as zero bias. We did device simulation to first demonstrate validity of the theory as well as to get an idea about the device response. We then fabricated and characterized prototype devices. Our devices are simple, easy to fabricate, involves a single step metal deposition process and are cost effective. We tested the performance of our devices under different bias conditions and verified that the enhancement in photocurrent in all devices studied is mainly due to the asymmetry in contact pad area. Our devices also exhibited excellent light switching behavior which are fast, stable and reliable. Extreme sensitivity and selectivity to light intensity make them suitable candidates for innovative photosensor devices. We also performed similar measurements on symmetric contact area devices to validate the observed photocurrent enhancement in asymmetric contact pads. In symmetric devices, we observed the significance of spot size and position of the light source in creating asymmetry in photocurrent at zero bias conditions. Our newly proposed simple design high performance device will greatly influence the industry of MSM photosensors.

Chapter 3. MODELING OF DUAL-METAL CONTACT BASED SILICON MICRO AND NANO WIRE SOLAR CELLS

We study solar cell properties of single silicon wires connected at their ends to two dissimilar metals of different work functions. Effects of wire dimensions, the work functions of the metals, and minority carrier lifetimes on short circuit current as well as open circuit voltage are studied. The most efficient photovoltaic behavior is found to occur when one metal makes a Schottky contact with the wire, and the other makes an Ohmic contact. As wire length increases, both short circuit current and open circuit voltage increase before they start to saturate. Depending on the contact work function difference and the wire dimensions, the saturation length increases by approximately an order of magnitude for a two order of magnitude increase in minority carrier lifetime. However current per surface area exposed to light is found to decrease rapidly with increase in length. The proposed use of a multi-contact interdigitated design for long wires is found to increase the photovoltaic response of the devices. It is also shown that use of a grounded gate can improve both short circuit current and open circuit voltage.

3.1 INTRODUCTION

One dimensional nanomaterials like nanowires and nanotubes hold great potential for many applications such as electronics [60], [61], sensors [62], [63], and photovoltaics [3], [11], [64]. Nano engineered materials like nanowires and nanotubes are considered important candidates for low cost and high efficiency solar cells. There have been many studies on solar cells based on single as well as multiple nanowires [1], [2], [65], [66]. Tsakalakos *et al.* [1] studied p-n junction based silicon nanowire solar cells on metal foils, and found large current density and low optical reflectance. Sivakov *et al.* [2] fabricated silicon nanowire solar cells by electroless wet chemical etching of micro crystalline silicon layer on glass and achieved a high power conversion efficiency of 4.4%. Tian et al. [65] studied single p-i-n coaxial silicon nanowires and measured open circuit voltage (V_{oc}) of 0.26 V and short circuit current (I_{sc}) of 0.503 nA. Experimental study on Schottky solar cells comprising multiple SiNWs bridging two different metals with different work functions was carried out by Kim et al. [66]. They obtained a low V_{oc} of 0.167 V but high I_{sc} of 91.1 nA. Kelzenberg et al. [67] studied single-nanowire solar cells with one rectifying junction created by electrical heating of the segment of the nanowire beneath it. For a nanowire of diameter 900 nm, they achieved a V_{oc} of 0.19 V and a short circuit current density of $5.0\ \mathrm{mA\,cm^{-2}}$. Hybrid Schottky diode solar cells [68] with poly(3,4-ethylenedioxythiophene) poly(styrenesulfonate) (PEDOT:PSS) film deposited on metal-assisted chemically etched SiNW arrays produced Voc of ~0.48 V and J_{sc} of ~30 mA/cm^2. These works on nanowire based solar cells primarily focus on experimental investigations to demonstrate their potential in realizing the next generation of solar cells. However, a detailed study on the influence of various parameters like nanowire dimensions and work function of the metal contacts in modifying the photovoltaic behavior of the nanowires is lacking. In this chapter, we present results of our simulation studies of Schottky junction based microwire and nanowire solar cells, and investigate the dependence of their photovoltaic properties on metal work functions, wire dimensions as well as minority carrier lifetimes.

3.2 DEVICE STRUCTURE, PROBLEM STATEMENT, AND SIMULATION METHOD

Figure 3.1 is a sketch of the device under study. There are two dissimilar metal pads, with dissimilar work functions, bridged by a rectangular cross-section wire. L, W and H represent the wire length, width and height, respectively. The array of the downward pointing arrows represents incident light beam. Only the top surface (of area L x W) of the wire is illuminated. The effect of the substrate is not considered in this work. Performance enhancing features such as an antireflection coating or back reflector have also not been included so as to keep the focus on the role of the silicon wire and metal contacts.

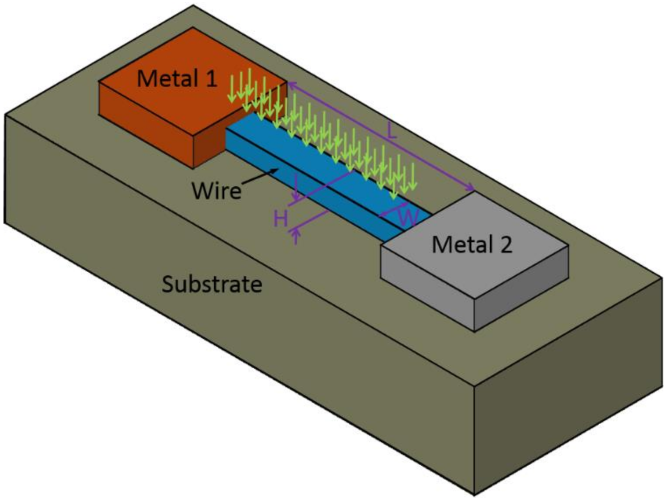

Figure 3.1. Schematic representation of a single nanowire between two metal pads. Wire dimensions are indicated, and the downward pointing array of green arrows represents the incident light.

We focus on understanding how device dimensions and minority carrier lifetimes affect the photovoltaic properties (short circuit current, open circuit voltage, I-V characteristics) of the solar cell. This chapter also investigates the effects of the metal work functions on the solar cell performance. It explores ways to improving the efficiency of the solar cells, including selection of metals, use of multiple contacts, and a grounded gate electrode.

Modeling studies of the structure are carried out Silvaco Atlas software [59]. In this simulator the device structure (Figure 3.1) is meshed, and device equations (see below) are discretized and solved on device mesh points with appropriate boundary conditions. For device meshing, a wire (device) with given L, W, and H is taken. The wire is covered by a 1 nm thick silicon dioxide on all surfaces. Usually a constant doping of given type and amount is assumed at all the grid points. However, for simulations involving the p-i-n type structure, there are three different regions, each with a different but still uniform doping density. The nanowire is contacted with two or more electrodes. A metal of a specific work function forms an electrode. Wherever there is an electrode, the oxide at the surface of the wire is removed so that the metal is in direct contact with the silicon. The device (nanowire + oxide + electrodes) is meshed (discretized) using prism elements along all three directions for a three dimensional (3D) simulation. For a two dimensional (2D) simulation, a vertical cross section of the metal-wire-metal structure is discretized using triangular elements. Silvaco Atlas solves the following equations on the device mesh:

Poisson's equation

$$\nabla \cdot \left(\varepsilon_r \varepsilon_0 \nabla \psi \right) = -\rho \tag{3.1}$$

Carrier continuity equation

$$\frac{1}{q} \nabla \cdot \vec{J}_n + G_n - R_n = 0 \tag{3.2a}$$

$$-\frac{1}{q} \nabla \cdot \vec{J}_p + G_p - R_p = 0 \tag{3.2b}$$

Drift-diffusion transport equation

$$\vec{J}_n = -q \mu_n n \nabla \phi_n \tag{3.3a}$$

$$\vec{J}_p = -q \mu_p p \nabla \phi_p \tag{3.3b}$$

Quasi-Fermi levels

$$\phi_n = \psi - \frac{k_B T}{q} \ln\left(\frac{n}{n_i} \right) \tag{3.4a}$$

$$\phi_p = \psi + \frac{k_B T}{q} \ln\left(\frac{p}{n_i}\right) \qquad (3.4b)$$

Carrier recombination

$$R_{SRH} = \frac{pn - n_i^2}{\tau_p\left(n + n_i\right) + \tau_n\left(p + n_i\right)} \qquad (3.5a)$$

$$R_{AUG} = \Gamma_n\left(pn - nn_i^2\right) + \Gamma_p\left(np^2 - pn_i^2\right) \qquad (3.5b)$$

Light absorption and photo generation

$$G_n = G_p = G_L = \eta_0 \frac{P\lambda}{hc}\left(\frac{4\pi}{\lambda}k\right)\exp\left(-\left(\frac{4\pi}{\lambda}k\right)y\right) \qquad (3.6)$$

Table 3.1. List of variables

Symbol	Name	Symbol	Name
ψ	Electric potential	n_S	Surface electron density from charge neutrality
ρ	Charge density		
n	Electron density	p_S	Surface hole density from charge neutrality
p	Hole density	μ_n	Electron mobility
$\vec{J}_n$	Electron current density	μ_p	Hole mobility
$\vec{J}_p$	Hole current density	ϕ_n	Electron quasi-Fermi level
G_n	Electron generation rate	ϕ_p	Hole quasi-Fermi level
G_p	Hole generation rate	τ_n	Minority electron lifetime
G_L	Photo generation rate	τ_p	Minority hole lifetime
R_n	Electron recombination rate	P	Ray intensity factor, includes effects of reflections, transmission and absorption
R_p	Hole recombination rate	k	Imaginary part of index of refraction
$V_{applied}$	Applied bias	λ	Wavelength of light
W_f	Metal work function	ε_r	Relative permittivity

Table 3.2. List of constants

Constant	Name	Value
ε_0	Permittivity in vacuum	$8.854\times10^{-14}\mathrm{F}\cdot\mathrm{cm}^{-2}$
q	Magnitude of electron charge	$1.6022\times10^{-19}\mathrm{C}$

n_i	Intrinsic carrier density	$1.45\times10^{10}\text{cm}^{-3}$
μ_n	Electron mobility	$1000\ \text{cm}^2\text{V}^{-1}\text{s}^{-1}$
μ_p	Hole mobility	$500\ \text{cm}^2\text{V}^{-1}\text{s}^{-1}$
k_B	Boltzmann's constant	$1.38\times10^{-23}\ \text{JK}^{-1}$
T	Temperature	300 K
Γ_n	Electron Auger recombination parameter	$2.8\times10^{-31}\ \text{cm}^6\text{s}^{-1}$
Γ_p	Hole Auger recombination parameter	$9.9\times10^{-32}\ \text{cm}^6\text{s}^{-1}$
h	Planck's constant	$6.626\times10^{-34}\text{m}^2\cdot\text{kg}\cdot\text{s}^{-1}$
c	Speed of light in vacuum	$3\times10^{10}\text{cm}\cdot\text{s}^{-1}$
E_g	Silicon bandgap energy	1.08 eV
χ	Electron affinity	4.17 eV
N_C	Electron effective density of states	$2.8\times10^{19}\ \text{cm}^{-3}$
N_V	Hole effective density of states	$1.04\times10^{19}\ \text{cm}^{-3}$

The symbols for variables and constants are defined in Table 3.1 and 3.2, respectively. Relative permittivity for silicon is 11.8.

There are two types of surfaces in the device: with contact and without contact. A contacted surface can be either Ohmic or Schottky. Ohmic contacts are implemented as simple Dirichlet boundary conditions with

$$\psi_S = \phi_n + \frac{k_B T}{q}\ln\frac{n_S}{n_i} = \phi_p - \frac{k_B T}{q}\ln\frac{p_S}{n_i} \tag{3.7}$$

while each Schottky contact is specified with an associated work function so that

$$\psi_S = \chi + \frac{E_g}{2q} + \frac{k_B T}{2q}\ln\frac{N_C}{N_V} - W_f + V_{applied} \tag{3.8}$$

In the non-contacted surfaces, homogeneous (reflecting) Neumann boundary conditions are imposed and the normal electric field components are assumed zero in such surfaces.

For a specific light condition, ray-tracing method is used to find the photo generation rate using (3.6). Next Poisson's equation and the current continuity equations (along with drift-diffusion equations) are solved self-consistently. At the beginning, an initial guess is found by the solution at equilibrium. In this case current continuity equations need not be solved, and only Eqs. (3.1) and (3.4) are solved to find potential and carrier densities inside the device. Once an initial guess has been obtained, the applied bias at the anode contact is increased in small increments (0.01V or 0.1V). The cathode bias is fixed at zero Volts. For each anode bias condition, the density values at the previous bias are used as an initial guess, and Poisson's equation is solved to calculate the device potential. The calculated potential is used in Eq. (3.4) to find the quasi-Fermi levels, which along the previous densities are substituted in Eq. (3.3) to find the current densities in terms of carrier densities. Finally, the current continuity equations are solved to find the updated carrier densities. The updated densities are substituted in Eq. (3.1) to find the updated potential. If the updated and previous potentials match within a tolerance, the simulation for current bias has converged and the applied bias is increased to the next value. If the tolerance has not been achieved, the process (calculation of densities and potential) is repeated.

3.3 SIMULATION VERSUS ANALYTICAL SOLUTIONS

We start with a case for which the simulation can be verified against a one dimensional (1D) analytical solution. For this, we assume that the contacts are Ohmic. For the simulation part, a microwire with $\mathrm{L} = 6.8\ \mu\mathrm{m}, \mathrm{W} = 1.0\ \mu\mathrm{m}, \mathrm{H} = 0.85\ \mu\mathrm{m}$ is 2D simulated. For the analytical solution, we consider the one dimensional (1D) minority carrier diffusion equation along wire length in the presence of an electric field [69]:

$$D_n \frac{\partial^2 \Delta n}{\partial x^2} + \mu_n \frac{\partial}{\partial x}\left(E\left[n_0 + \Delta n\right]\right) - \frac{\Delta n}{\tau_n} + G_L = 0 \qquad (3.9)$$

where D_n is carrier diffusion coefficient, μ_n is carrier mobility, E is the electric field, n_0 is equilibrium carrier density, Δn is photo-generated (excess) electron density, τ_n is electron lifetime, and G_L is photo-generation rate. Note that E is constant along length for Ohmic contacts.

Then excess minority carrier concentration, Δn, is found by solving Eq. (3.9), which is a linear second order differential equation having a solution of the form

$$\Delta n = Ae^{m_1 x} + Be^{m_2 x} + C \tag{3.10}$$

where

$m_{1,2} = -\frac{\mu_n E}{2D_n} \pm \sqrt{\left(\frac{\mu_n E}{2D_n}\right)^2 + \frac{1}{D_n \tau_n}}$. The constants A, B and C are found from the boundary conditions, $\Delta n(x=0)=0$ at the left contact and $\Delta n(x=L)=0$ at the right contact, and are given by

$$A = C\left(\frac{1-e^{m_2 L_x}}{e^{m_2 L_x} - e^{m_1 L_x}}\right), C = G_L \tau_n \text{ and } B = -A - C. \tag{3.11}$$

Here G_L along the 1D line for analytical calculation is extracted from two dimensional (2D) G_L generated by the Atlas simulator. Eq. (3.10) along with Eq. (3.11) represents the analytical expression of the excess minority carrier density. Analytical expression for current can be calculated by first finding the current densities as given below

$$\begin{aligned} J_n &= q\mu_n nE + qD_n \nabla n \\ J_p &= q\mu_p pE - qD_p \nabla n \quad [\text{as } \nabla p = \nabla n] \end{aligned} \tag{3.12}$$

where E is the electric field, $D_{n(p)} = kT\mu_{n(p)}/q$ is electron (hole) diffusion constant. Then total current, I, is found by multiplying the total current density by the cross sectional area, A, of the wire, or $I = A(J_n + J_p)$.

Figure 3.2 presents the comparison between the results from simulation (line with symbols) and analytical calculation (solid line) for our microwire with a uniform p-type doping density of $10^{15}\ \text{cm}^{-3}$. Figure 3.2(a) compares excess electron (minority carrier) density for different applied biases between the contacts. The photo generated minority electron density is symmetric with respect to the contacts for zero bias, but the peak density shifts towards the positive (right) contact $(\text{at position} = 6.8\ \mu\text{m})$ as the bias is increased. Figure 3.2(b) plots the total current with one sun illumination as a function of the bias voltage in the range 0.0-0.5 V. The plots display an excellent match between analytical calculations (solid line) and simulation results (symbol).

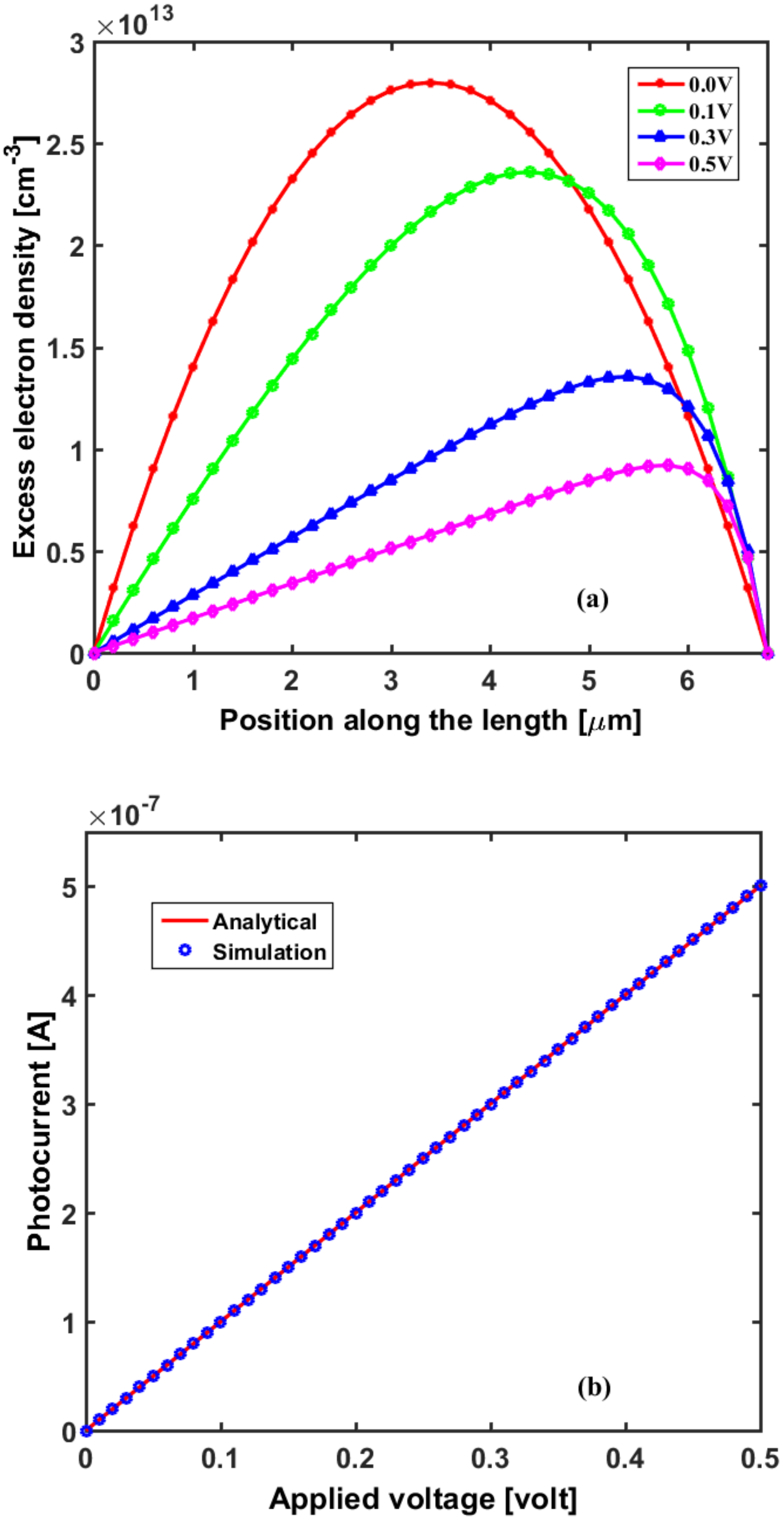

Figure 3.2. Comparison of (a) excess electron density and (b) photocurrent from analytical calculation (solid line) and simulation (symbol).

The device operation can be understood as follows. At dark and equilibrium, hole density (p) throughout the device is equal to the doping density ($10^{15}\ \mathrm{cm}^{-3}$) while electron density is n_i^2/p or $2\times10^{5}\ \mathrm{cm}^{-3}$. The current is obviously zero as there is no drift (due to zero electric field) or diffusion (due to zero density gradient). When a bias is applied at dark, due to Ohmic contacts, a constant electric field is set up along the length of the device. Hence the carrier densities are still the same as in the equilibrium case so that the diffusion currents are zero. However, drift currents proportional to the electric field (and carrier densities) are produced under bias. Since electron density is negligible compared to the hole density, the total current equals the hole drift current. Under an illumination, the microwire and nanowire photovoltaic devices absorb photons of energy higher than the bandgap that excite electrons from the valence band to the conduction band. This process generates excess electron-hole pairs. Note however that the excess carrier density is zero at the contacts due to requirement of boundary condition. Since at short circuit (or zero applied bias) the device is symmetric with respect to the contacts, the excess carrier density is symmetric dome shaped in this case, as shown in the red curve of Figure 3.2(a). This also implies a zero photo current at zero bias (zero drift) as excess carrier diffusions are equal and opposite. The excess carrier density is low for one sun illumination, so overall hole density is still dominated by the doping density. For electrons though the excess density is orders of magnitude higher than the equilibrium density, so Figure 3.2(a) essentially plots the electron density under illumination. As the bias is increased, the applied electric field shifts the maximum excess carrier position towards the positive contact. In this case both drift and diffusion photo currents, and a nonzero total photo current, are produced. We find that the dark current for this device is too high because of the Ohmic contacts so that photocurrent to dark current ratio is close to unity.

Thus for Ohmic contacts, an asymmetric carrier profile due the applied bias causes nonzero (drift and diffusion) current as shown in Figure 3.2(b). In addition to applied bias, asymmetry can also be introduced by dissimilar doping of the wire ends as well as by unequal work function metal contacts as discussed in section 3.5. For nanodevices, it is difficult to control the doping [24]–[27], while use of unequal-work-function metal contacts is relatively easier. Such an approach is also common in organic photovoltaics. Hence, in this chapter, we study the effect of asymmetry between the nanowire ends due to dissimilar-work-function metals on the photocurrent.

3.4 PHOTOCURRENT VS. WIRE LENGTH

In all results below, standard solar spectrum air mass 1.5 (AM1.5) has been used whenever light is present. The recombination processes that we consider are Shockley-Read-Hall (SRH) and Auger recombination. Varying values of minority carrier lifetimes used in this work are assumed to include a range of bulk and surface recombination values.

Minority carrier lifetime is an important parameter for solar cell devices. Intuitively, the longer the wire, the more the surface area to absorb light and the larger will be the number of excess carriers generated inside for a single device and hence the larger the current. However, only carriers that reach the contact contribute to any photocurrent. The rest of the electron-hole pairs recombine inside the device. A longer lifetime gives minority carriers more time to travel to the contact before recombination with a majority carrier. On the other hand, if the lifetime is too short, excess minority carriers recombine with majority carriers before reaching the contact and as such will not contribute to the photocurrent. Thus carrier lifetime sets a limit to the maximum wire length beyond which photo generated carriers are not collected efficiently and as a result the photocurrent saturates. Hence the wire lengths and minority carrier lifetimes are related. This is seen in the results shown in Figure 3.3, which plots zero bias photocurrent (short circuit current) of the wires of varying lengths for minority carrier lifetimes of 10μsec (solid curve), 1μsec (dashed curve) and 0.1μsec (dash-dotted curve). We consider doping density of $\sim 10^{15}$ cm^{-3} (p-type) for which minority carrier lifetime in crystalline bulk silicon is larger than 10μsec [70], [71]. However, due to large surface to volume ratio, nanowires can have high a surface recombination rate that can potentially reduce minority carrier lifetime [72], [73]. Life time that is an order of magnitude shorter than that of bulk silicon has been reported [73]. There have also been studies to improve the surface recombination and increase the lifetime [74], [75]. In view of these results, the lifetime values that we have selected are representative. Metal work functions of 5.5 eV (left contact) and 4.0 eV (right contact) have been used in this simulation.

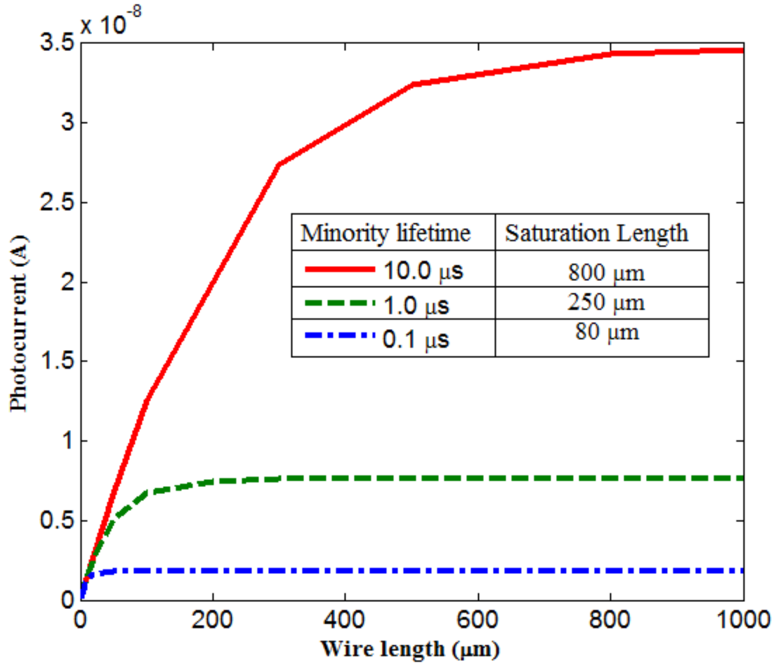

Figure 3.3. Photocurrent vs wire length for three different minority carrier lifetimes.

Figure 3.3 inset tabulates the relationship between the minority carrier lifetime and the device length at which the photocurrent approximately saturates. The saturation length is approximately proportional to the square root of the lifetime. This is reasonable given that the minority carrier diffusion length is defined as $L=\sqrt{D\tau}$, where $D=(kT/q)\mu$ is the diffusion constant, μ is the carrier mobility, and τ is the lifetime. At 300K, $L \approx 50\,\mu\text{m}$ for $\mu = 1000\ \text{cm}^2/\text{V-sec}$ and $\tau = 1\ \mu\text{sec}$. For this case saturation length is about $250\,\mu\text{m}$. This relation holds for other lifetimes as well. Hence the saturation length is about five times the minority carrier diffusion length. This may be a good design parameter for nanowire based solar cell.

3.5 EFFECT OF METAL WORK FUNCTION

As stated earlier, the results in Figure 3.3 are for metal work function pair of 5.5 eV and 4.0 eV. This choice depends on the work function of usable metals and of course, the work function of the nanowire itself. The larger the difference between the two metal work functions, the larger the asymmetry, and the better the photovoltaic properties. However, in practice not all metal combinations may ideally be suitable. For example, both gold and platinum have high work functions, but they concomitantly also reduce the charge carrier lifetime [76], [77] and thus may not be suitable as contact metals. On the low work function side, calcium and magnesium are highly reactive [78] and difficult to deposit since they oxidize very fast. Therefore, from a practical point of view, it is appropriate to study how work function differences affects solar cell behavior. Work function of the silicon nanowire can depend on many parameters such as etching time [79], chemical used in surface passivation, nanowire diameter [80], and doping. Silicon nanowire work function has been found to vary from about 4.5 eV to 5.01 eV [79], [80]. Work function of silicon microwire is taken from the bulk silicon, which has an electron affinity of 4.17 eV. Therefore, depending on doping type and concentration, the work function can vary from 4.17 eV (bottom of conduction band) to 5.25 eV (top of valence band) assuming a bandgap of 1.08 eV. In our study, we mostly consider the wire work function of 5.01 eV. This corresponds to bulk silicon with a p-type doping of $\sim 10^{15}\ \text{cm}^{-3}$. As explained through Figure 3.4 below, the work function of one metal should be below and that of the other metal should be above that value (5.01 eV). Thus considering a wire work function of 5.01 eV and work function range of usable metals, metal work functions of 5.5 eV and 4.0 eV are reasonable choices.

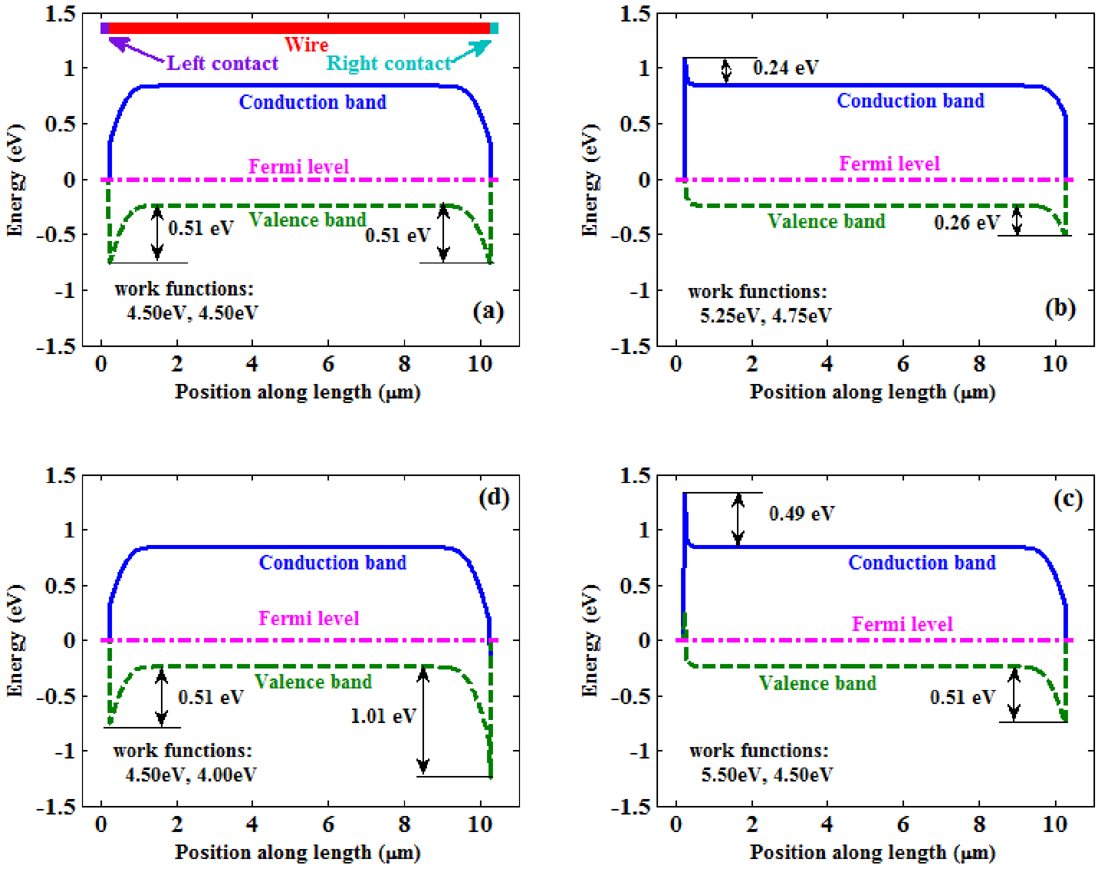

Figure 3.4. Conduction (solid), valence (dash) bands and Fermi level (dash dot) for a $10\mu\text{m}$ long wire. Contact work function pairs are 4.50 eV, 4.50 eV (a), 5.25 eV, 4.75 eV (b), 5.50 eV, 4.50 eV (c), 4.50 eV, 4.00 eV (d). Wire doping density is 10^{15}cm^{-3} (p-type, work function is 5.01 eV). Inset of (a) at the top shows the device schematic, and labels the contacts and the wire.

Figure 3.4 shows the conduction band (solid line) and the valence band (dashed line) as well as the Fermi level (dash dotted line) for a $10\,\mu\text{m}$ long wire. When there is no metal work function difference (Figure 3.4(a)), the two contacts are identical. If light is incident uniformly on such a device both the photo current and the photo voltage will be zero due to the symmetry of the bands. Figure 3.4(b) shows the case with work function of 5.25 eV for left contact (larger than silicon work function) and 4.75 eV right contact (less than silicon work function). Here electrons will prefer to flow towards the right contact while holes towards the left, resulting in a net photocurrent. If the barrier to the electron (hole) flow on the left (right) side is increased, photocurrent will also increase (Figure 3.4(c)). This is described in more detail in relation to Figure 3.8 below. If the work functions are chosen in such a way that bands at both ends bend in the same direction (Figure 3.4(d)), relatively smaller photocurrent will be produced and the device will be inefficient. Section 3.5 discusses guideline for choosing the metal work functions for improved short circuit current and open circuit voltage. It is also to be noticed that although the band bending in Figure 3.4 is due to proper metal work function selection, controlled doping may also produce similar effects.

To see the effect of the work function difference on the photocurrent, we have plotted the short circuit photocurrent of the microwire device (width = $1\mu\text{m}$ and height = 35 nm) as a function of its length in Figure 3.5(a). There are three curves for three metal contact work function differences. For a work function difference of 0.0 eV (dash dotted line), the current is zero, as can be expected from Figure 3.4(a). For a moderate work function difference of 0.5 eV (dashed line), there is a considerable amount of photocurrent. This should be expected from the band diagram of Figure 3.4(b). For a large work function difference of 1.5 eV (solid line), the current is even larger (see Figure 3.4(c)), especially before saturation at very long lengths. So the photocurrent increases with the work function difference.

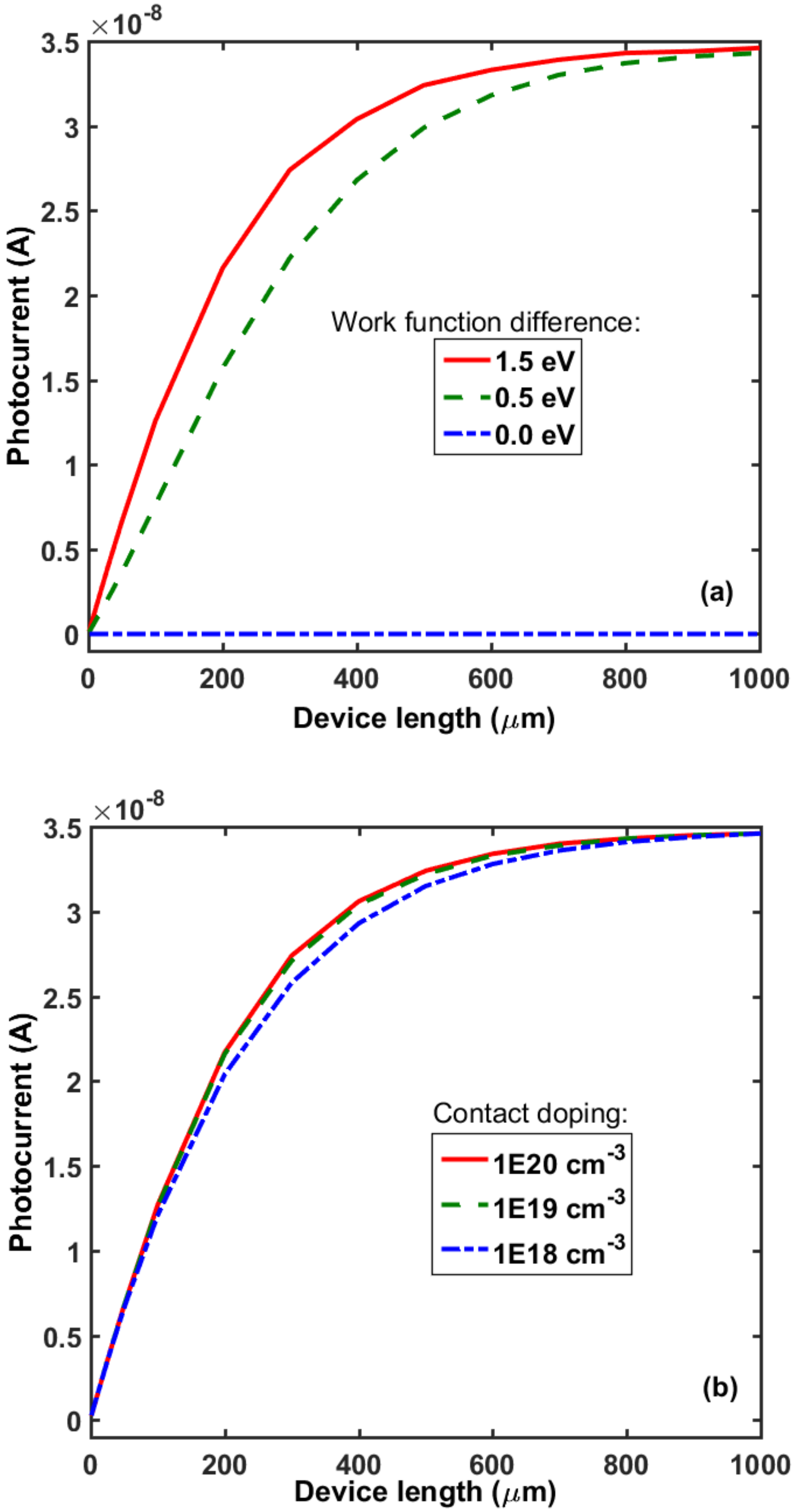

Figure 3.5. Effect of (a) work function and (b) contact doping on short circuit photocurrent versus device wire length.

Next we compare the effect of dissimilar doping at the ends of a wire with the effect of work function difference of the contact pairs. Figure 3.5(b) plots the short circuit photocurrent of the same wire as in Figure 3.5(a) for three different doping concentrations (10^{18} cm^{-3} (dash dotted line), 10^{19} cm^{-3} (dashed line), 10^{20} cm^{-3} (solid line)). Comparison of Figure 3.5 (a) and (b) reveals that metals with work function difference of 1.5 eV (work functions of 4.0 eV and 5.5 eV, solid line in Figure 3.5(a)) can give the same short circuit photocurrent as that produced by doping concentrations equal to or in excess of 10^{19} cm^{-3} (Figure 3.5(b), which makes the use of dissimilar metals an attractive alternative since controlled doping in nanowires is difficult [24]–[27] .

3.6 SHORT-CIRCUIT CURRENT AND OPEN-CIRCUIT VOLTAGE

Short-circuit current and open-circuit voltage are among the most important performance parameters of a solar cell. Short-circuit current (I_{SC}) is simply the photocurrent when the two electrodes are shorted to each other. Open-circuit voltage (V_{OC}) is the voltage across the device when the electrodes are open. In Figure 3.6, we consider both I_{SC} and V_{OC} of wires of two different widths: 1 µm (a) and 100 nm (b). The lengths of the wires vary from 1 µm to 1000 µm. Each wire has a height of 35 nm. The metal work functions are 5.15 eV (Nickel) and 4.15 eV (Aluminum). Figure 3.6(a) plots the 2D simulation results for the 1 µm wide wire. Note that 2D simulation is done on a vertical cross-section of area L times H of the wire (Figure 3.1). Since the height of the wire is still thin (35 nm), we also did the more computationally costly 3D simulation for this device (results not shown here). We have found that although the 2D and 3D results match closely, compared to 3D, the 2D simulations does tend to slightly overestimate both the I_{SC} and V_{OC}. Thus for the narrower wires, only 3D (Figure 3.6 (b)) simulations were done. I_{SC} for the 1 µm wide wire is about 10 times that of the 100 nm wide wire. Indeed, from 3D simulation of the wider wire, it is found that the current scales exactly linearly with the wire width. There have been several simulation studies [81]–[84] on optical absorption of single and multiple silicon nanowires as function of their diameter. Most works are on arrays of vertical wires [84] with core-shell geometry [81]. Simulations of core-shell single cylindrical wire predict [81] that there is an optimal wire radius for maximum current density. It was also pointed out that simulation of single nanowire may not capture all the physics present in an array of wires. Current per unit area was found to increase while current per unit volume was found to decrease with wire diameter in a study [84] of horizontal hexagonal wires. Simulation study [82] of arrays of cylindrical wires lying horizontally on a flat surface with wire to wire distance of 200 nm predicts enhanced absorption with increasing diameter, ranging from 50 to 160 nm. Our result is consistent with that study. For our single rectangular wire, lying horizontally on a flat surface, the surface area over which normal light is incident upon it is exactly proportional to its width. Thus the photocurrent generated by absorption of a uniform intensity light is proportional to the wire width.

For both wide and narrow nanowires, the I_{SC} first increases and then saturates with length. This is because as length increases, the probability of recombination of excess charge carriers also increases as they move towards their respective contacts. V_{OC}, as shown in the inset of Figure 3.6, has a trend similar to that of I_{SC}. This length is 800 µm for both I_{SC} and V_{OC} for minority carrier lifetime of 10 µm.

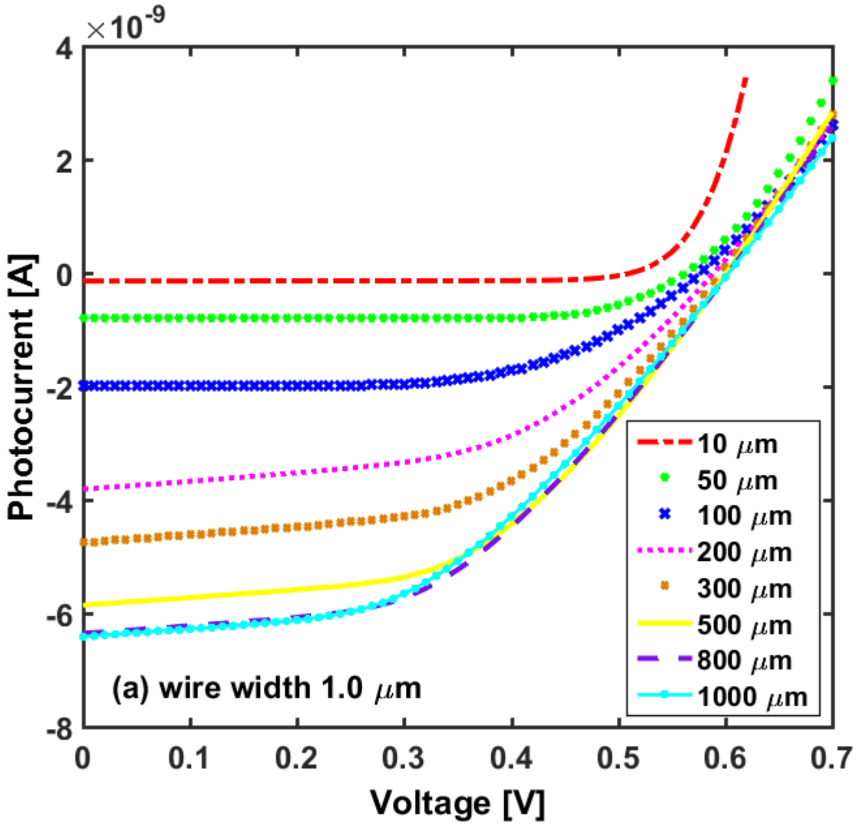
×10^-9
4
2
0
-2
-4
-6
-8
Photocurrent [A]
0
0.1
0.2
0.3
0.4
0.5
0.6
0.7
Voltage [V]
10 μm
50 μm
100 μm
200 μm
300 μm
500 μm
800 μm
1000 μm
(a) wire width 1.0 μm

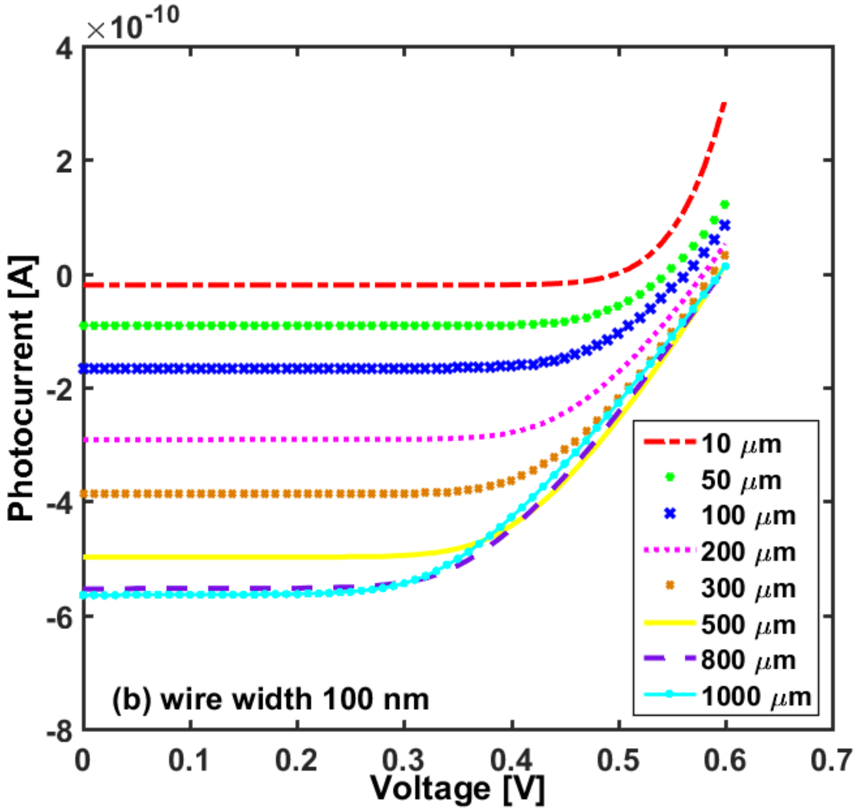
×10^-10
4
2
0
-2
-4
-6
-8
Photocurrent [A]
0
0.1
0.2
0.3
0.4
0.5
0.6
0.7
Voltage [V]
10 μm
50 μm
100 μm
200 μm
300 μm
500 μm
800 μm
1000 μm
(b) wire width 100 nm

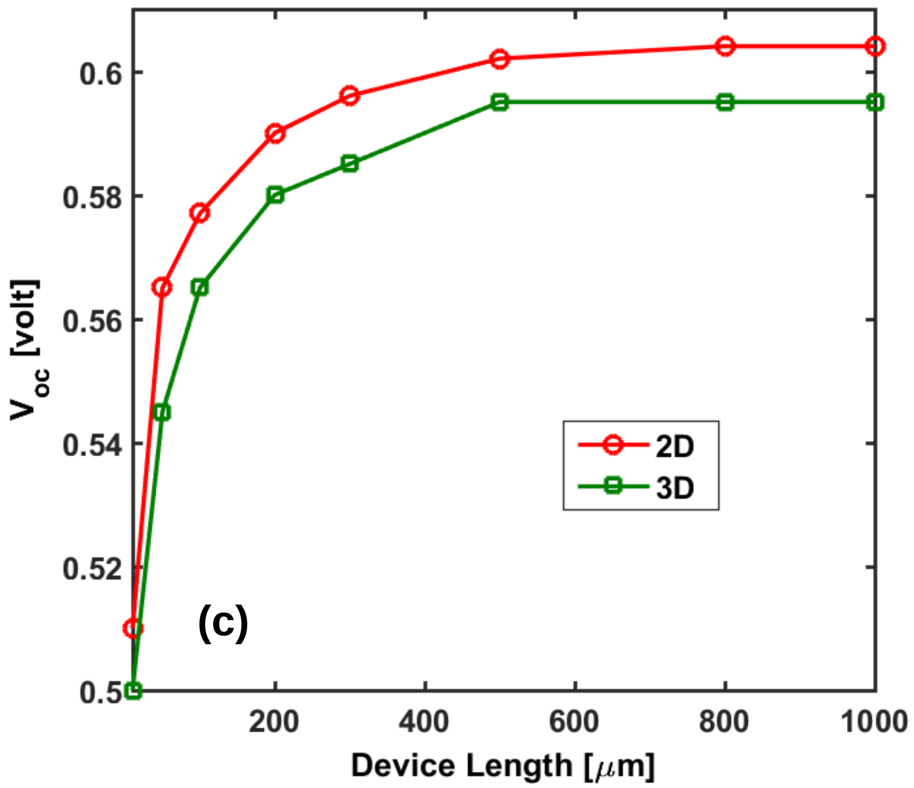

Figure 3.6. Photocurrent versus bias for different nanowire lengths: (a) 2D simulation of 1 micrometer wide wire, (b) 3D simulation of 100 nm wide wire. Open circuit voltage versus device length (c). Both wires have a height of 35 nm. Minority carrier lifetime is 10μs.

The behavior of Voc can be understood in terms of quasi-Fermi level splitting under illumination [22], [85]:

$$V_{OC} = \frac{kT}{q}\ln\left(\frac{np}{n_i^2}\right) = \frac{kT}{q}\ln\left(\frac{\Delta n(N_A + \Delta p)}{n_i^2}\right) \qquad (3.13)$$

where n (p) is the electron (hole) density, N_A is the p-type doping density, Δn (Δp) is the excess electron (hole) density due to illumination and n_i is the intrinsic carrier density. Similar expression holds for n-type doping. If the device is very long such that in steady state the excess carrier densities approach the value $G_L\tau$, then Eq. (3.13) becomes,

$$V_{OC} \approx \frac{kT}{q}\ln\left(\frac{(G_L\tau)\left(N_A+(G_L\tau)\right)}{n_i^2}\right) \tag{3.14}$$

Eq. (3.14) gives a limit on the available Voc. In an actual device, the closer the average excess densities are to $G_L\tau$, the closer its V_{OC} will reach the value given by Eq. (3.14). Figure 3.7 plots available, as given by Eq. (3.14), as well as actual, as calculated from simulation, Voc as a function of the AM1.5 light intensity for different wire lengths and two different work function differences between the two contact and the wire.

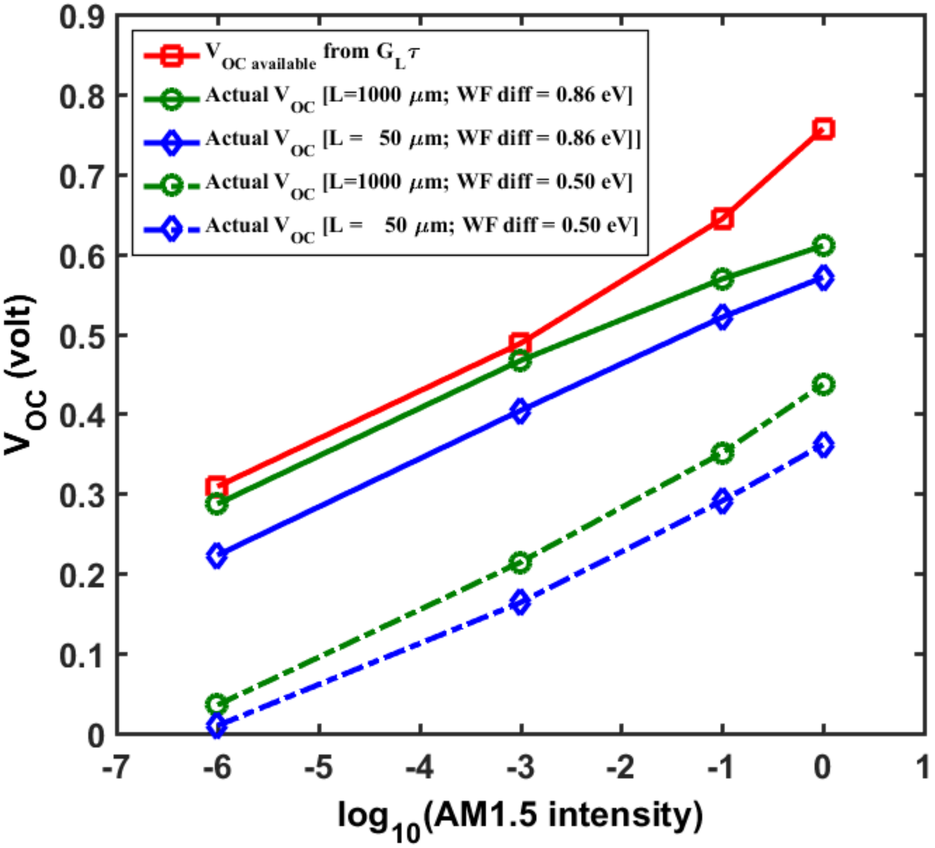

Figure 3.7. Available and actual open circuit voltages as a function of intensity. Wire doping density is 10^{15} cm^{-3} (p-type, work function is 5.01 eV). Lifetime is 10 μs .

Long wire with large work function difference approach the ideal device as can be seen for the case of $1000\ \mu\text{m}$ long wire with work function difference of 0.86 eV. For shorter wire ($50\ \mu\text{m}$), with the same work function difference, the voltage is lower. The reason is the shorter the wire the lower its excess carrier density is compared to $G_L \tau$.

Since appropriate contact work function values are so important for the nanowire solar cells, we discuss below how one may select the work functions to achieve larger I_{SC} and V_{OC}. The wire that we consider is $100\ \mu\text{m}$ long, $1\ \mu\text{m}$ wide and $35\ \text{nm}$ thick. The p-type doping density of the wire is $10^{15}\ \text{cm}^{-3}$ so that the Fermi level is fixed at 5.01 eV below the vacuum level (conduction band is at 4.17 eV and valence band is at 5.25 eV below). As discussed in Figure 3.4, in this case, work function of the Ohmic contact (W_O) should be below and the work function of the Schottky contact (W_S) should be above, the wire equilibrium Fermi level.

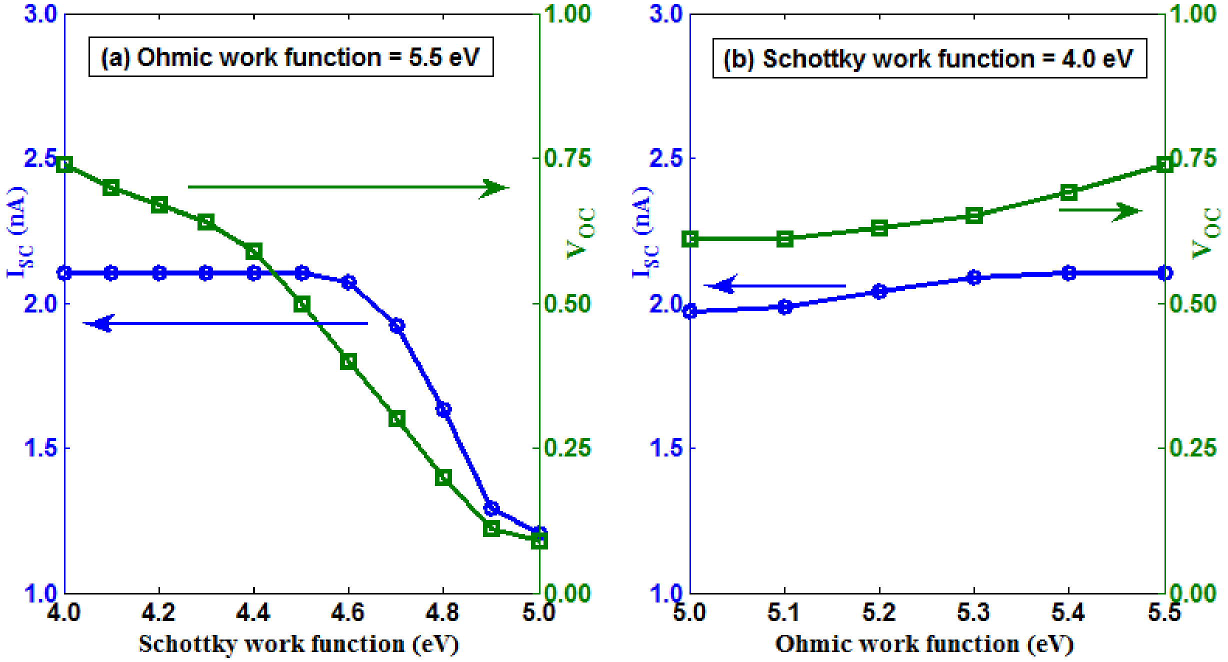

Figure 3.8. I_{SC} and V_{OC} as a function of (a) W_S, with W_O fixed, (b) W_O, with W_S fixed.

Figure 3.8(a) plots I_{SC} and V_{OC} as a function of the W_S with W_O kept fixed at 5.5 eV while in Figure 3.8(b) the W_S is fixed at 4.0 eV and W_O changes. As W_S moves above and away from the wire work function (Figure 3.8(a)), both I_{SC} and V_{OC} increase rapidly. But I_{SC} saturates when W_S is about 0.5 eV above the wire work function, while V_{OC} keeps increasing at a slower rate. On the other hand, variation in W_O (with a fixed W_S) does not produce as high a change in both the open circuit voltage and short circuit current (Figure 3.8 (b)). We find that I_{SC} saturates when W_O is 0.4 eV below the wire work function. Thus for efficient solar cell the work function of the Schottky contact is more important and should be as far away from the wire's work function as possible. The work function of the Ohmic contact although less important, can still cause a noticeable change in the V_{OC}, which should be kept in mind when selecting the metal.

3.7 SHORT-CIRCUIT CURRENT DENSITY

We have so far considered only the total currents of the individual devices (microwire and nanowire) without regard for their surface areas. Since the amount of device area exposed to light is very important for solar cells, we define a short circuit current density as

$$J_{SC} = \frac{I_{SC}}{LW} \tag{3.15}$$

where I_{SC} is the total short circuit current and J_{SC} is the short circuit current density. L and W are wire length and width, respectively. Note that this definition is different from short circuit current density used in conventional planar solar cells where the current flows perpendicular to the surface area. For the horizontally lying wires we considered in this study, the area in Eq. (3.15) is the area exposed to light (Figure 3.1), and the current flows parallel to this area.

We plot the short circuit current density (J_{SC}) for both the microwire and the nanowire devices for three different representative minority carrier lifetimes in Figure 3.9. In this plot, surface areas of the two metal contacts at the ends of the wire have not been taken into account. For a particular minority carrier lifetime, J_{SC} for both microwire and nanowire are the same, and thus I_{SC} scales with wire surface area, as discussed in relation to Figure 3.6. J_{SC} decreases as wire length increases, and the shorter the lifetime the faster the decrease. The reason is again attributed to the increased inefficient collection of photo-generated carriers as the length increases.

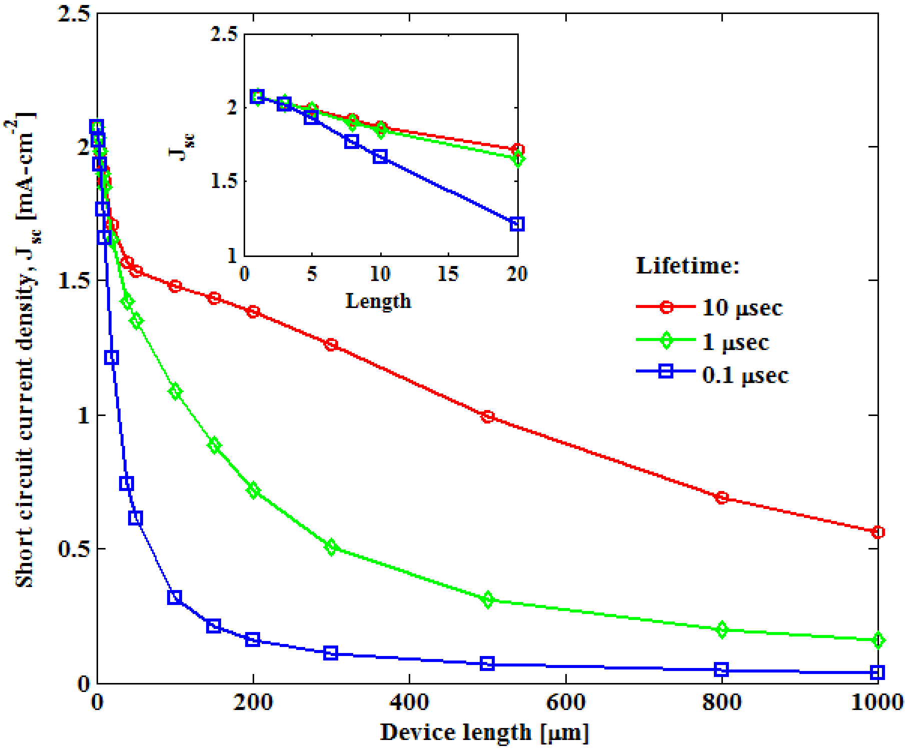

Figure 3.9. Short circuit current density versus wire lengths for three different minority carrier lifetimes. The wire has a height, H, of 35 nm.

As seen in Figure 3.3, the I_{SC} for a wire saturates at 5 times the diffusion length. However, when the surface area is taken into account, the carrier collection efficiency decreases rapidly with length. This implies that to obtain large current density per surface area, shorter wires are preferable. However, for greater current per nanowire, longer wires are preferable.

3.8 COMPARISON WITH REPORTED EXPERIMENTAL RESULTS

Kelzenberg et al. [12] measured both V_{OC} and J_{SC} for a single silicon nanowire of diameter 900 nm and length $20\ \mu m$ and it is interesting to compare our predictions with their measurements. However, there is one important difference: the reported work uses aluminum for both contacts, where one contact is electrically heated to get Schottky effect. Although we consider specific work functions corresponding to two distinct metals, it is equally applicable for same metal with different work functions. We simulate a wire of the same dimension with a minority carrier lifetime of 15 nsec, as given in [12]. For aluminum, the work function is approximately 4.15 eV. However, the work function of heated aluminum-silicon interface is not well understood [12] and the exact value is not available. Here a value of 4.52 eV gives a good match with the experiment: we find V_{OC} of 0.193V and J_{SC} of 4.2 mA/cm^2, which are comparable to published values of 0.19V and 5 mA/cm^2, respectively.

3.9 IMPROVING SHORT-CIRCUIT CURRENT

For long wires, saturation of short circuit current is a drawback. However, it is possible to make an improvement with simple device modifications. So far we have considered contacts only at the ends of the wire. Figure 3.10 depicts a sketch of a wire with additional metal contacts placed between the two ends. This contact arrangement essentially breaks a long wire into a few short nanowires electrically, with the cathodes connected together and the anodes connected together. This causes collection efficiency to increase since electrons and holes have to travel shorter distances.

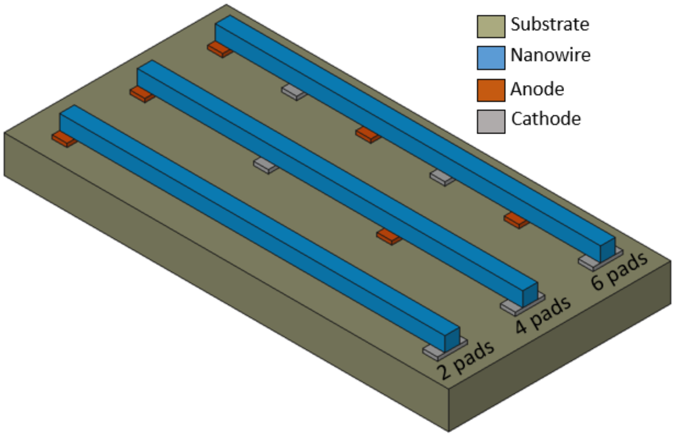

Figure 3.10. Electrically breaking a long wire into a few short wires.

Figure 3.11 plots both I_{SC} (a) and V_{OC} (b) versus the number of pads for nanowires of 6 different lengths. Here a minority carrier lifetime of 10 μs has been considered. For lengths below 220 μm, more than two pads decrease the current (Figure 3.11(b)). But for lengths 220μm and above, maximum current is obtained when more than two pads are used. The results in Figure 3.11(a) potentially imply that for wires with shorter lifetimes (more defects) employing multiple pads will improve collection efficiency even at shorter lengths. In addition, there is an improvement in fill factor (not shown) when number of pads equal or exceed the number required for maximum current. The V_{OC} vs number of pads plot in Figure 3.11(b) indicates that for wire length of 500μm or larger, open circuit voltage is greater for more than two pads. For number of pads maximizing the short circuit current (Figure 3.11(b)), V_{OC} is still larger than its value with two pads, if length is 500μm or larger.

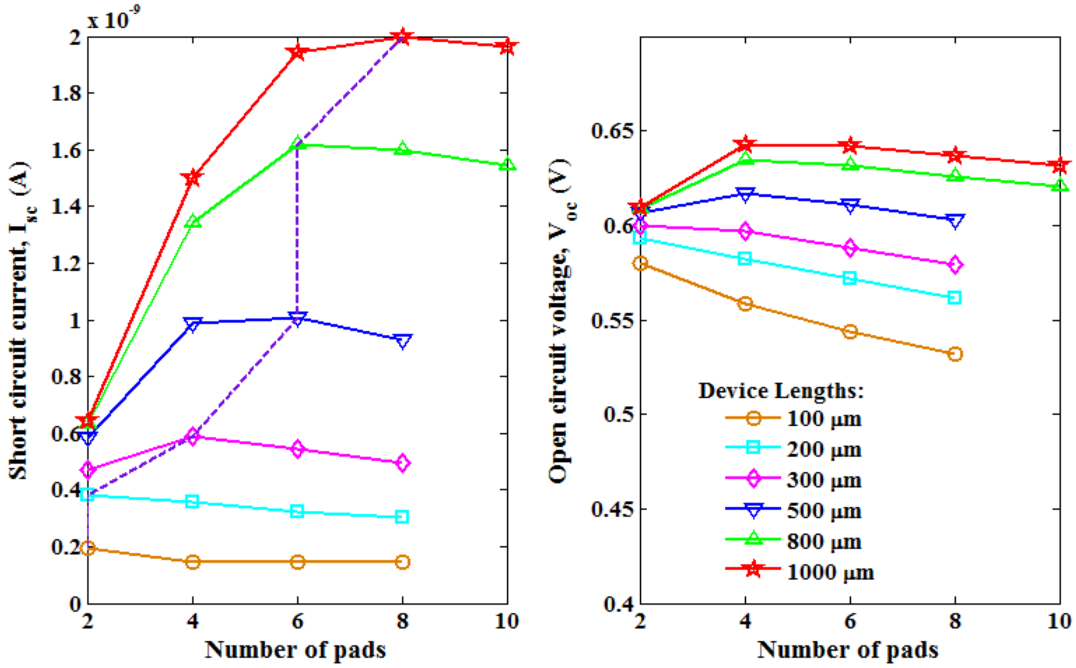

Figure 3.11. Short circuit current (a), and open circuit voltage (b) as a function of number of pads for six different nanowire lengths. The wire widths and heights are fixed at 100nm and 35nm, respectively. Minority carrier lifetime is $10\mu s$.

Electrically connecting silicon wires in series or parallel can be done using current technologies. A long silicon wire that is electrically broken by an interdigitated electrode pattern, as discussed above, may be thought of as a series connection of many smaller wires. The fabrication of millimeter long silicon nanowires has been reported in [86]–[89]. Electrode pattering for the long wires follows well defined fabrication procedures. On the other hand, arrays of silicon nanowires between two electrodes can be viewed as a parallel connection of those nanowires. Such arrays (or mats) have demonstrated optical properties that make them attractive candidates for solar cells, such as enhanced optical absorption [6]. These are discussed in Chapter 4.

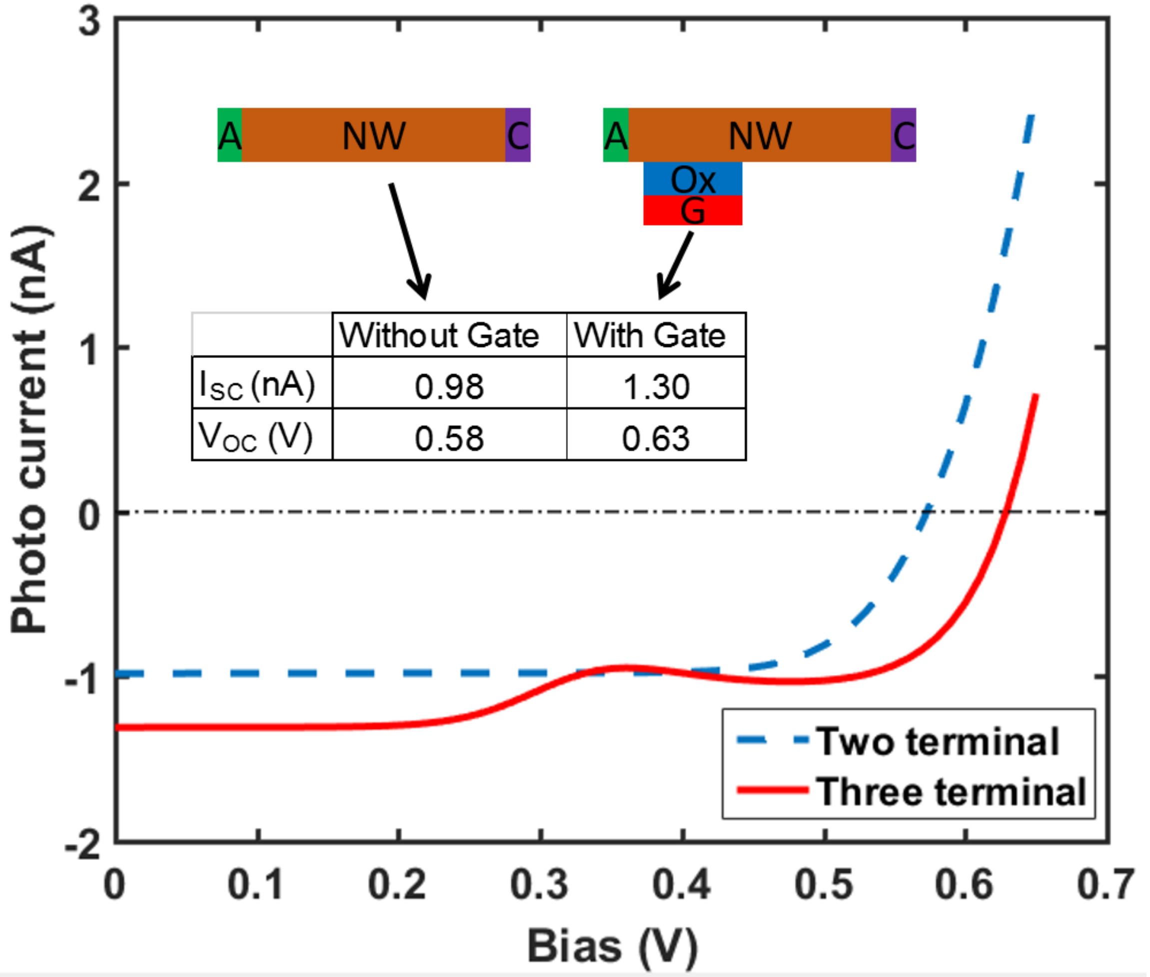

	Without Gate	With Gate
I_{SC} (nA)	0.98	1.30
V_{OC} (V)	0.58	0.63

Figure 3.12. Grounded gate electrode improves both short circuit current and open circuit voltage.

Another approach to improving both I_{SC} and V_{OC} is as follows. For each nanowire (or a portion of it between consecutive anode and cathode electrodes), instead of having just two contacts, a third contact, a gate, is added as shown in the cartoon in Figure 3.12, which also plots the photocurrent of both the two-terminal and three-terminal devices. Here the gate terminal is physically closer to the anode but tied to the cathode, i.e., grounded. Its mere presence though causes a well in the equilibrium band structure of the device and enhances both I_{SC} and V_{OC}. The price however is added fabrication steps to make the gate contact.

3.10 CONCLUSION

Nano and microwire photovoltaic devices have been investigated. The use of two dissimilar-metal contacts, with dissimilar work functions, for these devices is seen to be an excellent alternative to dissimilar doping at the two ends of the wire. This implies that issues related to fabrication reliability of such devices can be significantly reduced because controlled doping in nanowires is difficult and expensive. The behavior of nanowire photovoltaic devices is found to be dependent on the wire length for short wires. However, as wire length increases, both the short circuit current and open circuit voltage saturate. This saturation length is found to be approximately five times the minority charge carrier diffusion length, and suggests an upper bound on the achievable photocurrent. This bound can be overcome through modifications of the basic structure. Use of interdigitated patterns of dissimilar metals for a very long wire is seen to significantly increase the short circuit current, while keeping the open circuit voltage nearly constant. This is attributed to increased collection of charge carriers before they recombine. Finally, it is shown that adding a grounded gate terminal can improve short circuit current as well as open circuit voltage at the cost of added fabrication complexity.

Chapter 4. ZERO-BIAS PHOTOCURRENTS IN HIGHLY DISORDERED NANOWIRE NETWORKS

Semiconducting nanowire (NW) devices have garnered attention in self-powered electronic and optoelectronic applications. This chapter explores and exhibits, for the first time for visible light, a clear evidence of the zero-biased optoelectronic switching in randomly dispersed Ge and Si NW networks. The test bench, on which the NWs were dispersed for optoelectronic characterization, was fabricated using standard CMOS fabrication process, and utilized metal contacts with dissimilar work functions - Al and Ni. The randomly dispersed NWs respond to light by exhibiting substantial photocurrents and, most remarkably, demonstrate zero-bias photo-switching. The magnitude of the photocurrent is dependent on the NW material, as well as the channel length. The photocurrent in randomly dispersed GeNWs was found to be higher by orders of magnitude compared to SiNWs. In both of these material systems, when the length of the NWs was comparable to the channel length, the currents in sparse NW networks were found to be higher than that in dense NW networks. The measurement results are explained by metal work function measurement and considering various possible arrangements of NWs in the devices.

4.1 INTRODUCTION

Semiconducting nanowires, which offer long absorption paths along their length yet shorter distances for carrier collection/transport[67], [90], have been widely studied for prototype applications, such as solar cells[91], photo-detectors[92] and nanolasers[93]. Often, these studies encompass single NWs and involve complex and costly nano-fabrication and ultra-sensitive measurements to achieve unique applications such as single-photon optics[94], self-powered photo detection[92], etc. However, given the fabrication challenges with single NWs, the potential of

NW-based devices comprised of NW mats, networks or randomly dispersed NWs (RDNWs)[95] needs to be understood and exploited. The NW networks, mats and RDNWs are relatively cheaper and simple to fabricate and also have important scientific and technological advantages over single NWs, such as effective light trapping and refractive-index matching[95], [96]. Chemical sensors fabricated from NW mats are more sensitive than that of single NW devices[16]. Other advantages of networks and mats are that they are relatively strong and flexible, self-supported, and thin (approximately 50 µm) with ~90% void space, which can absorb most of the light from the ultraviolet (UV) to near-infrared (IR) wavelength ranges[97].

An important aspect of nanoscale materials, such as NWs, is their behavior at interfaces, which often overrides the active nano-material physics and can potentially alter the overall performance of the electronic and optoelectronic devices[98]. In optoelectronic applications, the interfaces are generally the electronic contacts to the NWs, which collect photo-generated electrons and holes upon illumination of semiconductor NWs. The interfaces and their influences on the overall device performance have been studied in electronic devices, even at the nanometer scale[99], [100], and observations have shown that nano-contact resistance can dominate the overall electrical properties.

Apart from collection of charge carriers, the idea that work-function asymmetry in contacts can induce an electric field in the active channel—which in turn directs carriers—has attracted the attention of the optoelectronic research community. Note that such an asymmetry in bulk semiconductors is achieved by chemical doping, which becomes extremely difficult to control at the nanoscales. A recent modeling study of dual-metal Schottky contacts for nano and micro-wire solar cells[101] reported that dissimilar metal contacts can be an excellent alternative to dissimilar doping, which in turn enhances the fabrication reliability, particularly where nanoscale materials are involved. The experimental investigations of asymmetric contacts for photo-switching behavior have been carried out in single NW devices[102]–[104]. However, for nanowire networks, observation of photo-switching has only been limited to ZnO NWs that too only for UV excitations[105]. This effect is largely due to the inherent losses originating from misalignments and inter-NW transport, which is not clearly understood.

Over the last two decades, NW synthesis has advanced considerably. Vapor-liquid-solid (VLS) growth is predominantly used for synthesis of one-dimensional structures of all kinds of materials[32], [106]–[109]. Another method is the so-called supercritical fluid-liquid-solid (SFLS) approach[110], [111]. The VLS method is slow and expensive, whereas SFLS has better control over NW size (i.e., diameter heterogeneity) and allows for the synthesis of large (industrially relevant) quantity of NWs[110]. NWs synthesized in the SFLS approach are single-crystalline[110], [111] and can be free of metal particles[112]. It is also possible to synthesize NWs of compound materials[111], and surface modifications[113], [114] can be done simultaneously with synthesis. However, NWs synthesized by the SFLS route have not been extensively explored for device applications as have NWs synthesized through VLS.

In this chapter, we report the detailed experimental characterization of the optoelectronic switching response of highly disordered networks of SFLS-synthesized Ge and Si NWs between asymmetric work-function contacts under red light excitation. The effect of density of the networks and distance between contacts on the performance is also investigated. The rest of the report is organized as follows: Section 4.2 presents details of NW synthesis and RDNW-based device fabrications, section 4.3 demonstrates and discusses the results of photo-response in Ge and Si RDNWs, followed by the section 4.4 that summarizes and concludes this chapter.

4.2 EXPERIMENTAL

4.2.1 *Synthesis of GeNWs and SiNWs*

Ge and Si NWs were synthesized via metal nanocrystal-seeded SFLS method using diphenylgermane (DPG) and monophenylsilane (MPS), respectively, as the precursors. To synthesize Au-seeded GeNWs (diameter=45±15nm and few to several tens of microns long), the reactant solution was prepared using 16 mg/L of Au nanocrystals and 34 mM DPG (Gelest, > 95%) in anhydrous toluene. The synthesis reaction was carried out at 380°C, 6.2 MPa and at a flow rate of 0.5 mL/min for 40 min. Subsequently, the reactor was allowed to cool isochorically to 80°C for surface passivation via thiogermylation[115]. Inside a glovebox, a solution was prepared containing 8 mL of anhydrous toluene and 4 mL of 1-dodecanethiol (Sigma-Aldrich, ≥98%) as a passivating agent. The passivation solution was injected into the reactor at a flow rate of 2 mL/min, until the pressure returned to 6.2 MPa (the exit valve of the reactor remained closed during injection). The reactor was then sealed and kept at 80°C for 2 h. The NW products were removed and were washed three times by dispersion in a solution of toluene, hexanes, and chloroform (2:1:1) and precipitated via centrifugation between each washing step.

The Sn-seeded SiNWs were synthesized with MPS according to a procedure described by Bogart et al.[116]. In a typical synthesis, a reactant solution containing 30 mL of anhydrous toluene, 500 μL of MPS and 96 μL of bis(bis(trimethylsilyl)amino)tin ($Sn(HMDS)_2$, Sigma-Aldrich, 99.8%) was prepared inside an argon-filled glovebox and placed inside a stainless steel injection cylinder. This solution was fed to a titanium reactor filled with anhydrous toluene at 490°C and 10.3 MPa, at a rate of 0.5 mL/min for 40 min. Afterwards, the reactor was cooled, the contents extracted, and the product washed as in the case of the GeNWs. Physical characterizations of NWs synthesized in the above processes have been reported in detail elsewhere [113], [115], [116].

4.2.2 *Fabrication of dual-metal test benches on oxide*

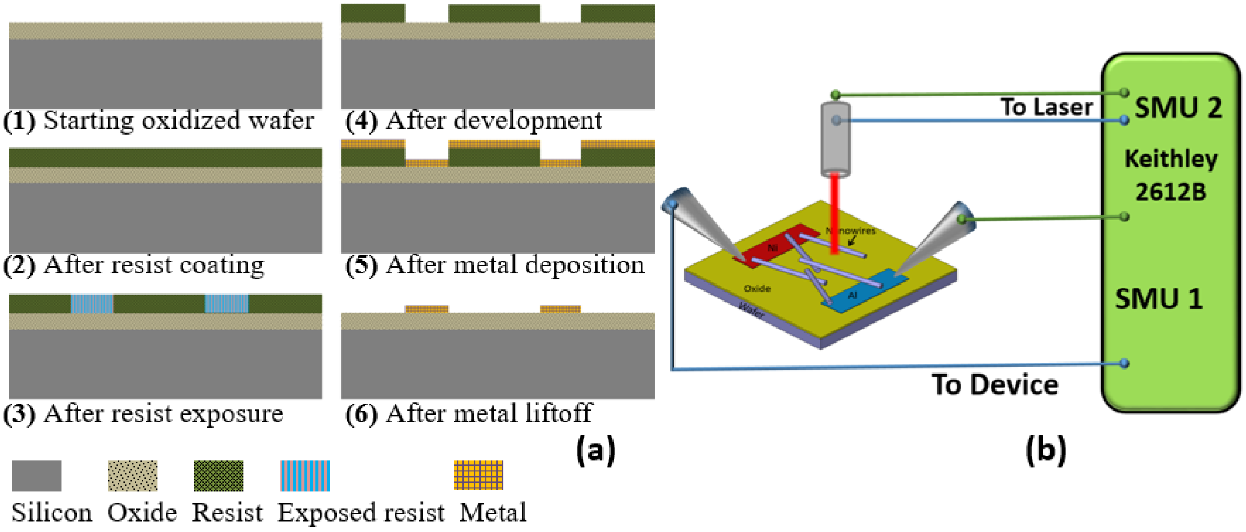

Figure 4.1. (a) Fabrication steps for metal patterns on an insulating substrate, (b) I-V measurement setup.

Figure 4.1(a) describes the fabrication steps of the metals-on-oxide test bench. Fabrication started with <100> Boron doped silicon wafer (resistivity of 1 to $5x10^{-3}$ Ohm-cm) of 100 mm in diameter and 500 µm in thickness. The silicon wafer was wet oxidized to form a $1\,\mu m$ SiO_2 layer on the top surface. The oxidized wafer was then cleaned with a nitrogen gas blower and primed with hexamethyldisilazane **(**HMDS) in a hot oven to enhance photoresist adhesion. Next AZ1512 photo-resist was spin coated at 3000 rpm for 45 seconds, which yielded a resist thickness of approximately$1.2\mu m$. Immediately after coating, the wafers were baked at 100°C for 60 seconds on a hot plate. The resist-coated and baked wafers were exposed to UV light dose of 70 mJ/cm^2 with an AB-M aligner. The exposed resist was developed in MF319 developer for 30 seconds followed by removal of developed resist residue by discommending the wafer in a barrel Asher for 2 minutes with a power of 50 W and oxygen pressure of 1 Torr. Then the desired amount of adhesion and metals were deposited by using an electron-beam evaporator. Finally, the wafers were soaked in acetone to remove the unwanted metal along with the resist to obtain the desired metal patterns on the oxidized surface. The same steps were repeated for each metal patterned wafer used in this study. The first metal was Al (250 nm) with 15 nm Ti as an adhesion layer while the second metal was Ni (250 nm) with 15 nm Cr as an adhesion layer. Note that fabrication based on photo-lithography is good enough to pattern the electrode gaps $(10\mu m - 100\mu m)$ used in this study; one may use e-beam lithography for even shorter gaps and better metal edge precision.

4.2.3 *Preparation of nanowire suspension, and dispersion*

For GeNW as well as SiNW, two types of suspensions, differing in NW density, were prepared by adding known weights of NWs, i.e., 15 mg and 5 mg, into a measured amount of toluene, 15 mL. Each of the mixtures was then sonicated for 5 minutes to obtain a uniform suspension of the NWs in toluene. Note that sonication also shortens the NWs, and therefore, for each sonication, a virgin suspension was used. Then, 2 μL of NW-in-toluene suspension was dispersed over the gap between Al and Ni contacts patterned on an oxidized Si surface, whose fabrication is described above. After the dispersion, the NWs settled out of solution via sedimentation and bridges the metal gap. The samples were kept as is for 24 hours to allow the toluene to evaporate completely. Although one can clearly see the NW density difference between the two cases in the SEM images in section 4.3, the actual number of NWs between the metal pads in a device does not necessarily follow the precise ratio of NW amount to toluene.

Note that the proposed device fabrication process is relatively simple, and the test bench can also be reused after a quick wash-off of the NWs. Table 4.1 lists the samples that were studied.

Table 4.1. Ge and Si NW samples studied in this chapter. The terms Dense and Sparse used in the text refer to the concentrations in this table, unless explicitely stated otherwise.

Sample Name	**NW Amount (mg):Toluene (mL)**
GeNW	1:1 (Dense), 1:3 (Sparse)
SiNW	1:1 (Dense), 1:3 (Sparse)

4.2.4 *Measurement setup*

The NW bridged metal-on-oxide devices were characterized both in dark and light conditions. Red laser diode was used as light source, with wavelength of 650 nm, power of 200mW, and spot size (diameter) of approximately 4 mm. Keithley source measure unit (SMU) 2612B was used to apply voltage across the gap between Al and Ni contacts, as well as to drive the laser diode. The same SMU was used to measure the currents. The setup shown in Figure 4.1(b) sat on an optical bench. Throughout the study, Al and Ni are employed as negative and positive electrodes, respectively. The Al-to-Ni distances (or device lengths) of 100 µm and 10 µm were considered. Because the laser spot size (~4 mm) was much larger than the device dimensions (100 µm and 10 µm), a uniform illumination over the entire RDNW device was attained. All the measurements were carried out in the ambient air at room temperature.

4.3 RESULTS AND DISCUSSIONS

4.3.1 *Photo response in RD-GeNWs*

Figure 4.2 displays the mesurement results for dense RD-GeNWs with 100-µm electrode gap. The scanning electron micrograph (SEM) image of the device is in Figure 4.2(a). GeNWs tended to clump together upon dispersion. Figure 4.2(b) shows that the current-voltage (I-V) charecteristics are almost symmetric[117], and the photocurrents and dark currents increase non-linearly with bias. Such non-linearity is probably due to the work-function difference between the NW and metal contacts[118]. At a bias of 5 V, the photocurrent is approximately 85 nA compared to the dark current of approximately 40 nA.

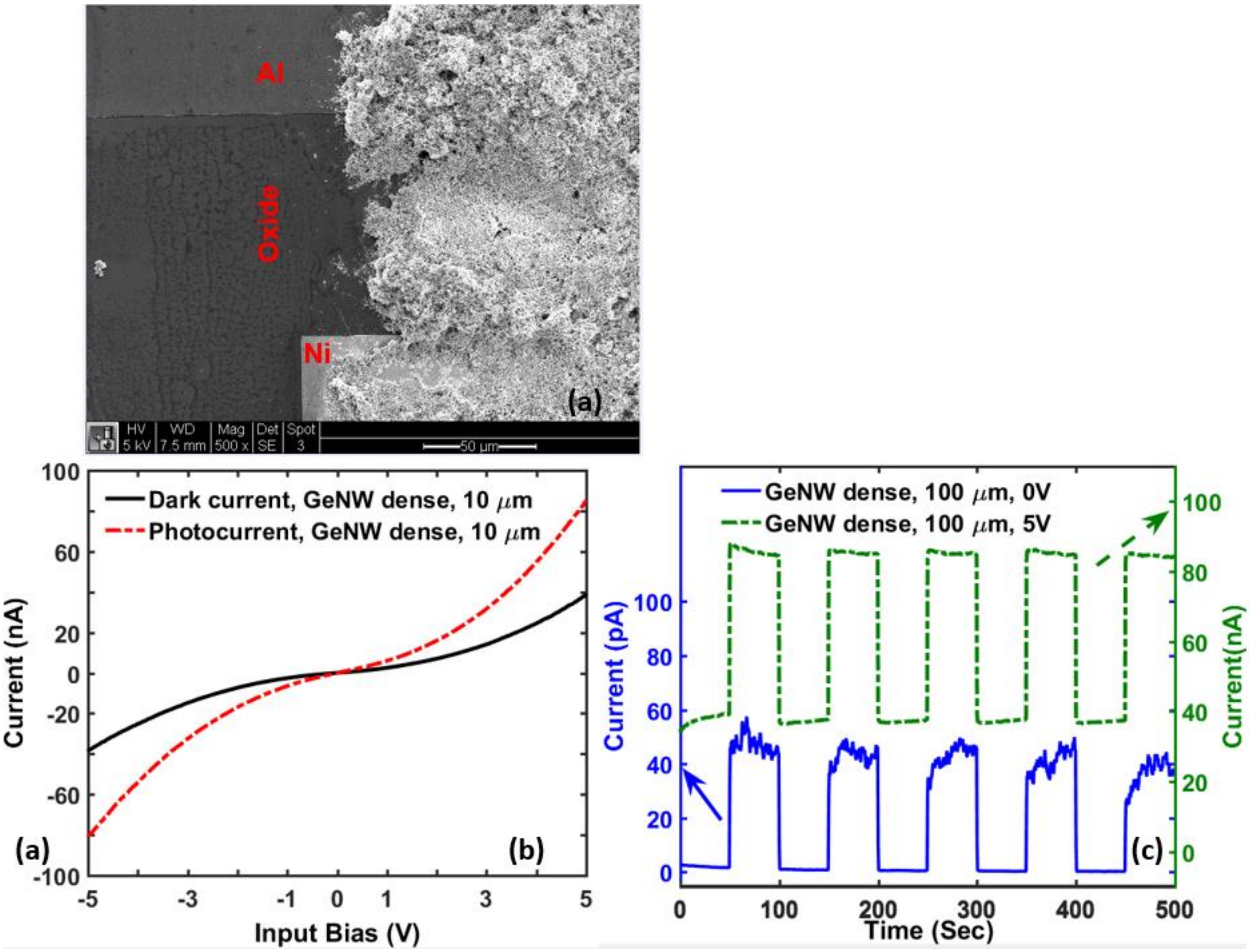

Figure 4.2. (a) SEM image of dense RD-GeNWs with Al and Ni contacts (100 µm), (b) I-V characteristics in the dark (solid) and light (dashed), and (c) light switching at zero (blue solid, left y-axis) and 5 V (green dashed, right y-axis) bias in a dense RD-GeNWs device.

More interestingly, Figure 4.2(c) shows the optoelectronic switching response of the RDNWs at zero bias and at a bias of 5 V. At zero bias, a significant photocurrent, ~40 pA, is observed. The zero-bias photocurrents in these highly disordered NWs indicate the effectiveness of using metal electrodes with different work functions. Notably, a mere random dispersion of NWs on dissimilar metal pads can extract such a high and distinct photocurrents at room temperature under visible-light illumination, even when no external bias is applied[118].

The results from a sparse network of RD-GeNWs are shown in Figure 4.3. An SEM image of a sparse GeNW device with a gap of 100 µm between the Al and Ni pads is shown in Figure 4.3(a). The sparse GeNWs led to a decrease in the currents (Figure 4.3(b)) by ~2 orders of magnitude when compared to that of a denser GeNWs. The zero-bias photocurrents also decreased to approximately 1.5 pA. The reduction in current is apparently due to the relatively small number of active channels available for light absorption and for carrier transport. However, the switching response is still distinct and stable.

The NWs used in this study are typically several micrometers to tens of micrometers long, as noted in the synthesis section. Therefore, for a 100 µm electrode gap, no single NW can contact both electrodes directly (also evident from SEM images in Figures 4.2(a) and 4.3(a)). If, however, the gap is shorter than the NW length, it is likely that many individual NWs can directly contact both the electrodes, which can further improve the photoresponse. To test this proposition, the same NWs were deposited on a device with a 10-µm electrode gap setup (Figure 4.4(a) and (b)), and the optoelectronic response was measured. Figure 4.4(c) and (d) show the currents in both dense and sparse, 10-µm gap, RD-GeNW devices. Figure 4.4(c) shows the dark and photocurrents versus bias, while 4.4(d) plots the zero-bias photo-switching results. For the dense devices, the both photocurrent and the dark currents at 5 V (Figure 4.4(c)) increased by a factor of ~5 when compared to those of the 100-µm gap device (i.e, Figure 4.2(b)).

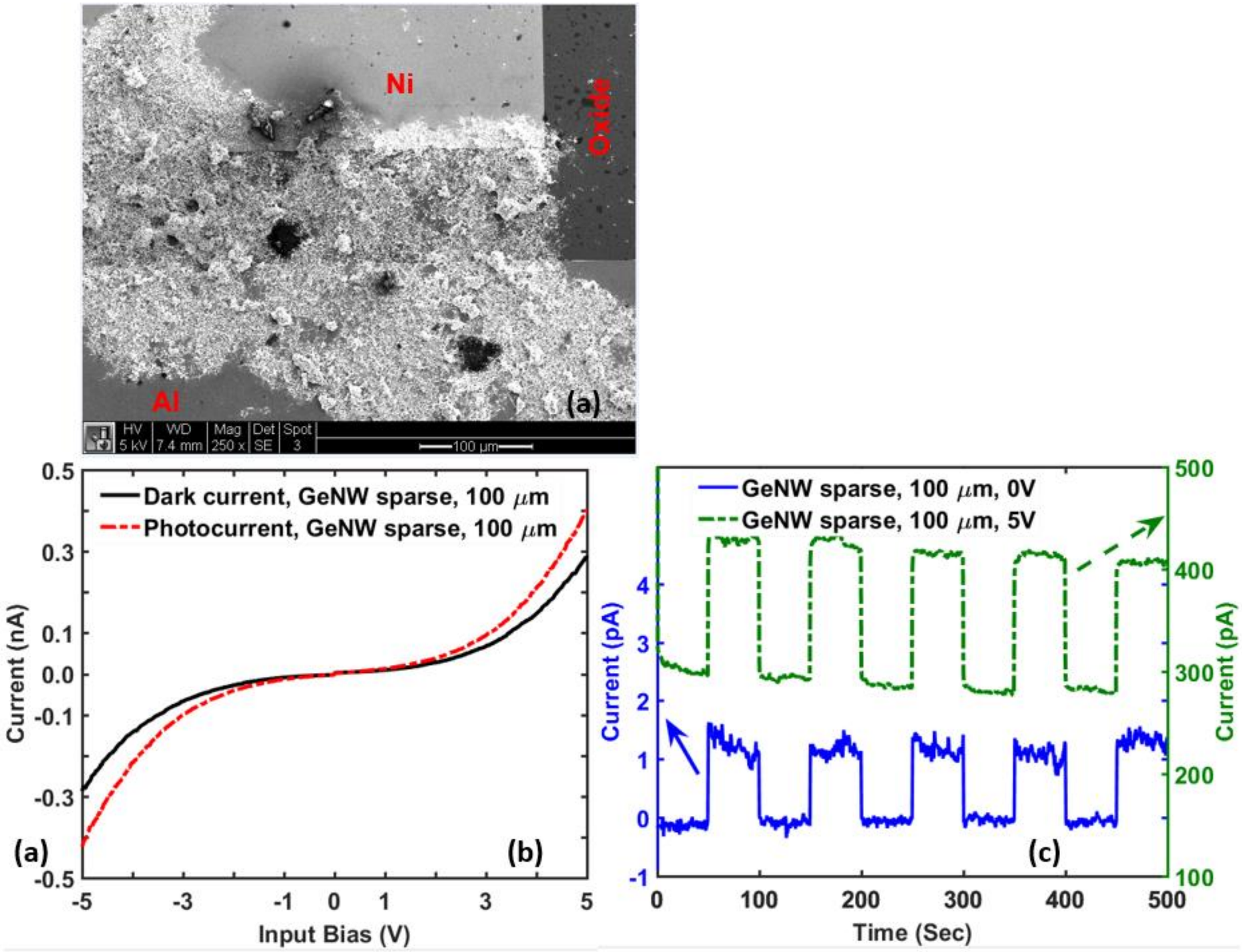

Figure 4.3. (a) SEM image of sparse Ge-RDNWs with Al and Ni contacts (100 µm), (b) I-V characteristics in the dark (dashed) and light (solid), (c) Light switching in sparse Ge-RDNWs device at 5 V (green dashed, right y-axis) and zero bias (blue solid, left y-axis).

However, the zero-bias photocurrent doubled. This finding confirms that devices with electrode gaps comparable to the length of the NWs more effectively produce a photocurrent than devices with a longer electrode gap. Similar channel-length dependence has been observed in carbon nanotube networks[119]. Although, due to the reduced area of the absorbing region, there are fewer photogenerated carriers available for the shorter device — the greater degree of direct, end-to-end contact between the NWs and both electrodes, as well as the stronger electric field that collects carriers more efficiently, more than compensated for this deficit in photogenerated charge carriers. Hence, greater absorption in long NWs might not always produce the expected higher photocurrent because carriers can only be collected from a distance on the order of the diffusion length[101]. Therefore, it can be inferred that, for the devices based on RD-NWs with asymmetric metal contacts, electrode-to-electrode distances smaller than the average NW length are more effective for photogenerated charge-carrier separation.

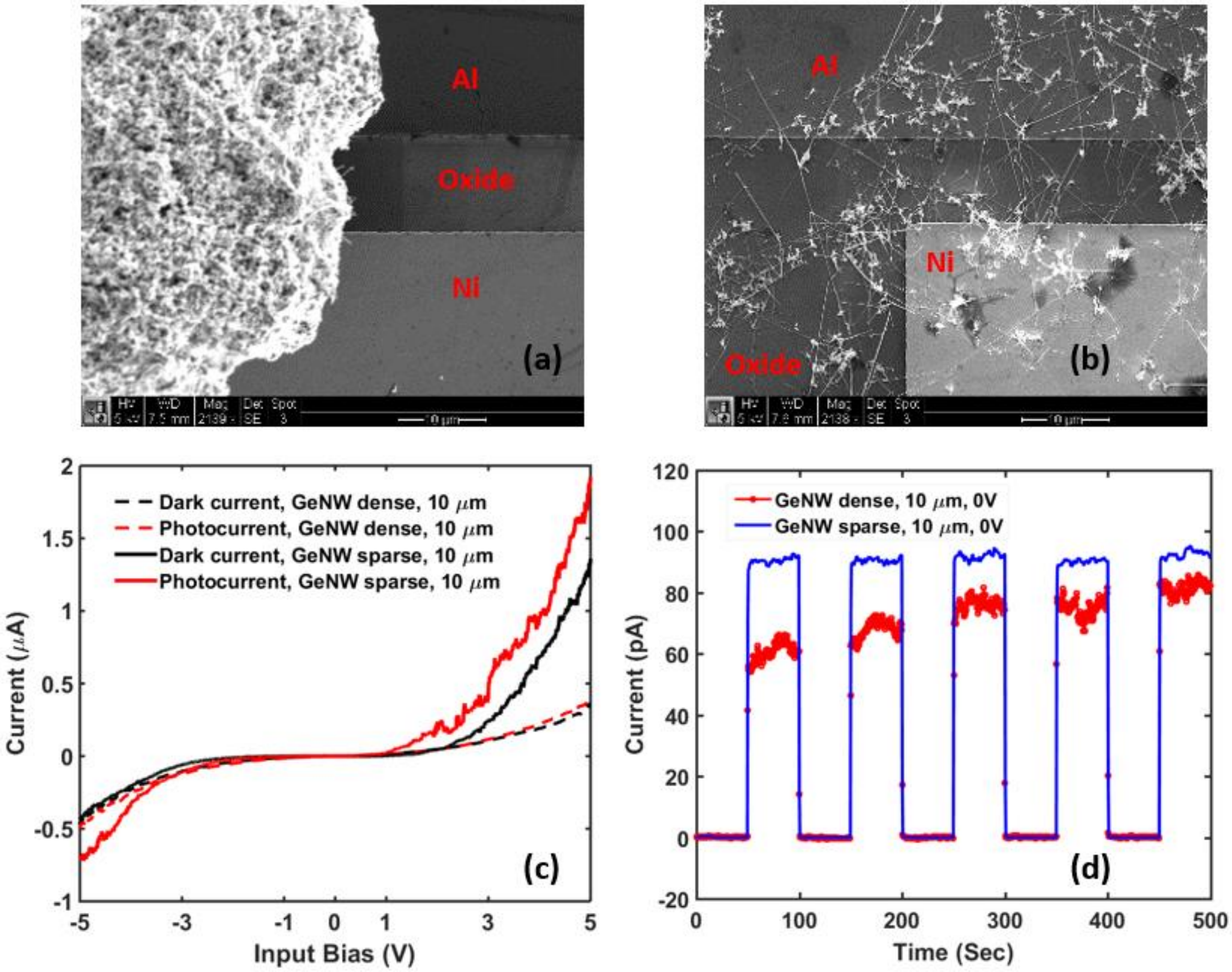

Figure 4.4. SEM images of dense (a) and sparse (b) RD-GeNW devices with 10 μm metal gap, (c) I-V characteristics in dark and light, and (d) light switching at zero bias.

Moreover, an unexpected observation can be made when comparing the responses of the dense and sparse NW networks in Figure 4.4. It is often anticipated that the dense NW network has more channels to carry current and can also trap photon more efficiently[95]. However, under a bias, the decrease in the number of dispersed NWs led to a significant increase in the current. The zero-bias photocurrent is also higher in the sparsely coated device (Figure 4.4(d), solid blue line).

To confirm that this particular result is generic, and not specific to GeNWs, SiNW network devices were characterized.

4.3.2 *Photo response in RD-SiNWs*

Figure 4.5 shows the results for SiNW devices with a 10 µm electrode gap. The SEM images of the dense and sparse SiNW network devices are shown in Figure 4.5 (a) and (b), respectively, while the dark and photo currents are plotted in Figure 4.5 (c) and (d). As in GeNW, the dense I-V characteristics are more symmetric than those of the sparse device. The SiNW networks also exhibit good photo-switching (Figure 4.5(e) and (f)). Here again, sparse NW devices also consistently produced more current than the dense devices; the photocurrent (at 5V bias) from the sparse NW network (~1.5nA) is almost an order greater than that of the dense (~200 pA) network. However, the current in the SiNW devciess is still lower than that in the similar GeNW devices (Figure 4.4(c)) because Ge has a greater conductivity as well as better optical absoprtion. The native Ge oxide is also less stable[120] than the native Si oxide and might allow for better NW-to-NW conductivity in GeNWs.

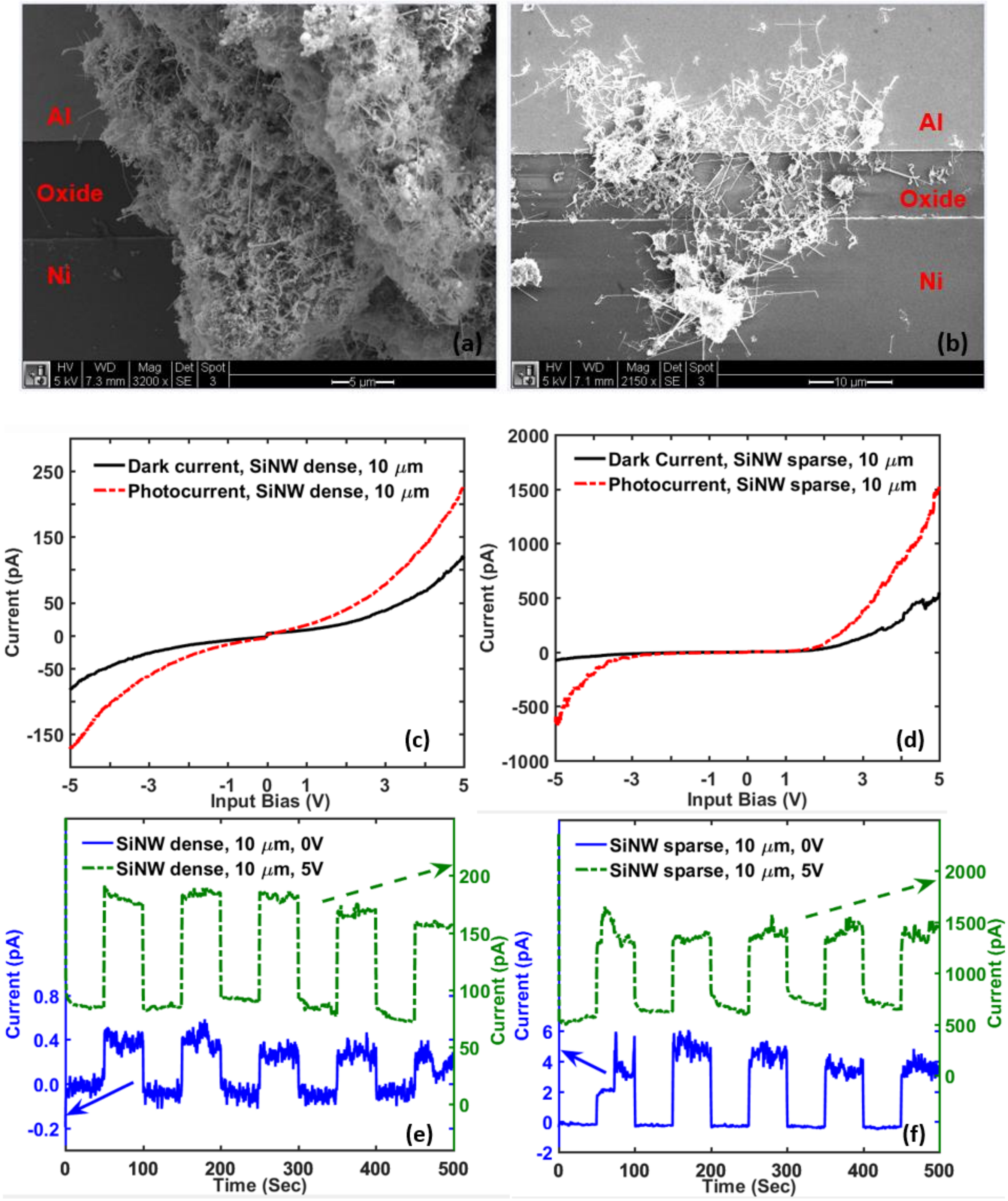

Figure 4.5. SEM images of dense (a) and sparse (b) RD-SiNWs devices. I-V characteristics in the dark and light for both (c) dense and (d) sparse SiNW devices with a metal gap of 10 μm. The 5 V and zero-bias photo switching responses for the dense (e) and sparse (f) devices are also shown.

4.3.3 *Measurement of metal work function*

Since metal work function difference plays a significant role in zero bias photocurrent, as modeled in detail in Chapter 3 and also supported by photo response results in this Chapter, it was important to get an estimate of what work function difference we could achieve with our choice of metals, namely Nickel and Aluminum. To that end, we did Kelvin Probe Force Microscopy (KPFM) which can measure workfunction of a surface with respect to the work function of an AFM tip [121]. For two metal surfaces, thus, we can get their workfunction difference. Figure 4.6 plots the KPFM surface scan result of a device. The device has Nickel and Aluminum deposited on an oxide surface, with metal to metal distance of 2 µm. No nanowire dispersion has been done on top of the metals, and a short (~5 second) buffered oxide etch (BOE) was done just before the KPFM measurement to have as clean a metal surface as possible. The KPFM surface scan in Figure 4.6(a) shows the AFM profile with the surface potential plotted as a color variation. The leftmost dark region is Ni, the middle reddish region is the gap (oxide) and the light orage on the right is the Al. Figure 6(b) plots the scan data along the horizontal line in Figure 6(b). We see that the potential difference between Al (right) and Ni (left) is ~0.7 eV. The nominal work function difference between Ni and Al is ~ 1 eV, so the measured value is quite acceptable, although not very accurate. The reason for discrepancy may be due to quality of deposited metals as well as presence of some native oxide, especially on Al. The KPFM measurement suggests that the two metals, when bridged by a semiconducting material such as a GeNW or SiNW, can cause asymmetric band bending in the semiconductor. Such device will produce a photo current when light is incident upon it. We used the amplitude modulation (AM) type KPFM which suffers from low spatial accuracy due to a surface averaging effect [121], so KPFM of a metal-NW-metal device was not successful in getting nanowire band structure information.

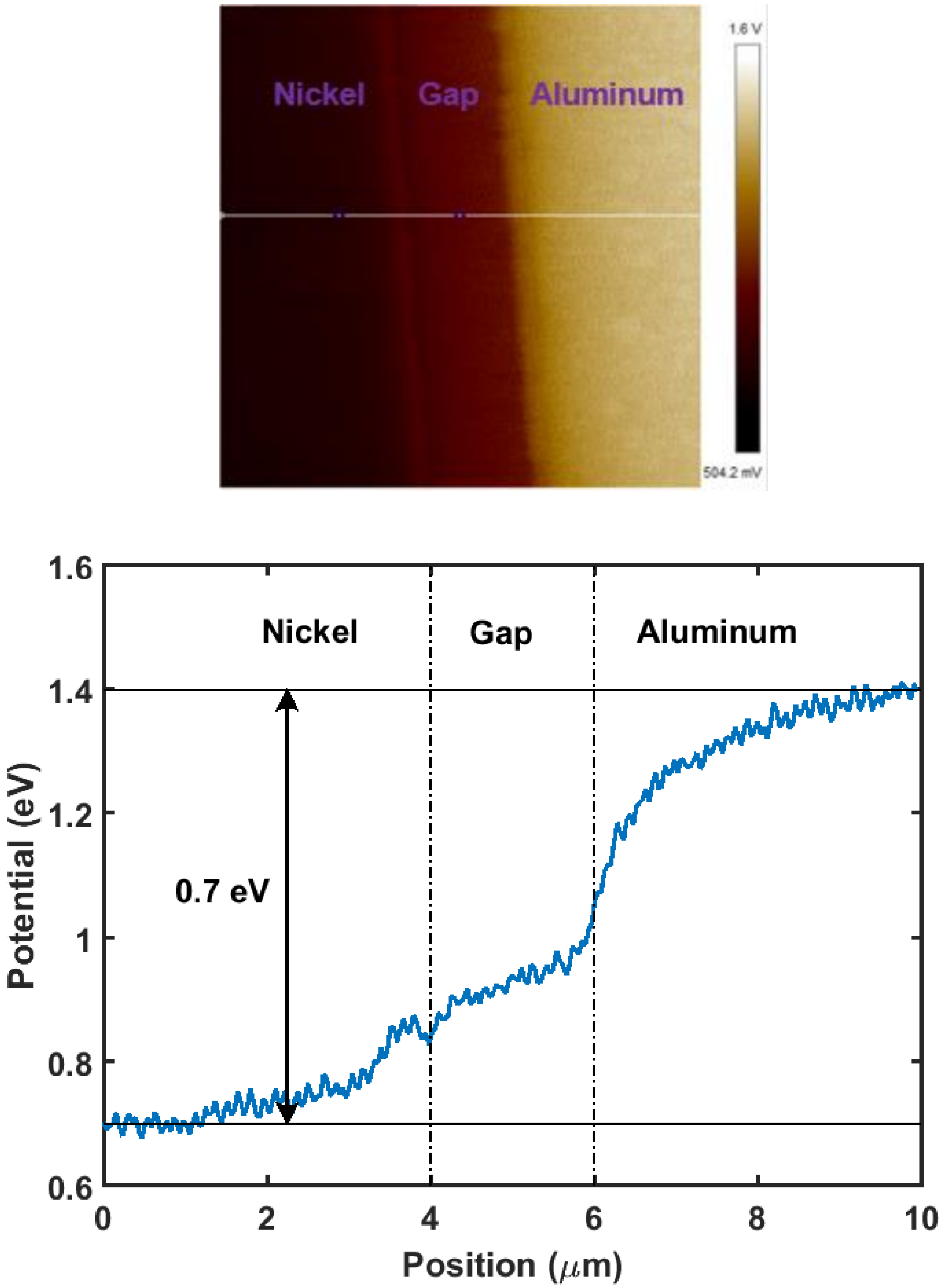

Figure 4.6. (a) KPFM scan of a two metal (Nickel and Aluminum) device without nanowire (b) shows the surface work function along the horizontal line in (a).

4.3.4 *Discussions*

To present some plausible explanations for the measured electrical characteristics, we take a bottom-up approach and consider the energy band diagrams for two different but simple current channels, shown in Figure 4.7. In the first case, shown in Figure 4.7(a), there is only a single NW between the two dissimilar work-function metals. The work function difference might induce band banding[101], but the exact degree of band bending will depend on the NW, the two metals and the two NW-metal contacts. Such bending can separate the photo-generated electrons and holes and generate a photocurrent. The amount of the current will also depend on the characteristics of the NW, the metal and the NW-metal contacts.

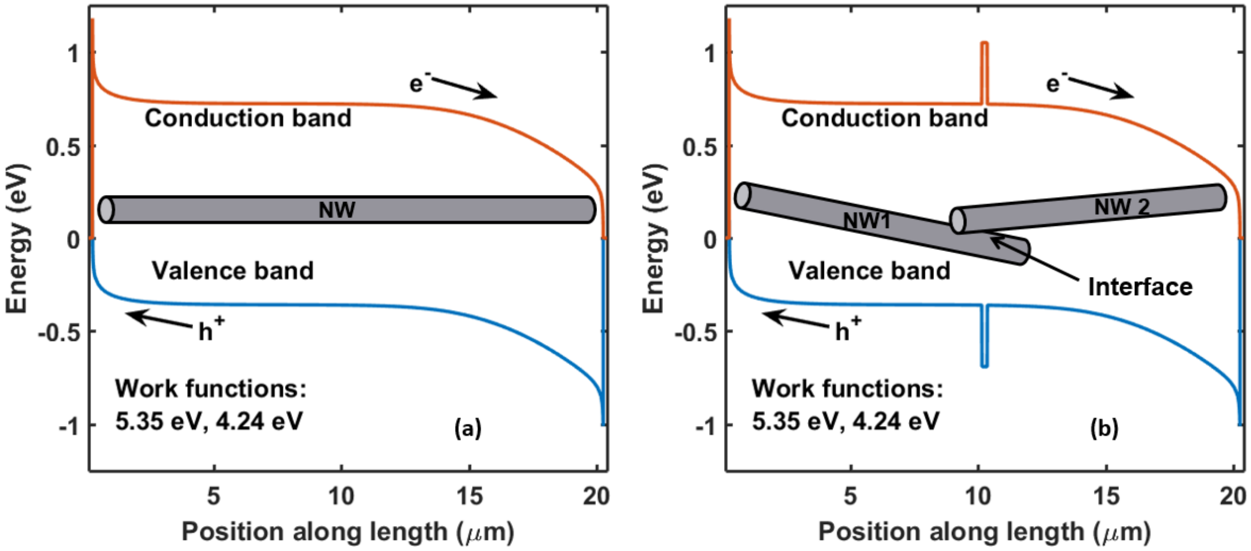

Figure 4.7. Energy band diagrams of current path for a single NW (a), and multiple NWs (b).

Figure 4.7(b) depicts the second case, in which a single current channel has two NWs instead of one. In addition to factors in the first case, *i.e.*, the NW, the metals and the NW-metal contacts, the NW-NW interface will have some effect on channel conductivity. The barriers at the middle of the energy bands represent non-ideal NW-NW interface due to presence of a nonconductive shell or native oxide at the NW surface or a surface depletion layer. Such a barrier can make the NW-NW interface the dominating factor and significantly reduce the channel conductivity. Obviously as the number of NWs involved in a single current channel increases, the number of NW-NW interfaces also increases and the current decrease might become more severe.

Depending on length and network density, dispersed NWs can be found in various possible orientations, and their conduction can be dominated by single or multiple NW channels.

(i) If the NWs are sufficiently long and sparse, they can contact bothelectrodes directly, as shown in Figure 4.8(a). Therefore, the sparse newtork will effectively consist of many single-NW channels, such as the one in Figure 4.7(a) and lead to enhanced carrier conduction and greater current.

(ii) The shorter NWs (i.e., shorter than the metal-to-metal gap) cannot individually contact both electrodes, and they can only interlink to bridge the electrode gap and form a device (cf. electrical percolation), as seen in Figure 4.8(b). In this case, the current channels are similar to the one in Figure 4.7(b). The carrier transport will be limited by the large NW-to-NW juction resistance due to the presence of a non-conducting shell or native oxide at the NW surface[116], [122]. Thus, the higher the density of NWs, the better the interlink[119], [123], and the larger the current.

(iii) Irrespective of the length size, if the density of the NW network is higher than what is required for a one-NW-layer thick surface coverage, many NWs at the top might not contact either electrode. Rather, they will be in contact with the underlying NWs, which might be in direct contact with at least one of the electrodes (Al or Ni), as seen in Figure 4.8(c). Additionally most of the bottom NWs are likely in contact with only electrode at one end, while the other end of the NW is surrounded by other NWs, instead of contacting the other electrode. This scenario will again lead to current paths similar to the one in Figure 4.7(b). But, unlike case (ii), the current channels will involve more and more NWs as the network density increases, and the current will decrease due to increasingly inefficient NW-NW transport.

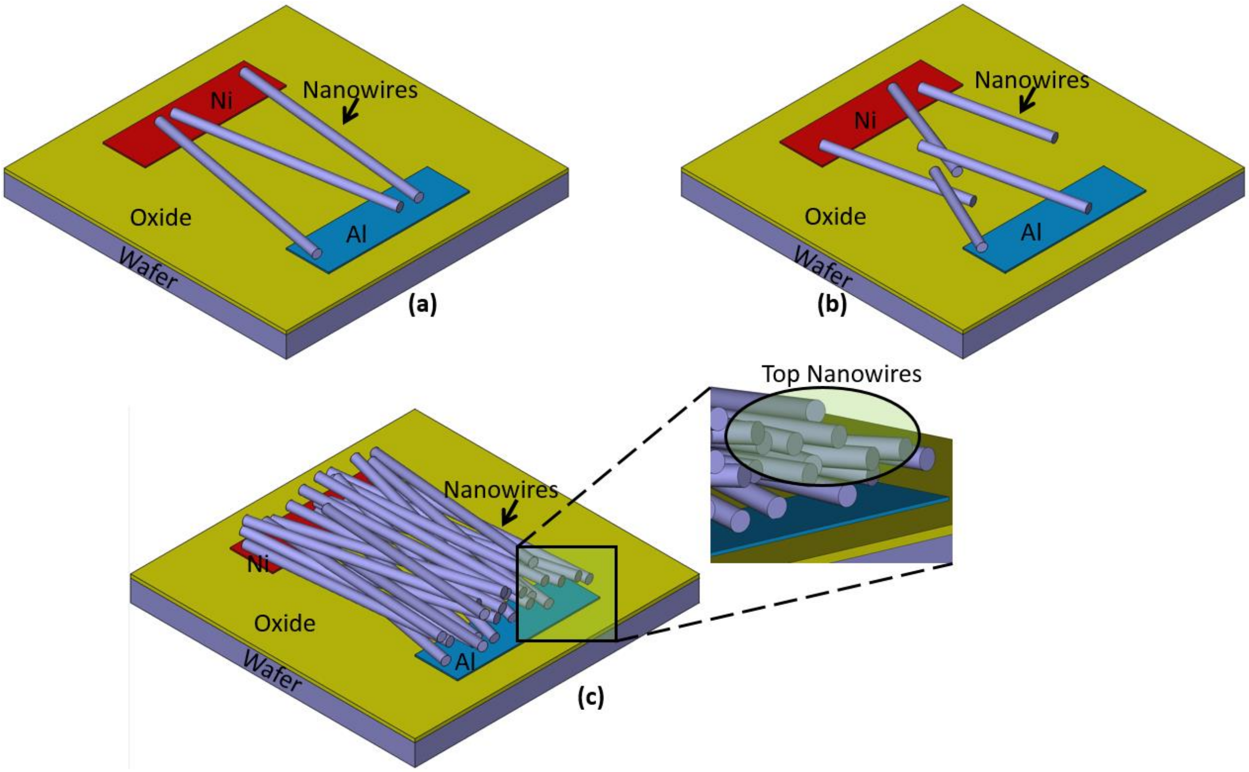

Figure 4.8. RDNW device schematics. (a) long sparse NW network (inset shows band structure of a Ni-NW-Al channel), (b) short, sparse NW network (inset shows band structure of a Ni-NW1-Oxide-NW2-Al channel), (c) long, dense NW network, inset shows zoom in on one end of some of the top NWs.

Therefore, in the dark, the sparse (and sufficientlylong) NWs produce more current due to better contact with the metal electrodes. When illuminated, the sparse NWs absorb photons directly and transport carriers effectively, thereby exhibiting higher photocurrents. However, in the denser NWs, the network is thick and most of the incident light is absorbed by the top NWs[124]. The photogenerated carriers inside these NWs need to be transported through other NWs to the electrode, and therefore, the NW-NW junction resistance limits the current flow, leading to smaller current values in dense NW devices. This phenomenon is a result of inefficient nanoscale transport.

4.4 CONCLUSIONS

In summary, Ge- and SiNW-based low-cost randomly dispersed networks were fabricated and their potential for self-powered photo-switching has been demonstrated. These devices can efficiently trap and absorb the incident light and collect the photo generated excitons, as evidenced by photocurrent measurements. Larger currents can be extracted from GeNWs than from SiNWs. GeNW devices exhibit better photo-switching because of greater conductivity and inter-NW transport. KPFM measurement suggests that contact work function difference of 0.7 eV is achievable with Ni and Al. The ‘anomalous’ increase in current as the density of the randomly dispersed NW networks decreases, when the electrode gap is comparable to the NW lengths, is a general phenomenon of the devices tested and has been clearly explained. The consistency of the results indicates that this anomaly is applicable to nanoscale devices with electrodes of either similar or dissimilar work function and that there is an optimum number of dispersed NWs for obtaining the best optoelectronic response

Chapter 5. STUDY OF NARROW AND BENT SILICON NANOWIRES

Bent narrow silicon nanowires are studied using molecular dynamics and quantum mechanical simulations. Details of nanowire bending process, electronic Hamiltonian generation, and electronic transport calculation are covered. Local strain or strain in the atomic scale in nanowires are analyzed, and electronic transport as well as the energy gap in the transport as a function of bending strain and nanowire diameter is calculated. In addition, the simulation process is repeated for the same nanowires but with uniaxial strain instead of bending. Comparison shows that for the same nanowire and for the same amount of average strain, the decrease in energy gap in electronic transmission is larger in the case of bending. This shows that, for the same range of strain variation, a bent nanowire will absorb a wider spectrum of light than a uniaxially strained nanowire.

5.1 INTRODUCTION

Silicon nanowires have huge potential in micro- and nano-technology. They can be fabricated in both top-down and bottom-up approaches, and have been employed in electronic devices (e.g. nanotransistors [60], [61], [125], solar cells [1], [3], [11]), optoelectronic devices [126], sensors [62], [63], [127], [128], as well as thermoelectric energy conversions [129], [130]. They have also been fabricated in a range of diameters; from a few nanometers to a few hundred nanometers. The sub-10nm diameter nanowires are particularly interesting, as unlike the bulk silicon and the wider wires, they have been predicted to have a direct bandgap [28]–[30]. They are, thus, appropriate for optoelectronic studies. More interestingly, the bandgap of the narrow silicon nanowires can be changed through application of mechanical strain [30], [131]. It has also been shown that by applying strain the direct bandgap of a narrow silicon nanowire can be turned into indirect, and vice versa [28], [30]. As we know, direct bandgap semiconductor absorbs / emits light more efficiently than indirect bandgap semiconductor. This means mechanical strain is important in modulating both electronic and optoelectronic properties of narrow silicon nanowires.

Strain has traditionally been applied to planar MOSFETs to enhance their mobility [43]. The usual approach to straining such devices is through lattice mismatch and stress-memorization [132]–[134] techniques. For nanowires though, mechanical bending of the substrate containing the nanowires [44], [45] or deposition of extra layer of straining materials [135], such oxide and nitride, on a portion of the wire surface are common.

Simulation of different device phenomena is an integral part of research and development. It is more important for nanodevices as most of the traditional theory is inadequate, and the experimental studies are costly. Simulation and modeling help understand experiments, and can also help devise new tests. Electronic simulations of nanodevices under strain has been done mostly in the density functional theory (DFT) formalism [131], [136], which is the best approach available. But DFT suffers from high computational demand. Because of this, almost all the atomic level electronic property studies have been done only for uniaxial strain. To the best of our knowledge, there has been no simulation works of bent silicon nanowires to study the effect of bending strain on electronic properties. The reason might be that, due to the bent nature of the nanowire, there is no crystal symmetry present. Without such a symmetry, the predominantly used periodic boundary condition is not applicable along the length of the nanowire. So, as a considerably long length of the bent nanowire needs to be studied, the computational demand is huge.

For such large structures, classical molecular mechanics or dynamics (MD) study may be the required compromise. It is atomistic so that atomic interactions will be accurately captured. But it is also classical so that quantum effects will not be properly taken into account. More importantly, its computational demand is less than that of DFT. Classical MD is extensively used in the study of mechanical [137], [138] and thermal [139], [140] properties of many micro [141] and nanodevices [142], [143], including silicon nanowires [140], [144]. Guenole et al. [145] used MD to study the effect of temperature and surface states on plasticity in silicon nanowires, while Yang et al. [146] studied the effects of the shape on the yield stresses of silicon nanowires. Cai et al. [147] simulated nanowire size, and temperature effects, on its fracture mechanisms. Thermal properties of silicon nanowires are crucial to the integration of nanowires in MEMS and NEMS systems [148]–[150]. Silicon nanowire thermal conductivity was studied by non-equilibrium molecular dynamics (NEMD) simulations in [151], while Aluru et al. [152] studied the size and surface orientation effects on the thermal expansion coefficients. MD has been also used in the study of properties of silicon nanoparticles [153], [154]. In reference [155], Andriotis et al. studied electrical conductivity of tetrahedral and clathrate (or cagelike) nanowires. In many of these simulations, MD and energy minimization have been used to extend, compress, or bend the nanowires, and to extract information about their mechanical and thermal properties. But few have studied the electronic properties [155] to a great detail, especially for the bent nanowires.

Although the studies of strain dependent electronic property of nanowires have exclusively focused on uniaxial strain, real nanowires have some inherent bending present in them. They can also be bent easily. Bottom up synthesized nanowires are usually not perfectly straight, rather they are twisted as well as jumbled [31], [32]. In reference [33], Bertagnolli grew wires with a predefined rectangular shape. Zhu et al. [34] demonstrated over 40% bending strain in nanowires with tungsten tip. They could also make the bending permanent with low electron beam exposure. In an ultimate bending strengths experiment, Cook et al. [35] bent silicon nanowires lying on a flat substrate through sequential atomic force microscope (AFM) tip manipulations. They could achieve a U-shape bending, and found that, as nanowire diameter decreased, the bending strength increased. This means that very narrow nanowires, in addition to having quantum mechanical properties, are stable even under large stress. Although these bending studies have been done mostly on bottom up nanowires, even top-down fabricated nanowires can be bent intentionally [36], [37] or unintentionally [38], [39]. Nannini et al. [38] demonstrated bending in released silicon nanowires due to surface relaxation, and noticed that, an applied force can modify the mechanical equilibrium. Moreover, top down and bottom up approaches can be combined [40] to get horizontally suspended, well-oriented and size-controlled nanowire arrays. These new bending approaches may open up new possibilities, and thus, electronic study of bent wires is necessary. It is also informative to compare bent nanowires with uniaxially strained nanowires to get an idea about their relative merits.

5.2 DESCRIPTION

This section presents detailed description about shape and size of the simulated nanowires, the simulation approaches, and the bending as well as uniaxial straining method. Definition of strain under the bent condition, the passivation approach as well as the electronic Hamiltonian generation procedure are also discussed. Moreover, formalism for calculating electronic transmission of the nanowire is briefly described.

5.2.1 *Nanowire size and shape*

Silicon nanowires with six different cross sectional areas are studied in this work. All the nanowires are <110> directed, since experimentally it has been found that the smallest nanowires grow mainly along the <110> direction [32], [156]–[160]. The average diameters of the nanowires are 1.0 nm, 1.7 nm, 2.3 nm, 3.1 nm, 3.6 nm and 4.3 nm, which are labeled here as <110>2d, <110>3d, <110>4d, <110>5d, <110>6d and <110>7d, respectively. The left side of Figure 5.1(a) shows the hexagonal cross section of nanowire <110>3d; other nanowires have similar shape, but they have either narrower or wider diameters. The right side of Figure 5.1(a) shows the assumed co-ordinate system. The top of Figure 5.1(b) shows the full length of the nanowire in Figure 5.1(a) while the bottom again shows the co-ordinate system. The total length of each nanowire is 19.922 nm, and there are 103 atomic layers along the length. Figure 5.1 (c) show three consecutive layers. The starting nanowire structures were generated by the repetition of DFT optimized, unit cell sized silicon nanowires studied in [30].

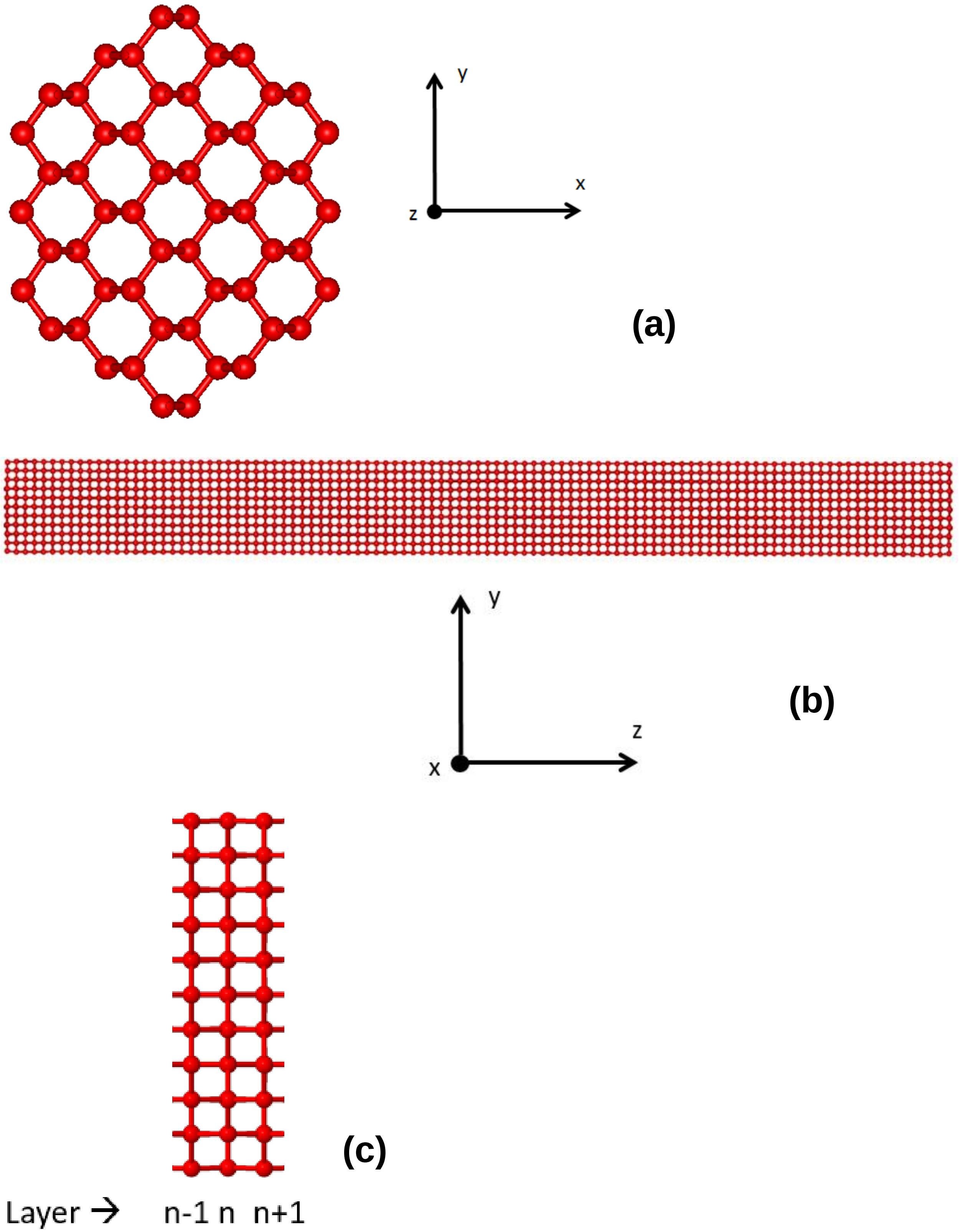

Figure 5.1. Nanowire cross section (a), length (b), a few layers along length (c).

5.2.2 *Molecular dynamics*

The molecular dynamics simulation is done with the Large-scale Atomic/Molecular Massively Parallel Simulator (LAMMPS) [161]. The Tersoff [162], [163] many-body bond-order reactive potential is used to describe the Si-Si interatomic interactions. Tersoff potential has been used in the theoretical study of atomic structure and mechanical properties of branched silicon nanowires [164], in the investigation of atomic elastic stiffness in silicon [165], and in the study of mechanical properties of silicon nanowire under uniaxial tension and compression [166]. In reference [167], Tersoff potential was used to study the effects of vacancy defects on thermal conduction of silicon nanowires. It has also been concluded, from the prediction of bulk silicon thermal conductivity, that Tersoff potential gives the best results for isotopically pure silicon [168]. Reference [169] concluded that Tersoff potential reasonably reproduced small defect clusters predicted by the more comprehensive tight-binding or first-principles calculations. It should be noted here that during our mechanical straining (bending as well as uniaxial strain) of the nanowires, hydrogen passivation of nanowire surfaces was not included as potential for Si-H bond is not available. In [167], it has been found that DFT calculations with or without hydrogen passivation gave almost the same thermal conductance.

5.2.3 *Procedure of applying bending and uniaxial strain*

The nanowire is strained using the following procedure. The nanowire structure is first optimized by using energy minimization, with no velocity or force restrictions on any atoms. Then, the atoms are subdivided into three groups: the leftmost 8 atomic layers form the left group, the rightmost 8 atomic layers form the right group, and the rest fall in the middle group. To apply bending strain to the middle group, first the atoms in the left (right) group are rotated counter clockwise

(clockwise) in the yz plane (Figure 5.1(b) top) by an angle of 0.05 degree. Then they are kept frozen while energy minimization is done to the middle group of atoms. Similar approach for bending nanowires was applied in mechanical study of silicon carbide nanowires [137]. After the minimization, the atomic positions of all the atoms are saved, and the process is repeated for the next increment of the rotation angle. To apply uniaxial strain to the middle group of atoms, instead of rotating, the atoms in the left (right) group are shifted to the left (right) by 0.005 nm. The rest of the minimization procedure is similar to bending.

5.2.4 *Strain definition*

For uniaxial strain, each atomic layer is under the same amount of strain, which is defined as

$$\varepsilon = \frac{L - L_0}{L_0}$$

where ε is the uniaxial strain, and L_0 and L, respectively, are the layer-to-layer distances before and after applying strain.

The strain profile along the length of a bent nanowire is nonlinear, that is, it changes from layer to layer. For the bending approach described above, usually the bottom surface is compressed while the top surface is under tensile strain. For purposes of calculation as well as for comparison with the uniaxial case, a simplified strain definition is used. First, the **average** xyz positions of each atomic layer, both before and after bending, are calculated. Then the strain between any two consecutive layers is given by,

$$\varepsilon = \frac{L - L_0}{L_0} \qquad (5.1)$$

where ε is the average strain, and L_0 and L, respectively, are the **average** layer-to-layer distances before and after the bending.

5.2.5 *Cropping off nanowire ends*

Since the left and right groups of atoms are kept fixed during the bending or uniaxial straining and energy minimization process, the atoms in the middle group, which are close to atoms in the edge groups, undergo some artificial deformations. To avoid such artificial deformation, the full length of the bent nanowire is not used in the electronic calculations. Specifically, 19 layers of atoms from each end (including those that are kept frozen during the minimization) are cropped off. Electronic simulation is done using the remaining 65 layers of atoms. The cropping also decreases the problem size making the NEGF calculation computationally a little less intensive. Even after this cropping, however, the length is considerably larger than what is usually used in electronic studies of nanowires under uniaxial strain.

5.2.6 *Surface passivation*

Next the nanowires after their ends cropped off are hydrogen passivated with the GaussView [170] software. Although hydrogen passivation was not done during the energy minimization, it is essential to do so before any electronic calculations. Otherwise, the dangling bonds at the unpassivated nanowire surface will show up as electronic states inside the bandgap and overshadow the true energy gap. In reference [30], D. Shiri et al. studied strain dependent electronic properties of hydrogen passivated silicon nanowires. B. Li et al. [171] used hydrogen passivated nanowires to study the effects of size and shape on surface lattice constants of silicon nanowires. Experimentally, in [172] hydrogen passivation was done to silicon nanowires before functionalization with organic substituents. S. Kim et al. [173] showed improvement in MOSFET performance by doing high pressure hydrogen annealing which reduced interface states at silicon nanowire and oxide interface. T. Tezukal et al. [174] found that annealing of top-down fabricated nanowires in hydrogen made the nanowire surface less rough.

5.2.7 *Electronic Hamiltonians and their sizes*

The mechanics simulation gives the atomic positions. After that, for electronic calculations, the position information has to be represented in the form of a Hamiltonian matrix. Here we use the $sp^3d^5s^*$ tight binding (TB) method with parameters from Jancu [175]. Because of non-uniform strain along the nanowire, Bloch's theorem cannot be used, and thus, the usual electronic band structure cannot be calculated. Instead, we calculate electronic transmission to find the energy gap in it. Two types of Hamiltonians are generated: (i) in-layer Hamiltonian, which represents all the atoms in a layer, and (ii) layer-to-layer Hamiltonian, which gives coupling between the atoms in consecutive layers. Depending on the diameter, each layer can have 12 to 147 silicon, and 8 to 28 hydrogen atoms. Without considering spin-orbit coupling in $sp^3d^5s^*$ TB, Hamiltonian size for each silicon atom is 10x10, and that for each hydrogen atom is 1x1. Thus, the Hamiltonian size of each layer is between 128x128 and 1498x1498. As already pointed out, we have a total of 65 layers. Thus, while the narrower nanowires pose less challenge in terms of processor and memory requirements, the wider ones are really computationally intensive.

5.2.8 *Calculation of electronic transmission*

The transmission through the nanowire is calculated using the Green's function [176] formalism, which is briefly described next. First, the retarded Green function, $\mathrm{G}^{\mathrm{r}}(\mathrm{E})$, of the nanowire as a function of energy E is calculated as

$$G^r(E) = \frac{1}{EI - H - \Sigma_L^r(E) - \Sigma_R^r(E)} \qquad (5.2)$$

where H represents the Hamiltonian of the nanowire, I is an identity matrix, $\sum_{L(R)}^{r}(E)$ is the self-energy of the left (right) contact. H is block tri-diagonal in nature due to both the layered structure of the device and the use of nearest-neighbor TB Hamiltonian. The contact self-energy represents the connection strength between the nanowire and the contact, and it can be rigorously calculated by first calculating the surface Green's function of the contact. But this calculation is very time consuming and a simpler approach works. We assume, for each contact, a broadening function, Γ, of the form

$$\Gamma_{L(R)}(E) = \mathrm{E}_0 I \qquad (5.3)$$

and then, calculate the self-energy as

$$\sum_{L(R)}^{r}(E) = -\frac{i}{2}\Gamma_{L(R)} \qquad (5.4)$$

where E_0 is a constant with unit of energy. We assume its value to be equal to 50 mEv. Once $\mathrm{G}^{\mathrm{r}}(\mathrm{E})$ has been calculated, the electronic transmission can be found from

$$T(E) = tr\left(\Gamma_L(E)G^r(E)\Gamma_R(E)G^a(E)\right) \qquad (5.5)$$

Here, $\mathrm{G}^{\mathrm{a}}(\mathrm{E})$ represents the advanced Green function of the nanowire, which is found form the transpose-conjugate of $\mathrm{G}^{\mathrm{r}}(\mathrm{E})$. *tr* here means the trace of the matrix.

5.3 RESULTS AND DISCUSSION

5.3.1 *Strain analysis*

In this subsection, we analyze the strains in the nanowires. An average representation for the axial strain, as given by Eqn. (5.1), is calculated for easy correlation with electronic properties and comparison with uniaxial strain results. Figure 5.2 shows three bent nanowires, (a) <110>3d, (b)

<110>5d, and (c) <110>7d, with their local atomic strain along the length (z) direction visualized as color variation. To obtain this strain configuration, the left and right atom groups of each nanowire was rotated by 15^{o} in the vertical (yz) plane (Figure 5.1(b)). The top side of each nanowire is under tension while the bottom side is under compression. The corner atoms are under the largest amount of strain due to rotation. Also for a fixed amount of rotation, as expected, the range of strain variation (from most compressive to most tensile) increases with the nanowire diameter. In addition, the largest tensile strain magnitude is always higher than the largest compressive strain magnitude, for example, +3.7% vs -2.3% for nanowire <110>3d. This is due to the atomic potentials resisting compression more than tension because as the atoms are brought closer to each other beyond the no-strain minimum energy position the energy increases exponentially.

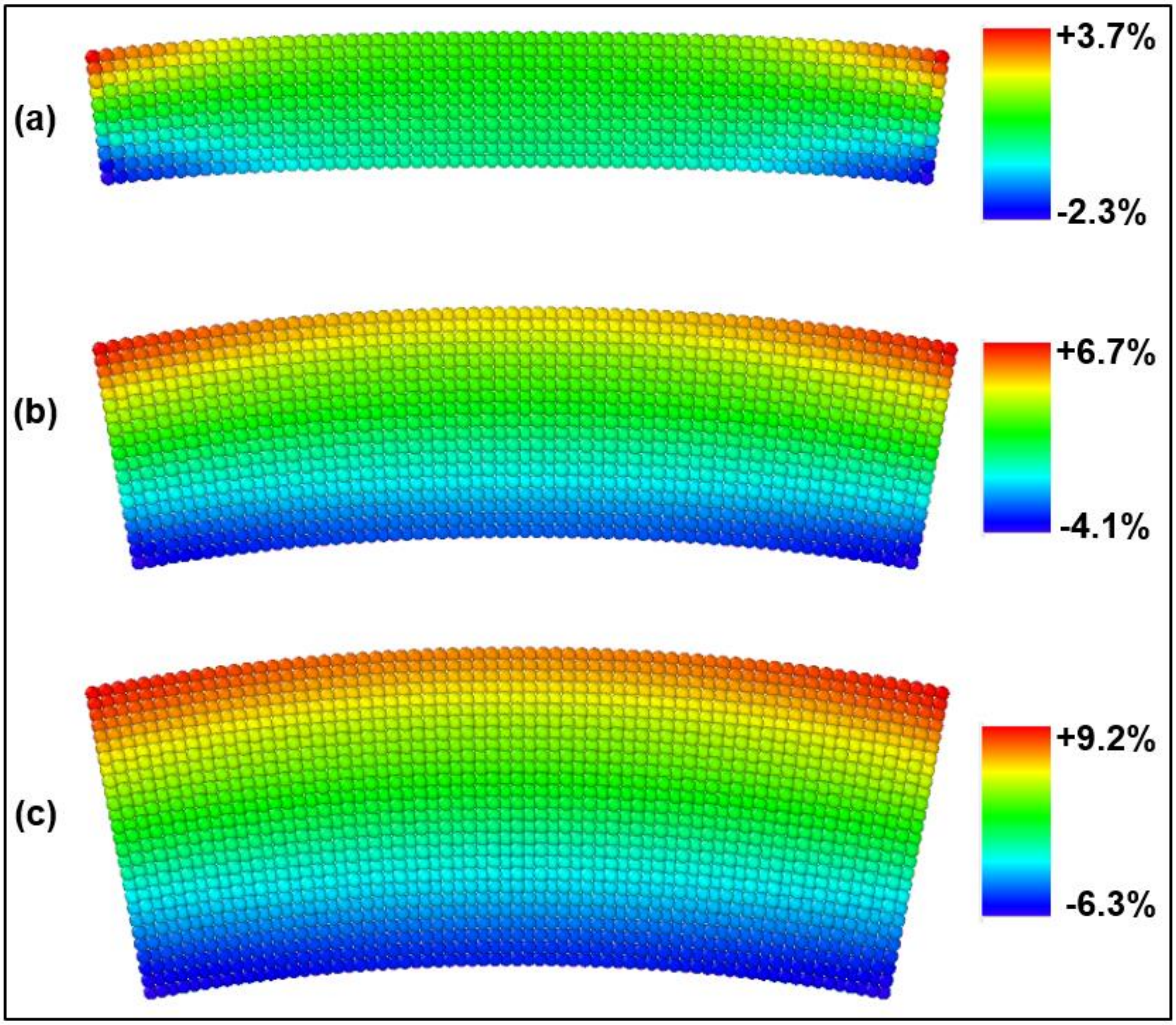

Figure 5.2. Local strain along the **z-direction** (length) in 3 different nanowires as a color plot; (a) <110>3d, (b) <110>5d, (c) <110>7d.

Figure 5.3 shows the local strain along x-direction while Figure 5.4 shows y-direction atomic strain for the nanowires (a) <110>3d, (b) <110>5d, and (c) <110>7d. For both cases, top surface is under compression while bottom surface is under tension, which is opposite to what we saw for z-direction. So the atoms that are under tension along the length compresses in the cross-sectional plane. Note as y-dimension is slightly larger than x, the range of y-strain is also larger.

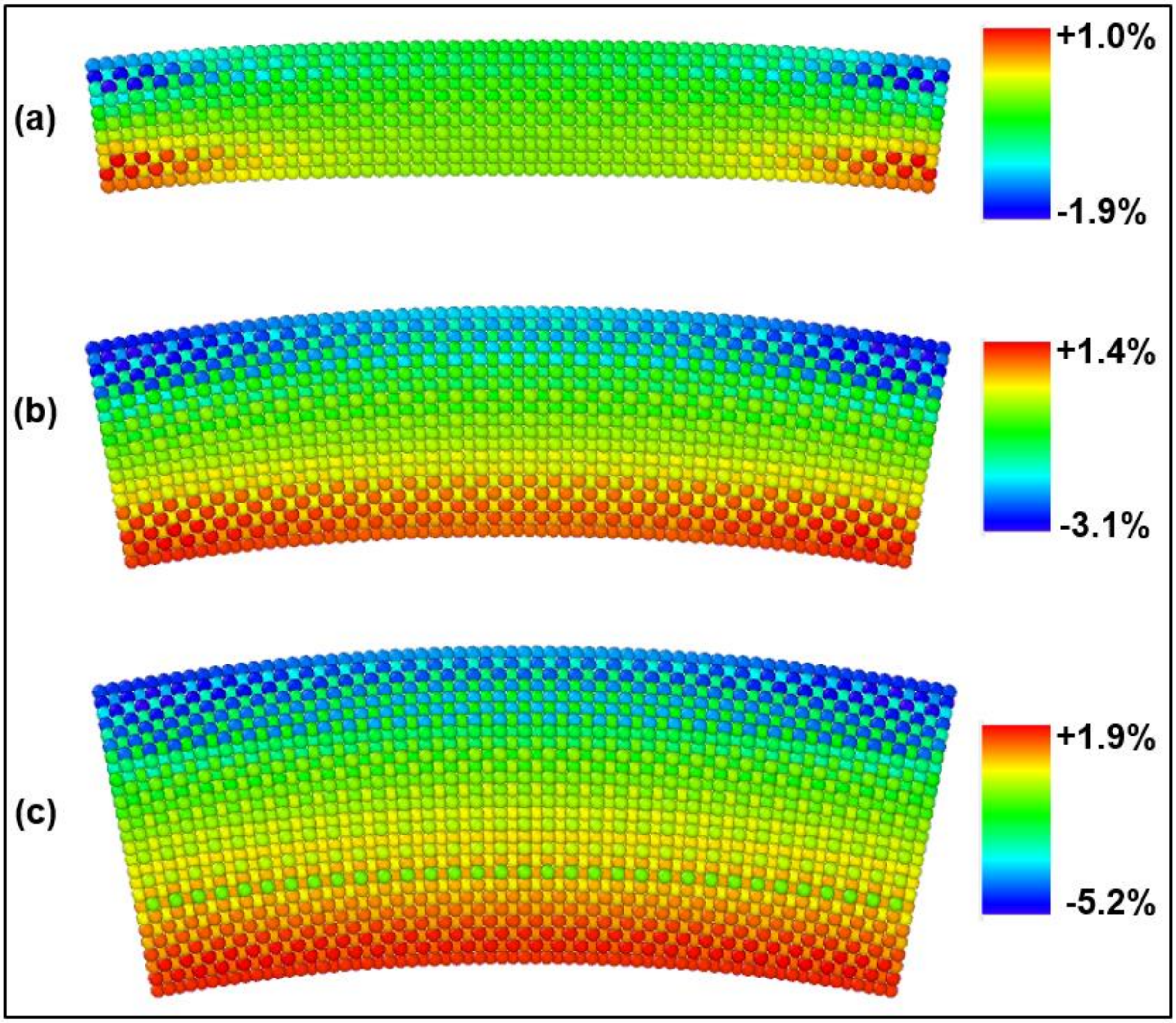

Figure 5.3. Local strain along the **x-direction** in 3 different nanowires as a color plot; (a) <110>3d, (b) <110>5d, (c) <110>7d.

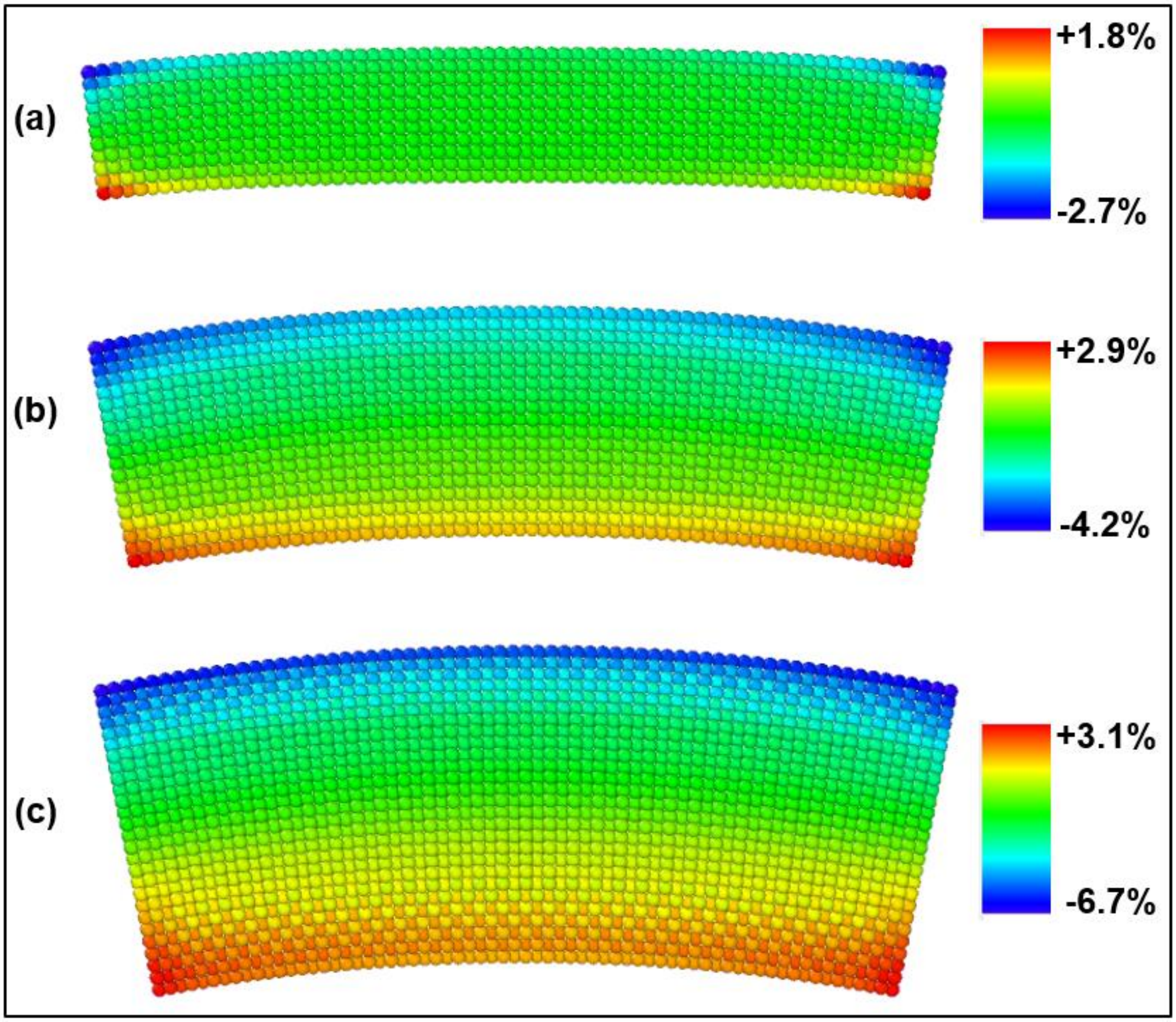

Figure 5.4. Local strain along the **y-direction** in 3 different nanowires as a color plot; (a) <110>3d, (b) <110>5d, (c) <110>7d.

We next consider local strain in uniaxially strained nanowires. Figure 5.5 shows the strain along (a) z (length) direction, (b) x direction and (c) y direction uniaxially strained <110>5d nanowire. As expected, variation in strain along the length is small and the atoms are always under tension. Such variation is due to fixing the end atoms and allowing the middle atoms to relax. Strain along x and y directions are always compressive and again the range is larger along y since the y dimension of the nanowire is also larger that x dimension.

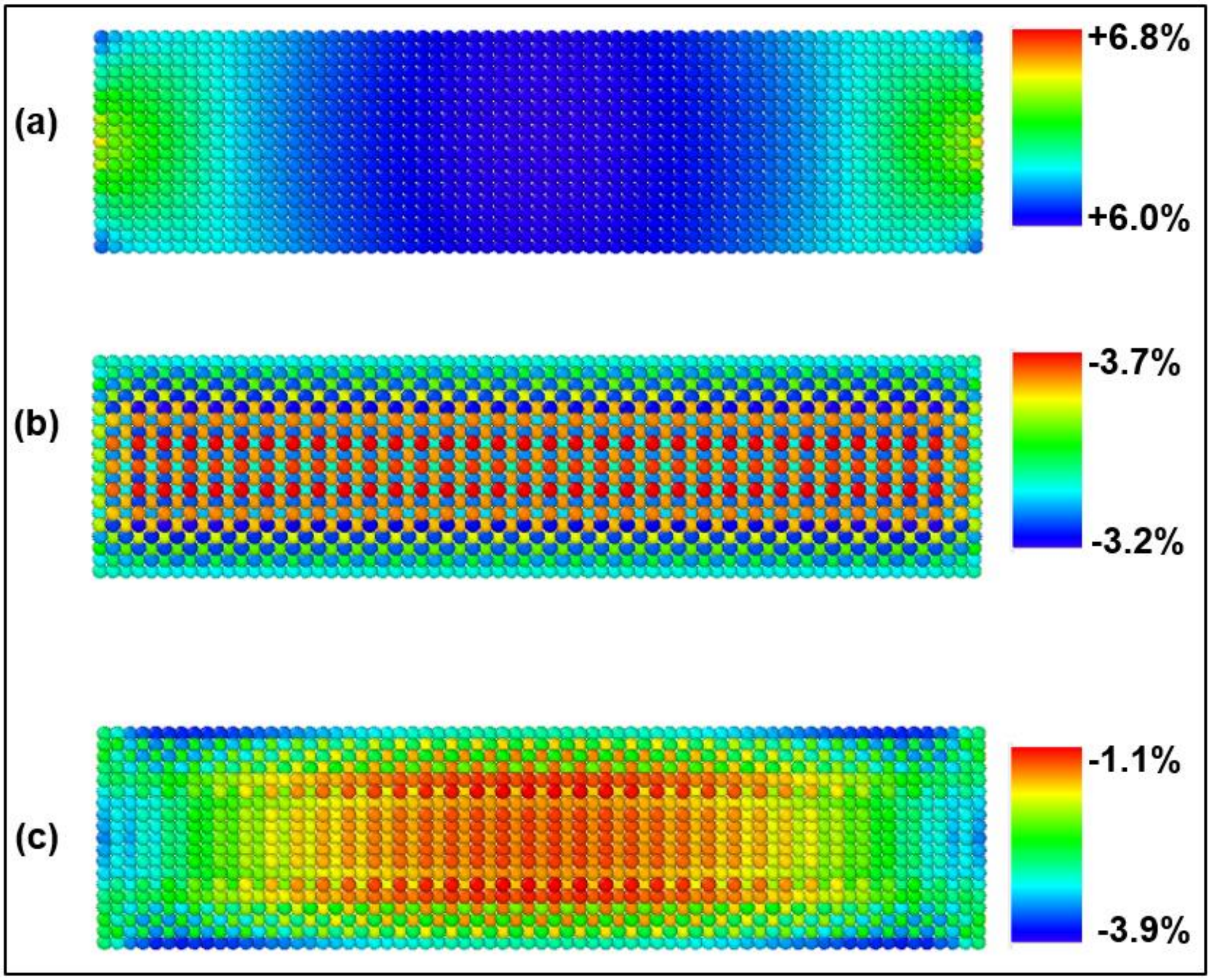

Figure 5.5. Local strain along (a) z, (b) x, (c) y direction as a color plot for a uniaxially strained <110>5d nanowire.

Next our goal is to get an average representation of the strain along the length in the bent nanowires. Figure 5.6 plots all the three strain ranges (x-range (a), y-range (b), and z-range (c)) as functions of the nanowire diameter for different amount of end atom group rotations. The ranges are almost linearly proportion to the nanowire diameter. As already seen, the y-range values are slightly higher than the x-range values as diameter along y is wider. Due to bending along the length, z-range values are the largest.

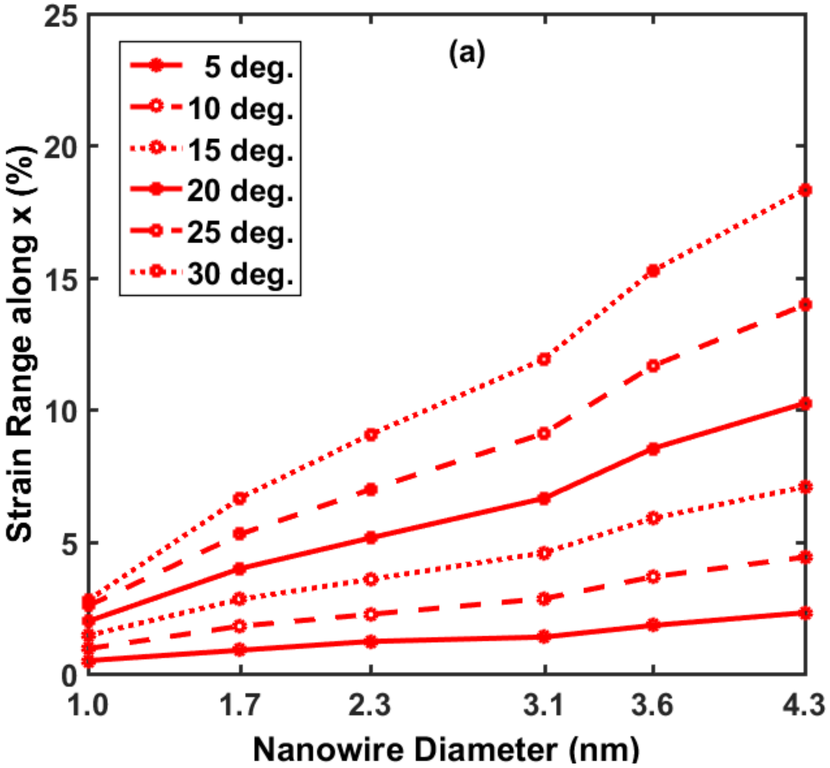
(a)
5 deg.
10 deg.
15 deg.
20 deg.
25 deg.
30 deg.
Strain Range along x (%)
0
5
10
15
20
25
1.0
1.7
2.3
3.1
3.6
4.3
Nanowire Diameter (nm)

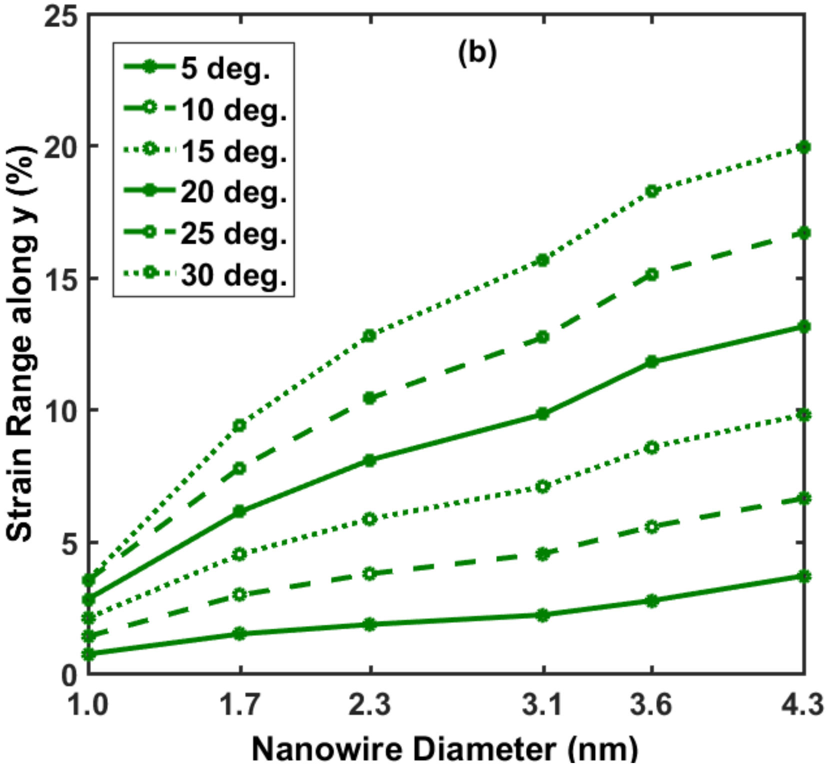
(b)
5 deg.
10 deg.
15 deg.
20 deg.
25 deg.
30 deg.
Strain Range along y (%)
0
5
10
15
20
25
1.0
1.7
2.3
3.1
3.6
4.3
Nanowire Diameter (nm)

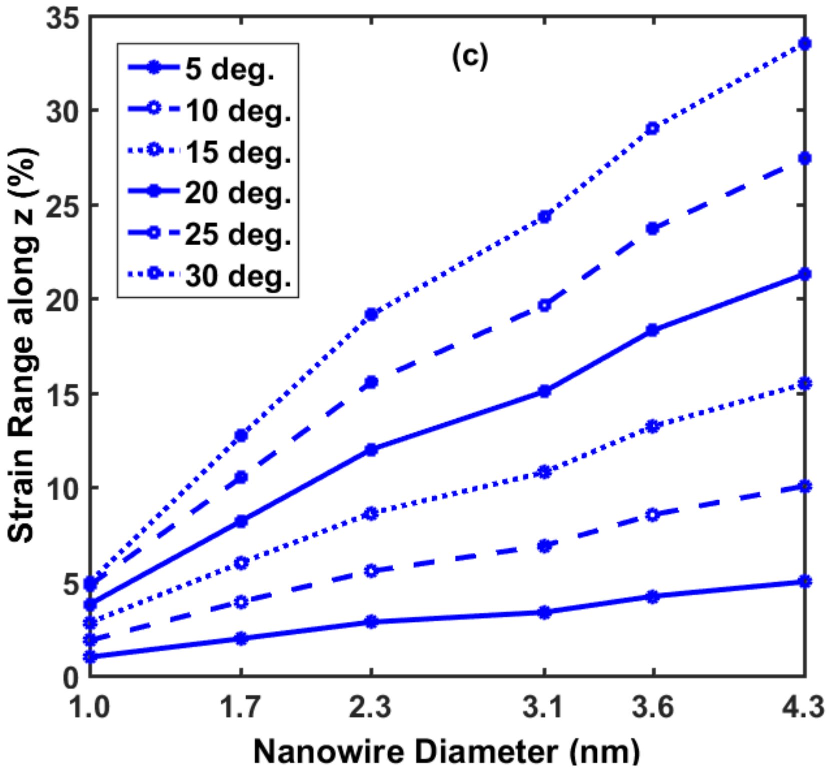

Figure 5.6. Ranges of strain (x-range (a), y-range, (b) and z-range (c)) as functions of nanowire diameter for different amount of end atom group rotations.

The strain plots in Figures 5.2, 5.3, 5.4 and 5.6 give an insight into strain profile of bent nanowires, it is difficult to correlate them directly with the any electronic properties. For example, it is not possible, for a specific nanowire under a specific amount of rotation, to show a one-to-one relation between the strain value and electronic transmission as strain does not have single value. Note that just the amount of rotation is not a good measure, especially if we want to make a comparison with uniaxially strained nanowires. So some average strain value at each strain configuration (or end atom rotation) is more convenient for such correlation. But any kind of averaging will lose some information, and more importantly, such simplifications should be justifiable. With such a goal in mind, we turn to the layer to layer strain of the nanowire.

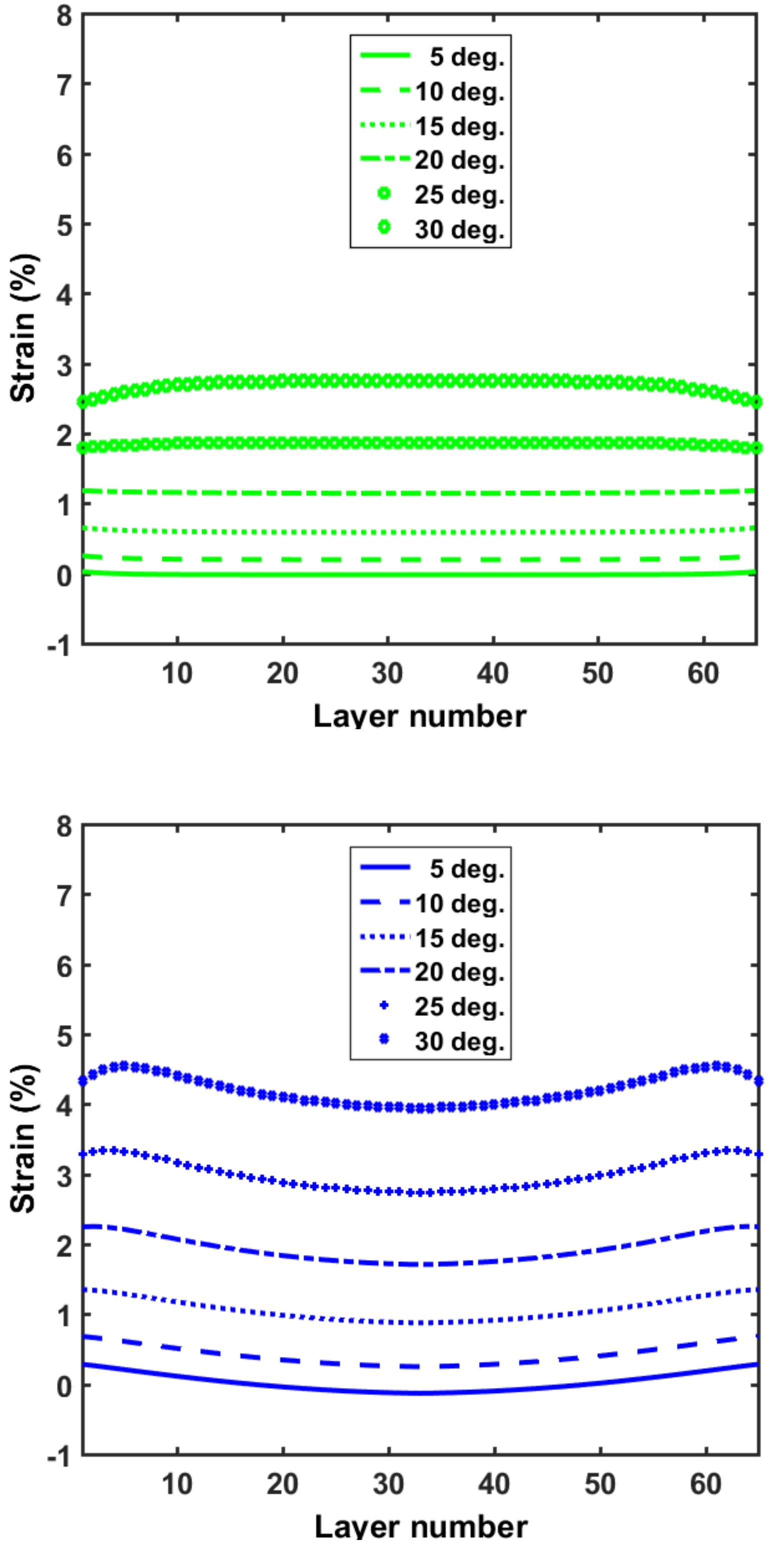

Figure 5.7. Layer to layer average strain along length. (a) <110>3d, and (b) <110>6d.

Figure 5.7 plots the layer to layer strain along the length, as defined in equation (5.1), for two different nanowires - (a) <110>3d and (b) <110>6d. We have already seen in Figure 5.6 (c) that the range of variation of strain over all the atoms in a nanowire can be quite large, mainly because of the corner atoms. However, the layer to layer strain variation is actually smaller (Figure 5.7). Thus, it is possible to find a single quantity, representing an equivalent average strain, for each of the curves in Figure 5.7. This average number is plotted in Figure 5.8 for all the bent nanowires considered in this study. For the same end atom rotation, like the strain ranges, the average strain also increases linearly with the diameter. The average strain value is used for studying correlation with electronic properties and uniaxially strained nanowires, for which nominal strain value along length is used.

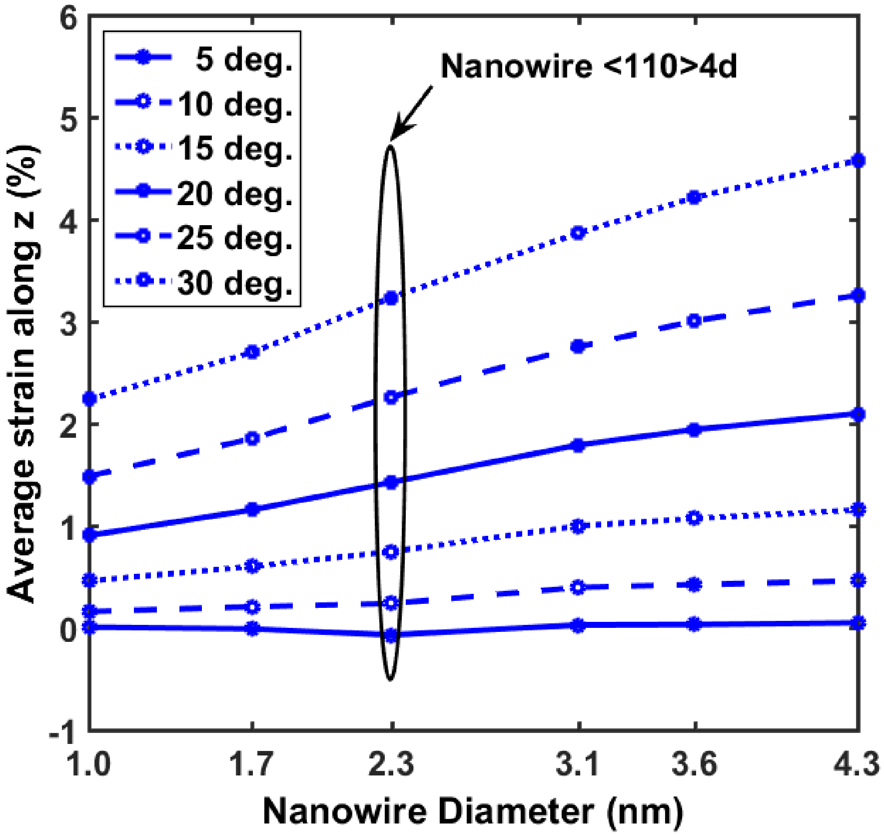

Figure 5.8. Average strain along length of a bent nanowire as a function of diameter.

5.3.2 *Electronic transmission*

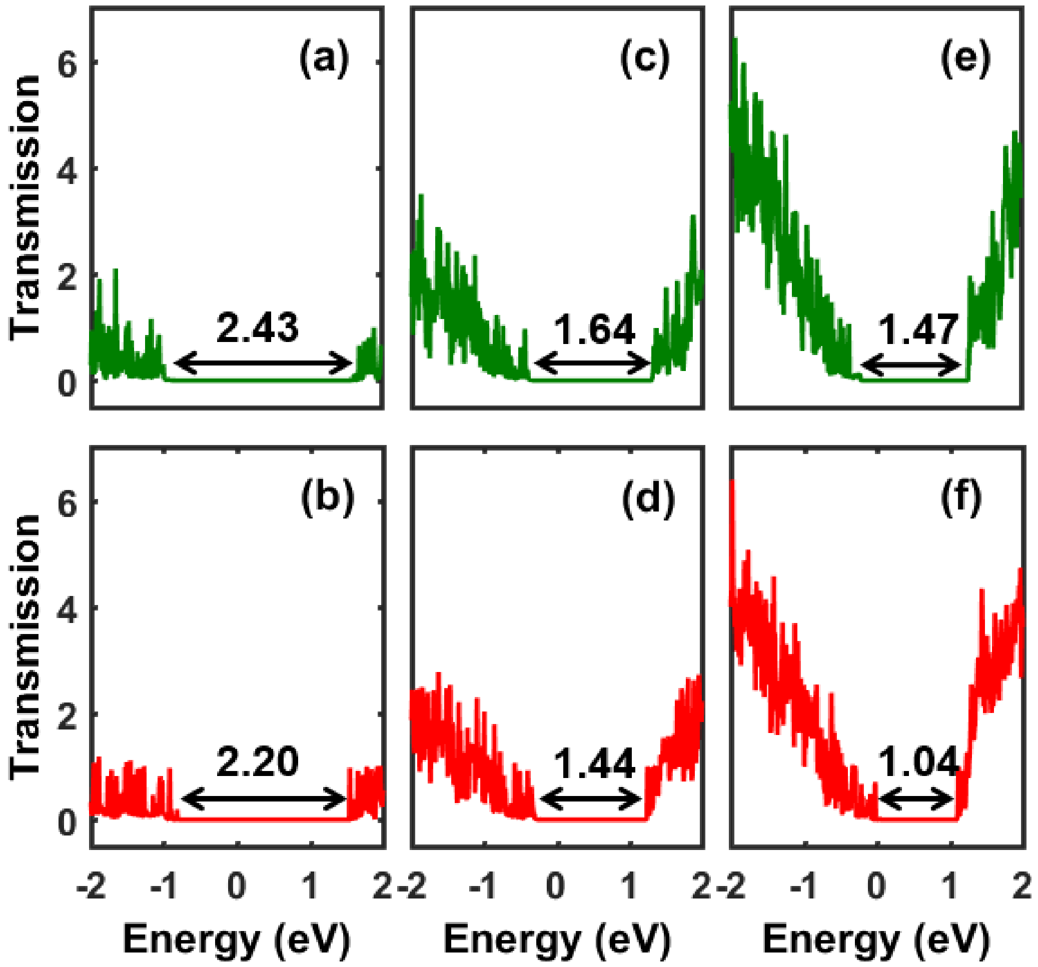

Figure 5.9. Electronic transmission as a function of energy. (a) <110>2d with no rotation, (b) <110>2d with 15-degree rotation, (c) <110>4d with no rotation, (d) <110>4d with 15-degree rotation, (e) <110>6d with no rotation, (f) <110>6d with 15-degree rotation.

In bent nanowires, the bending strain compresses or extends the nanowire locally (Figures 5.2, 5.3 and 5.4), although on an average, the nanowire is under tensile strain along the length (Figure 5.8). The strain (bending or uniaxial) changes the electronic band profile of the nanowire. As already discussed, due to absence of any crystal symmetry under bending, it is not possible, however, to calculate the energy band diagram using the Bloch's theorem. We rather calculate the electronic transmission (Eq. (5.5)) in the strained nanowires as a function of energy.

Figure 5.9 plots the electronic transmission as a function of energy for, respectively, zero and 15-degree end atom group rotations in the nanowires: (a, b) <110>2d, (c, d) <110>4d, (e, f) <110>6d. We notice at least three important trends in the plots. First, a narrower nanowire has a lower transmission value. A narrower nanowire has a fewer number of electronic modes, and at any energy, transmission is proportional to the number of modes. So this is reasonable. Second, the transmission gap - the continuous energy range over which the transmission is zero - in the nanowire is larger than the bulk silicon bandgap. The transmission gap also decreases as the nanowire diameter increases. This is expected since, in the limit of a very wide wire approaching the bulk material, the energy gap in the wire should approach that in the bulk. Also it is to be noticed that gaps in the unstrained nanowires - 2.43 eV (Figure 5.9(a)), 1.64 eV (Figure 5.9(c)), and 1.47 eV (Figure 5.6(e)) - are consistent with both DFT [30] and DFTB [29] calculations. This validates use of molecular dynamics for structure minimization. Third and most importantly, the gap in each nanowire decreases as the amount of bending strain (that is, average strain along length) increases. This behavior is also consistent with the results in [30], which predicts that for an increase in uniaxial tensile strain in the nanowire, its bandgap decreases.

We can get a more comprehensive overview by studying the transmission energy gap as a function of the nanowire diameter with the angle of end atom group rotation as a parameter. Such characteristics are plotted in Figure 5.10 for no rotation and six different rotations (5, 10, 15, 20, 25, and 30 degree) conditions. We note that, the larger the nanowire diameter, the smaller the transmission gap, which we already saw in Figure 5.9. For low bending strain (top curves), as the nanowire diameter decreases from the largest diameter, 4.3 nm, the gap increases gradually. This increase, however, becomes sharper as the diameter decreases below 1.7 nm. For large bending strain (bottom curves), the gap increases rapidly in an almost linear fashion as the diameter decreases. It is interesting to note that for the two widest wires, diameters 3.6 nm and 4.3 nm, the gap completely disappears for larger strains. The reason for the disappearance of the gap is as follows. We have seen, in Figure 5.6, that the strain range is higher for the wider wires. This means, for large rotations, the local strains (both tensile and compression) in some parts of the wider wires are very high (and of opposite direction). These large local strains represent a huge departure from the perfect crystal structure and introduce many electronic modes in the band gap, thereby making the gap totally disappear.

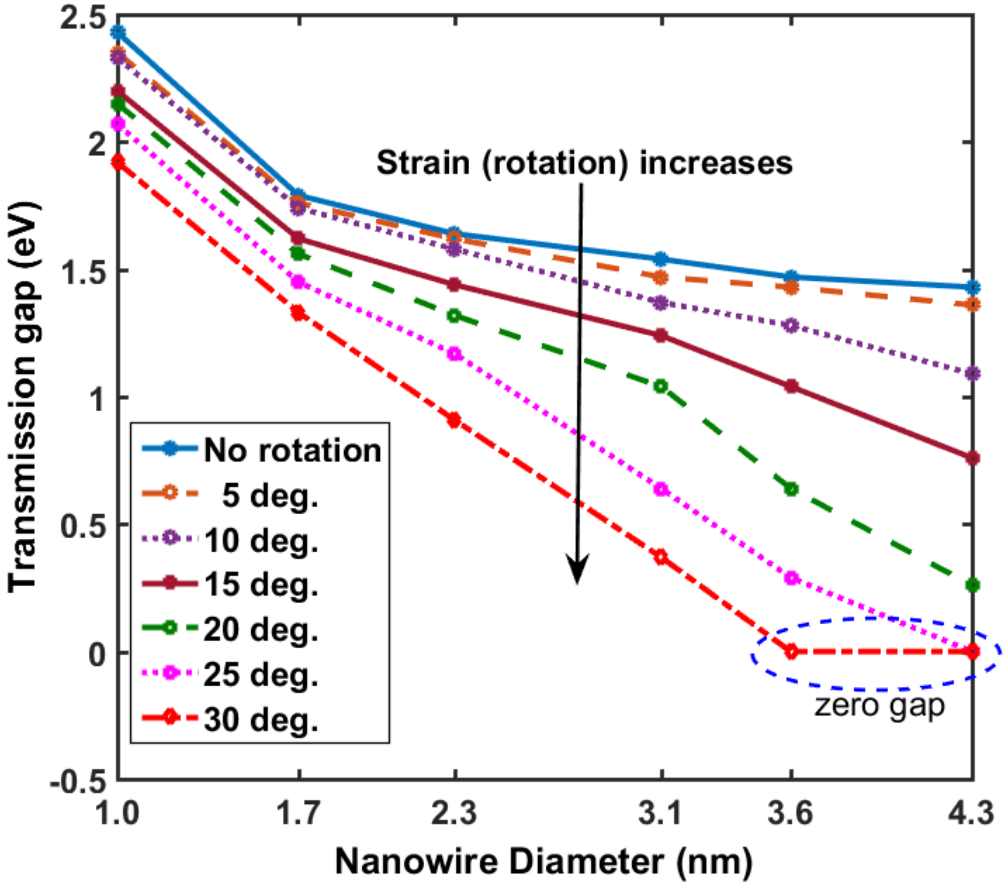

Figure 5.10. Transmission gap as a function of nanowire diameter for different rotation angles.

5.3.3 *Bent nanowire vs. uniaxially strained nanowire*

Figure 5.11 plots the energy gap in electronic transmission as a function of percentage strain for six nanowires for both bent and uniaxially strained cases. Nanowire diameter increases as we go from the top of the plot towards the bottom. The gap decreases linearly with the strain for both method of straining. However, for the same diameter and the same average strain, the gap is smaller and its decrease rate is faster in bent nanowire. Such trends have important consequences. Smaller gap means the bent nanowires will have higher conductivity. The larger decrease rate also means that the strain modulated band gap will respond to electromagnetic wave (light) of a wider wavelength range. This clearly is an advantage of the bent nanowire over the uniaxially strained nanowire.

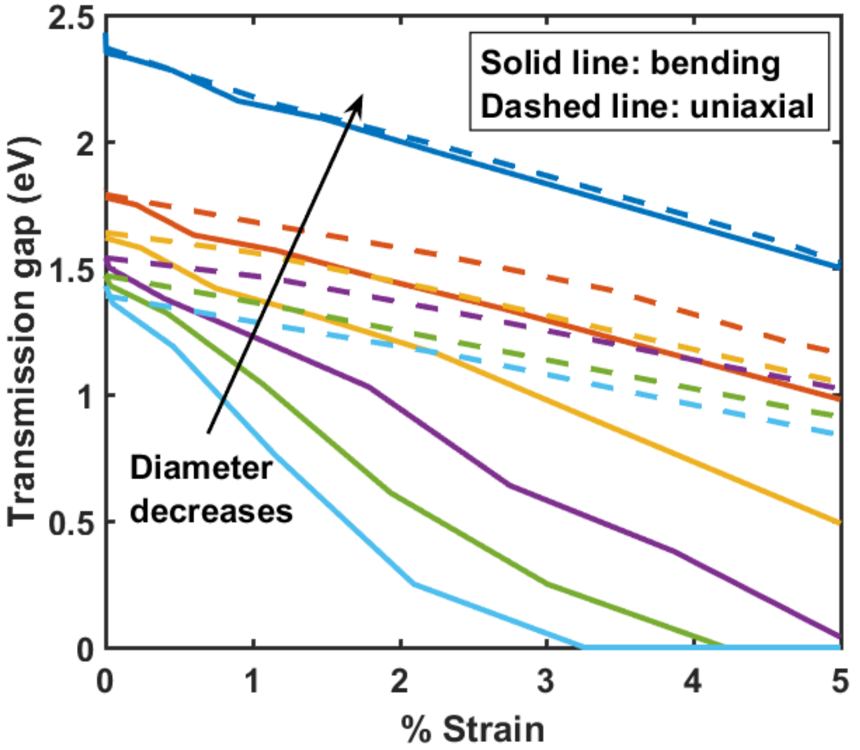

Figure 5.11. Transmission gap as a function of % strain. Solid: bent, dashed: uniaxial.

Change in both conduction band minimum (Ec) and valence band maximum (Ev) can contribute to the change in the gap. So it is informative to know which one contributes more. Figure 5.12 plots both Ec and Ev for the cases in Figure 5.11. For narrow nanowires, both Ec and Ev change at a similar rate, but as nanowire diameter increases, the Ev change becomes larger and larger.

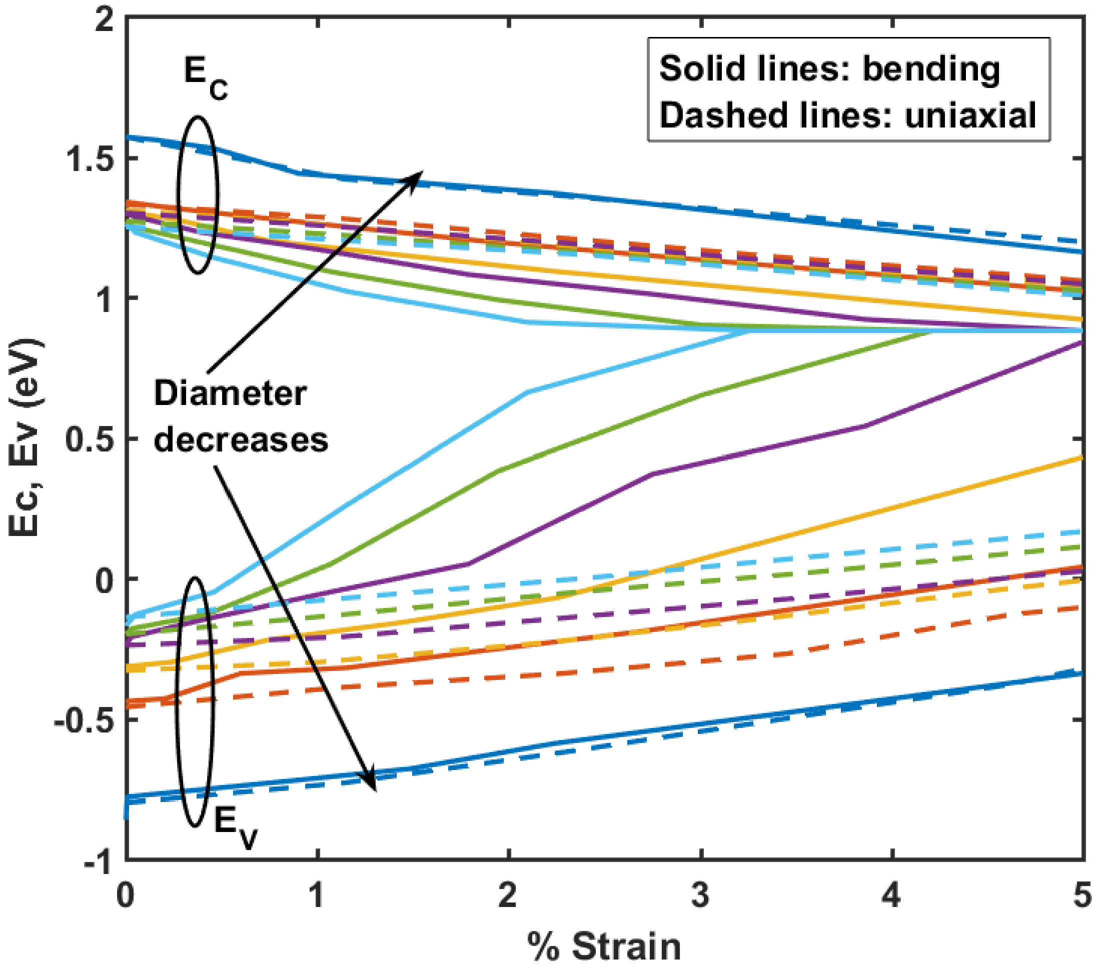

Figure 5.12. Ec and EV as a function of % strain. Solid: bent, dashed: uniaxial.

5.4 CONCLUSION

Atomic strain analysis and electronic transport calculation were done for six different nanowires of varying diameters. Both bending strain and uniaxial strain have been considered. The whole simulation process was described in detail. For the same amount of end atom rotation, the wider the nanowire, the larger is the strain. This directly translates into smaller energy gaps in electronic transmission for wider wires. Comparison of bent and uniaxially strained nanowire of same diameter reveals that for same average strain the bent nanowire has a smaller gap in transmission. The gap decrease rate is also found to be faster in the bent case. This makes bent nanowires superior over uniaxially strained nanowires in terms of conductivity as well as strain modulated photo absorption a wider wavelength range.

Chapter 6. SUMMARY AND FUTURE WORKS

This thesis explored modeling, fabrication and characterization of contact asymmetry (in size and work function) effect on photoresponse of bulk silicon and nanowires of both silicon and germanium semiconductors. It also investigated strain dependent electronic transport modulation of narrow silicon nanowires. The main contributions of this work are summarized below:

1) In Chapter 2, we presented the theory of contact size asymmetry based photosensor. If one contact has a larger area than the other, then under uniform illumination, the device is asymmetric and produce large photocurrent at zero applied bias. Even for symmetric contact devices asymmetry is possible if the light spot size is smaller than contact to contact distance and the light is at an asymmetric point with respect to the contacts. The theory was tested with prototype devices fabricated using a single metal deposition process. Hundreds of zero bias photocurrent was achieved and the response was fast and stable. Device simulation was also carried out to further understand the underlying physics of such devices. It was found that contact surface recombination and Schottky effects are essential for matching trends in experimental I-V characteristics.
2) Chapter 3 discussed detailed modeling of single silicon wire solar cells. Symmetric area contact with large work function difference (> 1 eV) can achieve performance of p-n junction type solar cells without the need for controlled high doping in nanowire devices. It was shown that due to recombination of photo generated minority carriers with majority carriers, the short circuit current as well as open circuit voltage saturates as nanowire length increases. The saturation length was found to be approximately five times the diffusion length. With one contact metal

work function above and the second contact metal work function below the nanowire work function, the first contact is Schottky while the other is Ohmic. The Schottky metal work function has a large impact on both I_{SC} and V_{OC} than the Ohmic contact.

Due to saturation, the current density performance of long nanowires worse than short nanowires. We presented multiple contact design to boost the short circuit current performance of the long wires without affecting the open circuit voltage. We further studied grounded gate design for improving both I_{SC} and V_{OC}. Such design also generates negative differential resistance effect in a non-resonant tunneling device.

3) In Chapter 4, we described fabrication and characterization of nanowire network based photo sensing devices with dual work function metal contacts. A process for fabricating nanowire network with controlled density was developed. Our characterization showed that the network produces appreciable photo response and demonstrated, for the first time for visual wavelength, zero bias photo response in nanowire network devices.

For devices with contact to contact distance larger than the nanowire length, the higher the nanowire density the larger the current. However, for devices with metal to metal distance shorter than nanowire length, sparser devices gave larger current than that given by a considerably denser device. This behavior was explained by considering the nanowire to nanowire transport phenomenon as our nanowires had some less-conducting shell surrounding them. The shell act as a bottleneck in the overall transport from one contact to the other. We also did KPFM measurements to show that our contact metal pair achieved a work function difference of about 0.7 eV which generates the required asymmetry for large zero bias photocurrent.

4) Simulation work of strained narrow silicon nanowires with an emphasis on bent nanowires was detailed in Chapter 5. The complete simulation methodology was described and local (atomic) strain was analyzed as function of nanowire diameter, direction as well as straining method (bending or uniaxial straining). Local strain in bent nanowires varied widely in magnitude and direction (tensile vs compressive). For comparison with uniaxial case, average strain along the length was defined and it was found that as a function of diameter the average strain increased linearly for same amount of end atom rotation used to cause bending. Electronic transmission vs energy plot shows that the energy gap decreases as diameter increases. For the same nanowire, the gap again decreases as the strain increases. Comparison with uniaxially strained nanowires reveal that the decrease rate is faster in bent nanowire for similar strain along the length. For nanowires with diameters 3.6 nm and 4.3 nm, less than 5% strain is required to reduce the gap to zero and cause a semiconductor to metal transition. Such transition is difficult, if not impossible, to achieve in uniaxially strained nanowires due to the slow rate of gap decrease with increase in strain. Since in bent nanowires, the range of strain over all the atoms in a nanowire is large, achieving larger gap decrease rate seems easier.

Below we briefly describe ways of extending this work:

1) The asymmetric contact area bulk silicon photosensor device work can be extended by fabricating and characterizing devices with ranges of contact size, contact to

contact distance, and metals with a range of work functions. Our prototype devices proved the theory and modeling indicated that surface recombination and barrier lowering are important. But for finding the best device, the elaborate fabrication and comparison with commercially available devices will be useful.

2) We did detailed modeling of single nanowire solar cell (or photo sensor) devices of two or more contacts in Chapter 3. Top-down fabrication with SOI wafers can be done to make such devices and characterize their performance against simulation result. We studied nanowire network based photo sensor devices in Chapter 4. Our KPFM measurement showed that our chosen metals Al and Ni had a work function difference of about 0.7 eV. However, due to instrument limitation, we did not do KPFM measurement on single nanowire devices. So fabrication of single nanowire devices and doing KPFM to extract the complete KPFM profile from first metal to nanowire to second contact would give valuable information about the band structure of the device.

Energy gap measurement in narrow bent silicon nanowires can be done to complement our simulation work of bent (as well as uniaxially strained) nanowires. Strain dependent photo absorption / emission measurements can be done for such purposes.

BIBLIOGRAPHY

[1] L. Tsakalakos, J. Balch, J. Fronheiser, B. a. Korevaar, O. Sulima, and J. Rand, "Silicon nanowire solar cells," *Appl. Phys. Lett.*, vol. 91, no. 23, p. 233117, 2007.

[2] V. Sivakov, G. Andrä, A. Gawlik, A. Berger, J. Plentz, F. Falk, and S. H. Christiansen, "Silicon Nanowire-Based Solar Cells on Glass : Synthesis , Optical Properties , and Cell Parameters," *Nano Lett.*, vol. 9, no. 4, pp. 1549–1554, 2009.

[3] E. Garnett and P. Yang, "Light trapping in silicon nanowire solar cells," *Nano Lett.*, vol. 10, no. 3, pp. 1082–1087, Mar. 2010.

[4] J. Li, H. Yu, S. M. Wong, X. Li, G. Zhang, P. G.-Q. Lo, and D.-L. Kwong, "Design guidelines of periodic Si nanowire arrays for solar cell application," *Appl. Phys. Lett.*, vol. 95, no. 24, p. 243113, 2009.

[5] C. Lin and M. L. Povinelli, "Optical absorption enhancement in silicon nanowire arrays with a large lattice constant for photovoltaic applications.," *Opt. Express*, vol. 17, no. 22, pp. 19371–81, Oct. 2009.

[6] M. M. Adachi, A. J. Labelle, S. M. Thon, X. Lan, S. Hoogland, and E. H. Sargent, "Broadband solar absorption enhancement via periodic nanostructuring of electrodes," *Sci. Rep.*, vol. 3, p. 2928, Jan. 2013.

[7] C. Yang, C. J. Barrelet, F. Capasso, and C. M. Lieber, "Single p-type/intrinsic/n-type silicon nanowires as nanoscale avalanche photodetectors.," *Nano Lett.*, vol. 6, no. 12, pp. 2929–34, Dec. 2006.

[8] P. Servati, a. Colli, S. Hofmann, Y. Q. Fu, P. Beecher, Z. a. K. Durrani, a. C. Ferrari, a. J. Flewitt, J. Robertson, and W. I. Milne, "Scalable silicon nanowire photodetectors," *Phys. E Low-dimensional Syst. Nanostructures*, vol. 38, no. 1–2, pp. 64–66, Apr. 2007.

[9] C. B. Winkelmann, I. Ionica, X. Chevalier, G. Royal, C. Bucher, and V. Bouchiat, "Optical switching of porphyrin-coated silicon nanowire field effect transistors.," *Nano Lett.*, vol. 7, no. 6, pp. 1454–8, Jun. 2007.

[10] J. Bae, H. Kim, X.-M. Zhang, C. H. Dang, Y. Zhang, Y. J. Choi, A. Nurmikko, and Z. L. Wang, "Si nanowire metal-insulator-semiconductor photodetectors as efficient light harvesters.," *Nanotechnology*, vol. 21, no. 9, p. 095502, Mar. 2010.

[11] M. M. Adachi, M. P. Anantram, and K. S. Karim, "Core-shell silicon nanowire solar cells," *Sci. Rep.*, vol. 3, p. 1546, Jan. 2013.

[12] M. G. Nikolaides, S. Rauschenbach, S. Luber, K. Buchholz, M. Tornow, G. Abstreiter, and A. R. Bausch, "Silicon-on insulator based thin-film resistor for chemical and biological sensor applications.," *Chemphyschem*, vol. 4, no. 10, pp. 1104–6, Oct. 2003.

[13] C. Yu, Q. Hao, S. Saha, L. Shi, X. Kong, and Z. L. Wang, "Integration of metal oxide nanobelts with microsystems for nerve agent detection," *Appl. Phys. Lett.*, vol. 86, no. 6, p. 063101, Jan. 2005.

[14] Z. Li, B. Rajendran, T. I. Kamins, X. Li, Y. Chen, and R. S. Williams, "Silicon nanowires for sequence-specific DNA sensing: device fabrication and simulation," *Appl. Phys. A*, vol. 80, no. 6, pp. 1257–1263, Mar. 2005.

[15] A. Tibuzzi, B. Margesin, M. Decarli, C. DiNatale, M. Zen, A. D'Amico, and G. Soncini, "MOS-Junction-Based Nanostructures by Thermal Oxidation of Silicon Wires for Hydrogen Detection," *IEEE Trans. Nanotechnol.*, vol. 3, no. 2, pp. 287–292, Jun. 2004.

[16] D. Zhang, Z. Liu, C. Li, T. Tang, X. Liu, S. Han, B. Lei, and C. Zhou, "Detection of NO 2 down to ppb Levels Using Individual and Multiple In 2 O 3 Nanowire Devices," *Nano*

Lett., vol. 4, no. 10, pp. 1919–1924, Oct. 2004.

[17] J. M. Lee and W. Lee, "Effects of Surface Roughness on Hydrogen Gas Sensing Properties of Single Pd Nanowires." American Scientific Publishers.

[18] F. Wang, S. Yip, N. Han, K. Fok, H. Lin, J. J. Hou, G. Dong, T. Hung, K. S. Chan, and J. C. Ho, "Surface roughness induced electron mobility degradation in InAs nanowires.," *Nanotechnology*, vol. 24, no. 37, p. 375202, Sep. 2013.

[19] L. J. Lauhon, M. S. Gudiksen, D. Wang, and C. M. Lieber, "Epitaxial core-shell and core-multishell nanowire heterostructures.," *Nature*, vol. 420, no. 6911, pp. 57–61, Nov. 2002.

[20] Y. Dong, B. Tian, T. J. Kempa, and C. M. Lieber, "Coaxial group III-nitride nanowire photovoltaics," *Nano Lett.*, vol. 9, no. 5, pp. 2183–7, May 2009.

[21] B. M. Kayes, H. a. Atwater, and N. S. Lewis, "Comparison of the device physics principles of planar and radial p-n junction nanorod solar cells," *J. Appl. Phys.*, vol. 97, no. 11, p. 114302, 2005.

[22] W. Shockley and H. J. Queisser, "Detailed Balance Limit of Efficiency of p-n Junction Solar Cells," *J. Appl. Phys.*, vol. 32, no. 3, p. 510, 1961.

[23] E. C. Garnett and P. Yang, "Silicon nanowire radial p-n junction solar cells," *J. Am. Chem. Soc.*, vol. 130, no. 29, pp. 9224–5, Jul. 2008.

[24] P. Peercy, "The drive to miniaturization," *Nature*, vol. 406, no. 6799, pp. 1023–1026, Aug. 2000.

[25] C. Claeys, "Technological Challenges of Advanced CMOS Processing and Their Impact on Design Aspects," *Proc. 17th Int. Conf. VLSI Des.*, p. 275, 2004.

[26] S. Xiong and J. Bokor, "Structural Optimization of SUTBDG Devices for Low-Power Applications," *IEEE Trans. Electron Devices*, vol. 52, no. 3, pp. 360–366, Mar. 2005.

[27] E. C. Jones and E. Ishida, "Shallow junction doping technologies for ULSI," *Mater. Sci. Eng. R Reports*, vol. 24, no. 1–2, pp. 1–80, 1998.

[28] X. B. Yang and R. Q. Zhang, "Indirect-to-direct band gap transitions in phosphorus adsorbed ⟨112⟩ silicon nanowires," *Appl. Phys. Lett.*, vol. 93, no. 17, p. 173108, 2008.

[29] M. Nolan, S. O'Callaghan, G. Fagas, J. C. Greer, and T. Frauenheim, "Silicon nanowire band gap modification.," *Nano Lett.*, vol. 7, no. 1, pp. 34–8, Jan. 2007.

[30] D. Shiri, Y. Kong, A. Buin, and M. P. Anantram, "Strain induced change of bandgap and effective mass in silicon nanowires," *Appl. Phys. Lett.*, vol. 93, no. 7, p. 073114, 2008.

[31] S. Hofmann, C. Ducati, R. J. Neill, S. Piscanec, a. C. Ferrari, J. Geng, R. E. Dunin-Borkowski, and J. Robertson, "Gold catalyzed growth of silicon nanowires by plasma enhanced chemical vapor deposition," *J. Appl. Phys.*, vol. 94, no. 9, p. 6005, 2003.

[32] Y. Cui, L. J. Lauhon, M. S. Gudiksen, J. Wang, and C. M. Lieber, "Diameter-controlled synthesis of single-crystal silicon nanowires," *Appl. Phys. Lett.*, vol. 78, no. 15, p. 2214, 2001.

[33] W. Molnar, a Lugstein, P. Pongratz, M. Seyring, M. Rettenmayr, C. Borschel, C. Ronning, N. Auner, C. Bauch, and E. Bertagnolli, "A general approach toward shape-controlled synthesis of silicon nanowires.," *Nano Lett.*, vol. 13, no. 1, pp. 21–5, Jan. 2013.

[34] S. Dai, J. Zhao, L. Xie, Y. Cai, N. Wang, and J. Zhu, "Electron-beam-induced elastic-plastic transition in Si nanowires," *Nano Lett.*, vol. 12, no. 5, pp. 2379–85, May 2012.

[35] G. Stan, S. Krylyuk, a V Davydov, I. Levin, and R. F. Cook, "Ultimate bending strength of Si nanowires.," *Nano Lett.*, vol. 12, no. 5, pp. 2599–604, May 2012.

[36] S. Zhang, L. Lou, and C. Lee, "Piezoresistive silicon nanowire based nanoelectromechanical system cantilever air flow sensor," *Appl. Phys. Lett.*, vol. 100, no.

2, p. 023111, 2012.

[37] R. Yang, T. He, C. Marcoux, P. Andreucci, L. Duraffourg, P. X. Feng, E. Engineering, C. Western, M. Campus, and G. Cedex, “SILICON NANOWIRE AND CANTILEVER ELECTROMECHANICAL SWITCHES WITH INTEGRATED PIEZORESISTIVE TRANSDUCERS,” pp. 1–4, 2013.

[38] G. Pennelli, M. Totaro, A. Nannini, U. Pisa, V. G. Caruso, and I.- Pisa, “Correlation between Surface Stress and Apparent Young ’ s Modulus of Top-Down Silicon Nanowires,” no. 12, pp. 10727–10734, 2012.

[39] M. G. Rabbani, “Unpublished,” 2011.

[40] A. S. Paulo, N. Arellano, J. a Plaza, R. He, C. Carraro, R. Maboudian, R. T. Howe, J. Bokor, and P. Yang, “Suspended mechanical structures based on elastic silicon nanowire arrays.,” *Nano Lett.*, vol. 7, no. 4, pp. 1100–4, Apr. 2007.

[41] C. O. Chui, S. Member, A. K. Okyay, and K. C. Saraswat, “Effective Dark Current Suppression With Asymmetric MSM Photodetectors in Group IV Semiconductors,” *IEEE PHOTONICS Technol. Lett.*, vol. 15, no. 11, pp. 1585–1587, 2003.

[42] T. Mizuno, S. Takagi, N. Sugiyama, H. Satake, a. Kurobe, and a. Toriumi, “Electron and hole mobility enhancement in strained-Si MOSFET’s on SiGe-on-insulator substrates fabricated by SIMOX technology,” *IEEE Electron Device Lett.*, vol. 21, no. 5, pp. 230–232, May 2000.

[43] S. E. Thompson, M. Armstrong, C. Auth, S. Cea, R. Chau, G. Glass, T. Hoffman, J. Klaus, Z. Ma, B. Mcintyre, a. Murthy, B. Obradovic, L. Shifren, S. Sivakumar, S. Tyagi, T. Ghani, K. Mistry, M. Bohr, and Y. El-Mansy, “A Logic Nanotechnology Featuring Strained-Silicon,” *IEEE Electron Device Lett.*, vol. 25, no. 4, pp. 191–193, Apr. 2004.

[44] R. He and P. Yang, “Giant piezoresistance effect in silicon nanowires,” *Nat. Nanotechnol.*, vol. 1, no. 1, pp. 42–6, Oct. 2006.

[45] E. F. Arkan, D. Sacchetto, I. Yildiz, Y. Leblebici, and B. E. Alaca, “Monolithic integration of Si nanowires with metallic electrodes: NEMS resonator and switch applications,” *J. Micromechanics Microengineering*, vol. 21, no. 12, p. 125018, Dec. 2011.

[46] B. Culshaw, “Optical fiber sensor technologies: opportunities and-perhaps-pitfalls,” *J. Light. Technol.*, vol. 22, no. 1, pp. 39–50, 2004.

[47] F. Prieto, B. Sep lveda, a Calle, a Llobera, C. Dom nguez, a Abad, a Montoya, and L. M. Lechuga, “An integrated optical interferometric nanodevice based on silicon technology for biosensor applications,” *Nanotechnology*, vol. 14, no. 8, pp. 907–912, 2003.

[48] S. P. Sundararajan, N. K. Grady, N. Mirin, and N. J. Halas, “Nanoparticle-induced enhancement and suppression of photocurrent in a silicon photodiode,” *Nano Lett.*, vol. 8, no. 2, pp. 624–30, Feb. 2008.

[49] a. Nascetti and D. Caputo, “Amorphous silicon phototransistor as nonlinear optical device for high dynamic range imagers,” *IEEE Trans. Electron Devices*, vol. 49, no. 3, pp. 395–399, Mar. 2002.

[50] A. Zhang, S. You, C. Soci, Y. Liu, D. Wang, and Y.-H. Lo, “Silicon nanowire detectors showing phototransistive gain,” *Appl. Phys. Lett.*, vol. 93, no. 12, p. 121110, 2008.

[51] I. Goykhman, B. Desiatov, J. Khurgin, J. Shappir, and U. Levy, “Waveguide based compact silicon Schottky photodetector with enhanced responsivity in the telecom spectral band,” *Opt. Express*, vol. 20, no. 27, pp. 28594–602, Dec. 2012.

[52] M. Casalino, M. Iodice, L. Sirleto, I. Rendina, and G. Coppola, “Asymmetric MSM sub-bandgap all-silicon photodetector with low dark current,” *Opt. Express*, vol. 21, no. 23, pp. 28072–28082, 2013.

[53] A. K. Okyay, C. O. Chui, and K. C. Saraswat, “Leakage suppression by asymmetric area electrodes in metal-semiconductor-metal photodetectors,” *Appl. Phys. Lett.*, vol. 88, no. 6, p. 063506, 2006.

[54] W. a. Wohlmuth, M. Arafa, A. Mahajan, P. Fay, and I. Adesida, “InGaAs metal-semiconductor-metal photodetectors with engineered Schottky barrier heights,” *Appl. Phys. Lett.*, vol. 69, no. 23, p. 3578, 1996.

[55] S. Zhu, G. Q. Lo, and D. L. Kwong, “Low-Cost and High-Speed SOI Waveguide-Based Silicide Schottky-Barrier MSM Photodetectors for Broadband Optical Communications,” *IEEE PHOTONICS Technol. Lett.*, vol. 20, no. 16, pp. 1396–1398, 2008.

[56] S. Zhu, M. B. Yu, G. Q. Lo, and D. L. Kwong, “Near-infrared waveguide-based nickel silicide Schottky-barrier photodetector for optical communications,” *Appl. Phys. Lett.*, vol. 92, no. 8, p. 081103, 2008.

[57] Z. Shiyu, H. Xia, F. Xu, and Y. Hui, “Design of Silicon Based Germanium Metal-semiconductor-metal Photodetector with Asymmetric Area Electrodes,” *Opto-electronic Eng.*, vol. 42, no. 01, 2015.

[58] S. M. Sze, “Physics of Semiconductor Devices,” *John Wiley Sons, Inc.*, no. second edition, 1981.

[59] “Atlas, Silvaco. Available: http://www.silvaco.com,” 2014. [Online]. Available: http://www.silvaco.com/.

[60] G. Larrieu and X.-L. Han, “Vertical nanowire array-based field effect transistors for ultimate scaling,” *Nanoscale*, vol. 5, no. 6, pp. 2437–2441, Mar. 2013.

[61] J.-P. Colinge, C.-W. Lee, A. Afzalian, N. D. Akhavan, R. Yan, I. Ferain, P. Razavi, B. O’Neill, A. Blake, M. White, A.-M. Kelleher, B. McCarthy, and R. Murphy, “Nanowire transistors without junctions,” *Nat. Nanotechnol.*, vol. 5, no. 3, pp. 225–229, Mar. 2010.

[62] I. Park, Z. Li, A. P. Pisano, and R. S. Williams, “Top-down fabricated silicon nanowire sensors for real-time chemical detection,” *Nanotechnology*, vol. 21, no. 1, p. 015501, Jan. 2010.

[63] G. Zheng, F. Patolsky, Y. Cui, W. U. Wang, and C. M. Lieber, “Multiplexed electrical detection of cancer markers with nanowire sensor arrays,” *Nat. Biotechnol.*, vol. 23, no. 10, pp. 1294–1301, Oct. 2005.

[64] Y. Cui, J. Wang, S. R. Plissard, A. Cavalli, T. T. T. Vu, R. P. J. van Veldhoven, L. Gao, M. Trainor, M. A. Verheijen, J. E. M. Haverkort, and E. P. A. M. Bakkers, “Efficiency Enhancement of InP Nanowire Solar Sells by Surface Cleaning,” *Nano Lett.*, vol. 13, no. 9, pp. 4113–4117, Sep. 2013.

[65] B. Tian, X. Zheng, T. J. Kempa, Y. Fang, N. Yu, G. Yu, J. Huang, and C. M. Lieber, “Coaxial silicon nanowires as solar cells and nanoelectronic power sources,” *Nature*, vol. 449, no. 7164, pp. 885–890, Oct. 2007.

[66] J. Kim, J.-H. Yun, C.-S. Han, Y. J. Cho, J. Park, and Y. C. Park, “Multiple silicon nanowires-embedded Schottky solar cell,” *Appl. Phys. Lett.*, vol. 95, no. 14, p. 143112, 2009.

[67] M. D. Kelzenberg, D. B. Turner-Evans, B. M. Kayes, M. A. Filler, M. C. Putnam, N. S. Lewis, and H. A. Atwater, “Photovoltaic measurements in single-nanowire silicon solar cells,” *Nano Lett.*, vol. 8, no. 2, pp. 710–714, Feb. 2008.

[68] F. Zhang, T. Song, and B. Sun, “Conjugated polymer-silicon nanowire array hybrid Schottky diode for solar cell application,” *Nanotechnology*, vol. 23, no. 19, p. 194006, May 2012.

[69] R. F. Pierret, *Modular series on solid state devices: Volume I: Semiconductor Fundamental*. Addison-Wesley publishing company, 1983.

[70] J. a. del Alamo and R. M. Swanson, “Modelling of minority-carrier transport in heavily doped silicon emitters,” *Solid. State. Electron.*, vol. 30, no. 11, pp. 1127–1136, Nov. 1987.

[71] M. S. Tyagi and R. Van Overstraeten, “Minority carrier recombination in heavily-doped silicon,” *Solid. State. Electron.*, vol. 26, no. 6, pp. 577–597, Jun. 1983.

[72] J. E. Allen, E. R. Hemesath, D. E. Perea, J. L. Lensch-Falk, Z. Y. Li, F. Yin, M. H. Gass, P. Wang, A. L. Bleloch, R. E. Palmer, and L. J. Lauhon, “High-resolution detection of Au catalyst atoms in Si nanowires,” *Nat. Nanotechnol.*, vol. 3, no. 3, pp. 168–173, Mar. 2008.

[73] Y. Jung, A. Vacic, D. E. Perea, S. T. Picraux, and M. a. Reed, “Minority Carrier Lifetimes and Surface Effects in VLS-Grown Axial p-n Junction Silicon Nanowires,” *Adv. Mater.*, vol. 23, no. 37, pp. 4306–4311, Oct. 2011.

[74] Y. Dan, K. Seo, K. Takei, J. H. Meza, A. Javey, and K. B. Crozier, “Dramatic reduction of surface recombination by in situ surface passivation of silicon nanowires,” *Nano Lett.*, vol. 11, no. 6, pp. 2527–2532, Jun. 2011.

[75] S. Kato, Y. Kurokawa, S. Miyajima, Y. Watanabe, A. Yamada, Y. Ohta, Y. Niwa, and M. Hirota, “Improvement of carrier diffusion length in silicon nanowire arrays using atomic layer deposition,” *Nanoscale Res. Lett.*, vol. 8, no. 1, p. 361, Jan. 2013.

[76] H. Zimmermann and H. Ryssel, “Trivalent character of platinum in silicon,” *Appl. Phys. Lett.*, vol. 58, no. 5, p. 499, 1991.

[77] M. D. Miller, “Lifetime-controlling recombination centers in platinum-diffused silicon,” *J. Appl. Phys.*, vol. 47, no. 6, p. 2569, 1976.

[78] C. France, *The Reactivity Series of Metals. Available: http://www.gcsescience.com/r1-reactivity-series-metals.htm*. 2014.

[79] M.-F. Ng, L. Y. Sim, H. Da, H. Jin, K. H. Lim, and S.-W. Yang, “Modulation of the work function of silicon nanowire by chemical surface passivation: a DFT study,” *Theor. Chem. Acc.*, vol. 127, no. 5–6, pp. 689–695, Jul. 2010.

[80] T. C. Cheng, J. Shieh, W. J. Huang, M. C. Yang, M. H. Cheng, H. M. Lin, and M. N. Chang, “Hydrogen plasma dry etching method for field emission application,” *Appl. Phys. Lett.*, vol. 88, no. 26, p. 263118, 2006.

[81] M. D. Kelzenberg, D. B. Turner-Evans, B. M. Kayes, M. a. Filler, M. C. Putnam, N. S. Lewis, and H. a. Atwater, “Single-nanowire Si solar cells,” *2008 33rd IEEE Photovolatic Spec. Conf.*, pp. 1–6, May 2008.

[82] T. Xu, Y. Lambert, C. Krzeminski, B. Grandidier, D. Stiévenard, G. Léveque, A. Akjouj, Y. Pennec, and B. Djafari-Rouhani, “Optical absorption of silicon nanowires,” *J. Appl. Phys.*, vol. 112, no. 3, p. 033506, 2012.

[83] L. Hu and G. Chen, “Analysis of optical absorption in silicon nanowire arrays for photovoltaic applications,” *Nano Lett.*, vol. 7, no. 11, pp. 3249–3252, Nov. 2007.

[84] S.-K. Kim, R. W. Day, J. F. Cahoon, T. J. Kempa, K.-D. Song, H.-G. Park, and C. M. Lieber, “Tuning light absorption in core/shell silicon nanowire photovoltaic devices through morphological design,” *Nano Lett.*, vol. 12, no. 9, pp. 4971–4976, Sep. 2012.

[85] R. a. Sinton and A. Cuevas, “Contactless determination of current–voltage characteristics and minority-carrier lifetimes in semiconductors from quasi-steady-state

photoconductance data," *Appl. Phys. Lett.*, vol. 69, no. 17, p. 2510, 1996.
[86] W. Il Park, G. Zheng, X. Jiang, B. Tian, and C. M. Lieber, "Controlled synthesis of millimeter-long silicon nanowires with uniform electronic properties," *Nano Lett.*, vol. 8, no. 9, pp. 3004–3009, Sep. 2008.
[87] B. W. Shi, H. Peng, Y. Zheng, N. Wang, N. Shang, Z. Pan, C. Lee, and S. Lee, "Synthesis of Large Areas of Highly Oriented, Very Long Silicon Nanowires," *Adv. Mater.*, vol. 12, no. 18, pp. 1343–1345, 2000.
[88] Y. Shi, Q. Hu, H. Araki, H. Suzuki, H. Gao, W. Yang, and T. Noda, "Long Si nanowires with millimeter-scale length by modified thermal evaporation from Si powder," *Appl. Phys. A*, vol. 80, no. 8, pp. 1733–1736, Feb. 2004.
[89] Y. F. Zhang, Y. H. Tang, C. Lam, N. Wang, C. S. Lee, I. Bello, and S. T. Lee, "Bulk-quantity Si nanowires synthesized by SiO sublimation," *J. Cryst. Growth*, vol. 212, no. 1–2, pp. 115–118, Jan. 2000.
[90] P. Yang, R. Yan, and M. Fardy, "Semiconductor Nanowire: What's Next?," *Nano Lett.*, vol. 10, no. 5, pp. 1529–1536, 2010.
[91] R. Yan, D. Gargas, and P. Yang, "Nanowire photonics," *Nat. Photonics*, vol. 3, no. 10, pp. 569–576, Oct. 2009.
[92] L. Zhang, X. Zhang, J. Lai, Z. Liu, S. Hou, S. Xie, and M. Gao, "Optically Powered ZnO Nanowires with Symmetric and Asymmetric Contacts," *J. Nanosci. Nanotechnol.*, vol. 13, no. 2, pp. 1203–1207, 2013.
[93] Y. Wu, H. Yan, M. Huang, B. Messer, J. H. Song, and P. Yang, "Inorganic Semiconductor Nanowires: Rational Growth, Assembly, and Novel Properties," *Chem. – A Eur. J.*, vol. 8, no. 6, pp. 1260–1268, 2002.
[94] C. M. Natarajan, M. G. Tanner, and R. H. Hadfield, "Superconducting nanowire single-photon detectors: physics and applications," *Supercond. Sci. Technol.*, vol. 25, no. 6, p. 63001, 2012.
[95] H. Bao, W. Zhang, L. Chen, H. Huang, C. Yang, and X. Ruan, "An investigation of the optical properties of disordered silicon nanowire mats," *J. Appl. Phys.*, vol. 112, no. 12, p. 124301, 2012.
[96] Y. Li, Q. Chen, D. He, and J. Li, "Radial junction Si micro/nano-wire array photovoltaics: Recent progress from theoretical investigation to experimental realization," *Nano Energy*, vol. 7, pp. 10–24, 2014.
[97] V. C. Holmberg, T. D. Bogart, A. M. Chockla, C. M. Hessel, and B. A. Korgel, "Optical Properties of Silicon and Germanium Nanowire Fabric," *J. Phys. Chem. C*, vol. 116, pp. 22486–22491, 2012.
[98] F. Leonard and A. A. Talin, "Size-Dependent Effects on Electrical Contacts to Nanotubes and Nanowires," *Phys. Rev. Lett.*, vol. 97, no. 2, p. 26804, Jul. 2006.
[99] E. Stern, G. Cheng, M. P. Young, and M. A. Reed, "Specific contact resistivity of nanowire devices," *Appl. Phys. Lett.*, vol. 88, no. 5, p. 053106, 2006.
[100] Y.-F. Lin and W.-B. Jian, "The Impact of Nanocontact on Nanowire Based Nanoelectronics," *Nano Lett.*, vol. 8, no. 10, pp. 3146–3150, 2008.
[101] M. G. Rabbani, A. Verma, M. M. Adachi, J. P. Sundararajan, M. M. Khader, R. Nekovei, and M. P. Anantram, "Modeling of dual-metal Schottky contacts based silicon micro and nano wire solar cells," *Sol. Energy Mater. Sol. Cells*, vol. 130, pp. 456–465, 2014.
[102] L. Peng, L. Hu, and X. Fang, "Energy Harvesting for Nanostructured Self-Powered Photodetectors," *Adv. Funct. Mater.*, vol. 24, no. 18, pp. 2591–2610, May 2014.

[103] K. Das, S. Samanta, P. Kumar, K. S. Narayan, and A. K. Raychaudhuri, “Fabrication of Single Si Nanowire Metal–Semiconductor–Metal Device for Photodetection,” *IEEE Trans. Electron Devices*, vol. 61, no. 5, pp. 1444–1450, May 2014.

[104] Z.-M. Liao, J. Xu, J.-M. Zhang, and D.-P. Yu, “Photovoltaic effect and charge storage in single ZnO nanowires,” *Appl. Phys. Lett.*, vol. 93, no. 2, p. 023111, 2008.

[105] Z. Bai, X. Yan, X. Chen, K. Zhao, P. Lin, and Y. Zhang, “High sensitivity, fast speed and self-powered ultraviolet photodetectors based on ZnO micro/nanowire networks,” *Prog. Nat. Sci. Mater. Int.*, vol. 24, no. 1, pp. 1–5, Feb. 2014.

[106] T. I. Kamins, R. Stanley Williams, D. P. Basile, T. Hesjedal, and J. S. Harris, “Ti-catalyzed Si nanowires by chemical vapor deposition: Microscopy and growth mechanisms,” *J. Appl. Phys.*, vol. 89, no. 2, p. 1008, Jan. 2001.

[107] A. M. Morales and C. M. Lieber, “A Laser Ablation Method for the Synthesis of Crystalline Semiconductor Nanowires,” *Science (80-.).*, vol. 279, no. 5348, pp. 208–211, Jan. 1998.

[108] X. Duan, J. Wang, and C. M. Lieber, “Synthesis and optical properties of gallium arsenide nanowires,” *Appl. Phys. Lett.*, vol. 76, no. 9, p. 1116, 2000.

[109] M. S. Gudiksen, J. Wang, and C. M. Lieber, “Synthetic Control of the Diameter and Length of Single Crystal Semiconductor Nanowires,” *J. Phys. Chem. B*, vol. 105, no. 19, pp. 4062–4064, May 2001.

[110] T. Hanrath and B. A. Korgel, “Supercritical Fluid–Liquid–Solid (SFLS) Synthesis of Si and Ge Nanowires Seeded by Colloidal Metal Nanocrystals,” *Adv. Mater.*, vol. 15, no. 5, pp. 437–440, Mar. 2003.

[111] F. M. Davidson, R. Wiacek, and B. A. Korgel, “Supercritical Fluid−Liquid−Solid Synthesis of Gallium Phosphide Nanowires,” *Chem. Mater.*, vol. 17, no. 2, pp. 230–233, Jan. 2005.

[112] F.-W. Yuan and H.-Y. Tuan, “Supercritical Fluid−Solid Growth of Single-Crystalline Silicon Nanowires: An Example of Metal-Free Growth in an Organic Solvent,” *Cryst. Growth Des.*, vol. 10, no. 11, pp. 4741–4745, Nov. 2010.

[113] V. C. Holmberg and B. A. Korgel, “Corrosion Resistance of Thiol- and Alkene-Passivated Germanium Nanowires,” *Chem. Mater.*, vol. 22, no. 12, pp. 3698–3703, Jun. 2010.

[114] A. T. Heitsch, V. A. Akhavan, and B. A. Korgel, “Rapid SFLS Synthesis of Si Nanowires Using Trisilane with In situ Alkyl-Amine Passivation,” *Chem. Mater.*, vol. 23, pp. 2697–2699, 2011.

[115] M. Brust, M. Walker, D. Bethell, D. J. Schiffrin, and R. Whyman, “Synthesis of thiol-derivatised gold nanoparticles in a two-phase Liquid–Liquid system,” *J. Chem. Soc. Chem. Commun.*, no. 7, pp. 801–802, 1994.

[116] T. D. Bogart, D. Oka, X. Lu, M. Gu, C. Wang, and B. A. Korgel, “Lithium Ion Battery Peformance of Silicon Nanowires with Carbon Skin,” *ACS Nano*, vol. 8, no. 1, pp. 915–22, Jan. 2014.

[117] Z. Zhang, K. Yao, Y. Liu, C. Jin, X. Liang, Q. Chen, and L. M. Peng, “Quantitative analysis of current-voltage characteristics of semiconducting nanowires: Decoupling of contact effects,” *Adv. Funct. Mater.*, vol. 17, pp. 2478–2489, 2007.

[118] F. Liu, L. Li, T. Guo, H. Gan, X. Mo, J. Chen, S. Deng, and N. Xu, “Investigation on the photoconductive behaviors of an individual AlN nanowire under different excited lights,” *Nanoscale Res. Lett.*, vol. 7, no. 1, p. 454, 2012.

[119] C. Kocabas, N. Pimparkar, O. Yesilyurt, S. J. Kang, M. A. Alam, and J. A. Rogers,

“Experimental and theoretical studies of transport through large scale, partially aligned arrays of single-walled carbon nanotubes in thin film type transistors.,” *Nano Lett.*, vol. 7, no. 5, pp. 1195–202, May 2007.

[120] D. P. Norton, J. D. Budai, and M. F. Chisholm, “Hydrogen-assisted pulsed-laser deposition of (001)CeO[sub 2] on (001) Ge,” *Appl. Phys. Lett.*, vol. 76, no. 13, p. 1677, 2000.

[121] W. Melitz, J. Shen, A. C. Kummel, and S. Lee, “Kelvin probe force microscopy and its application,” *Surf. Sci. Rep.*, vol. 66, no. 1, pp. 1–27, 2011.

[122] H.-Y. Tuan and B. A. Korgel, “Importance of Solvent-Mediated Phenylsilane Decompositon Kinetics for High-Yield Solution-Phase Silicon Nanowire Synthesis,” *Chem. Mater.*, vol. 20, no. 4, pp. 1239–1241, Feb. 2008.

[123] N. Mathews, B. Varghese, C. Sun, V. Thavasi, B. P. Andreasson, C. H. Sow, S. Ramakrishna, and S. G. Mhaisalkar, “Oxide nanowire networks and their electronic and optoelectronic characteristics,” *Nanoscale*, vol. 2, no. 10, pp. 1984–98, Oct. 2010.

[124] V. C. Holmberg, T. D. Bogart, A. M. Chockla, C. M. Hessel, and B. A. Korgel, “Optical Properties of Silicon and Germanium Nanowire Fabric,” *J. Phys. Chem. C*, vol. 116, no. 42, pp. 22486–22491, Oct. 2012.

[125] N. Singh, F. Y. Lim, W. W. Fang, S. C. Rustagi, L. K. Bera, a. Agarwal, C. H. Tung, K. M. Hoe, S. R. Omampuliyur, D. Tripathi, a. O. Adeyeye, G. Q. Lo, N. Balasubramanian, and D. L. Kwong, “Ultra-Narrow Silicon Nanowire Gate-All-Around CMOS Devices: Impact of Diameter, Channel-Orientation and Low Temperature on Device Performance,” *2006 Int. Electron Devices Meet.*, pp. 1–4, 2006.

[126] L. Li, C. Yang, H. Junhui, and Y. Qiaowen, “Preparation and Optoelectronic Applications of Silicon Nanowire Arrays,” *Prog. Chem. Rev.*, vol. 25, no. 0203, pp. 248–259, 2013.

[127] Z. Gao, A. Agarwal, A. D. Trigg, N. Singh, C. Fang, C.-H. Tung, Y. Fan, K. D. Buddharaju, and J. Kong, “Silicon nanowire arrays for label-free detection of DNA,” *Anal. Chem.*, vol. 79, no. 9, pp. 3291–7, May 2007.

[128] J. H. Chua, R.-E. Chee, A. Agarwal, S. M. Wong, and G.-J. Zhang, “Label-free electrical detection of cardiac biomarker with complementary metal-oxide semiconductor-compatible silicon nanowire sensor arrays,” *Anal. Chem.*, vol. 81, no. 15, pp. 6266–71, Aug. 2009.

[129] D. Dávila, a Tarancón, M. Fernández-Regúlez, C. Calaza, M. Salleras, a San Paulo, and L. Fonseca, “Silicon nanowire arrays as thermoelectric material for a power microgenerator,” *J. Micromechanics Microengineering*, vol. 21, no. 10, p. 104007, Oct. 2011.

[130] a. Stranz, J. Kähler, S. Merzsch, a. Waag, and E. Peiner, “Nanowire silicon as a material for thermoelectric energy conversion,” *Microsyst. Technol.*, vol. 18, no. 7–8, pp. 857–862, Dec. 2011.

[131] D. Shiri, A. Verma, C. R. Selvakumar, and M. P. Anantram, “Reversible modulation of spontaneous emission by strain in silicon nanowires,” *Sci. Rep.*, vol. 2, p. 461, Jan. 2012.

[132] C. Ortolland, Y. Okuno, P. Verheyen, C. Kerner, C. Stapelmann, M. Aoulaiche, N. Horiguchi, and T. Hoffmann, “Stress Memorization Technique—Fundamental Understanding and Low-Cost Integration for Advanced CMOS Technology Using a Nonselective Process,” *IEEE Trans. Electron Devices*, vol. 56, no. 8, pp. 1690–1697, Aug. 2009.

[133] A. Wei, M. Wiatr, A. Mowry, A. Gehring, R. Boschke, C. Scott, J. Hoentschel, S.

Duenkel, M. Gerhardt, T. Feudel, M. Lenski, F. Wirbeleit, R. Otterbach, R. Callahan, G. Koerner, N. Krumm, D. Greenlaw, M. Raab, and M. Horstmann, “Multiple Stress Memorization In Advanced SOI CMOS Technologies,” in *2007 IEEE Symposium on VLSI Technology*, 2007, pp. 216–217.

[134] C. Ortolland, P. Morin, C. Chaton, E. Mastromatteo, C. Populaire, S. Orain, F. Leverd, P. Stolk, F. Boeuf, and F. Arnaud, “Stress Memorization Technique (SMT) Optimization for 45nm CMOS,” vol. 51, no. c, pp. 2005–2006, 2006.

[135] V. Passi, U. Bhaskar, T. Pardoen, U. Södervall, B. Nilsson, G. Petersson, M. Hagberg, and J.-P. Raskin, “High-Throughput On-Chip Large Deformation of Silicon Nanoribbons and Nanowires,” *J. MICROELECTROMECHANICAL Syst.*, vol. 21, no. 4, pp. 822–829, 2012.

[136] C. Tuma and A. Curioni, “Large scale computer simulations of strain distribution and electron effective masses in silicon ⟨100⟩ nanowires,” *Appl. Phys. Lett.*, vol. 96, no. 19, p. 193106, 2010.

[137] M. Makeev, D. Srivastava, and M. Menon, “Silicon carbide nanowires under external loads: An atomistic simulation study,” *Phys. Rev. B*, vol. 74, no. 16, p. 165303, Oct. 2006.

[138] J. Zhang, C. Wang, R. Chowdhury, and S. Adhikari, “Small-scale effect on the mechanical properties of metallic nanotubes,” *Appl. Phys. Lett.*, vol. 101, no. 9, p. 093109, 2012.

[139] P. C. Howell, “Comparison of molecular dynamics methods and interatomic potentials for calculating the thermal conductivity of silicon,” *J. Chem. Phys.*, vol. 137, no. 22, p. 224111, Dec. 2012.

[140] J. Diao, D. Srivastava, and M. Menon, “Molecular dynamics simulations of carbon nanotube/silicon interfacial thermal conductance,” *J. Chem. Phys.*, vol. 128, no. 16, p. 164708, Apr. 2008.

[141] S. Keten, C.-C. Chou, A. C. T. van Duin, and M. J. Buehler, “Tunable nanomechanics of protein disulfide bonds in redox microenvironments.,” *J. Mech. Behav. Biomed. Mater.*, vol. 5, no. 1, pp. 32–40, Jan. 2012.

[142] Y. Y. Zhang, Q. X. Pei, and C. M. Wang, “Mechanical properties of graphynes under tension: A molecular dynamics study,” *Appl. Phys. Lett.*, vol. 101, no. 8, p. 081909, 2012.

[143] M. Hu and D. Poulikakos, “Si/Ge superlattice nanowires with ultralow thermal conductivity,” *Nano Lett.*, vol. 12, no. 11, pp. 5487–94, Nov. 2012.

[144] Y. He and G. Galli, “Microscopic Origin of the Reduced Thermal Conductivity of Silicon Nanowires,” *Phys. Rev. Lett.*, vol. 108, no. 21, p. 215901, May 2012.

[145] J. Guénolé, J. Godet, and S. Brochard, “Deformation of silicon nanowires studied by molecular dynamics simulations,” *Model. Simul. Mater. Sci. Eng.*, vol. 19, no. 7, p. 074003, Oct. 2011.

[146] Z. Yang, Z. Lu, and Y.-P. Zhao, “Shape effects on the yield stress and deformation of silicon nanowires: A molecular dynamics simulation,” *J. Appl. Phys.*, vol. 106, no. 2, p. 023537, 2009.

[147] K. Kang and W. Cai, “Size and temperature effects on the fracture mechanisms of silicon nanowires: Molecular dynamics simulations,” *Int. J. Plast.*, vol. 26, no. 9, pp. 1387–1401, Sep. 2010.

[148] T. Brun, D. Mercier, a. Koumela, C. Marcoux, and L. Duraffourg, “Silicon nanowire based Pirani sensor for vacuum measurements,” *Appl. Phys. Lett.*, vol. 101, no. 18, p. 183506, 2012.

[149] A. I. Hochbaum, R. Chen, R. D. Delgado, W. Liang, E. C. Garnett, M. Najarian, A.

Majumdar, and P. Yang, “Enhanced thermoelectric performance of rough silicon nanowires,” *Nature*, vol. 451, no. 7175, pp. 163–7, Jan. 2008.

[150] A. Agarwal, K. Buddharaju, I. K. Lao, N. Singh, N. Balasubramanian, and D. L. Kwong, “Silicon nanowire sensor array using top–down CMOS technology,” *Sensors Actuators A Phys.*, vol. 145–146, pp. 207–213, Jul. 2008.

[151] T.-M. Chang, C.-C. Weng, and M.-J. Huang, “A Nonequilibrium Molecular Dynamics Study of In-Plane Thermal Conductivity of Silicon Thin Films,” *J. Electron. Mater.*, vol. 39, no. 9, pp. 1616–1620, May 2010.

[152] H. Zhao and N. R. Aluru, “Size and surface orientation effects on thermal expansion coefficient of one-dimensional silicon nanostructures,” *J. Appl. Phys.*, vol. 105, no. 10, p. 104309, 2009.

[153] B. Hong and A. Z. Panagiotopoulos, “Molecular dynamics simulations of silica nanoparticles grafted with poly(ethylene oxide) oligomer chains,” *J. Phys. Chem. B*, vol. 116, no. 8, pp. 2385–95, Mar. 2012.

[154] N. Zhang, Q. Deng, Y. Hong, L. Xiong, S. Li, M. Strasberg, W. Yin, Y. Zou, C. R. Taylor, G. Sawyer, and Y. Chen, “Deformation mechanisms in silicon nanoparticles,” *J. Appl. Phys.*, vol. 109, no. 6, p. 063534, 2011.

[155] I. Ponomareva, M. Menon, D. Srivastava, and A. N. Andriotis, “Structure, Stability, and Quantum Conductivity of Small Diameter Silicon Nanowires,” *Phys. Rev. Lett.*, vol. 95, no. 26, p. 265502, Dec. 2005.

[156] V. Schmidt, J. V Wittemann, and U. Gösele, “Growth, thermodynamics, and electrical properties of silicon nanowires,” *Chem. Rev.*, vol. 110, no. 1, pp. 361–88, Jan. 2010.

[157] S. M. Eichfeld, M. F. Hainey, H. Shen, C. E. Kendrick, E. A. Fucinato, J. Yim, M. R. Black, and J. M. Redwing, “Vapor-liquid-solid growth of ⟨110⟩ silicon nanowire arrays,” in *SPIE NanoScience + Engineering*, 2013, p. 88200I.

[158] J. V. Wittemann, W. Münchgesang, S. Senz, and V. Schmidt, “Silver catalyzed ultrathin silicon nanowires grown by low-temperature chemical-vapor-deposition,” *J. Appl. Phys.*, vol. 107, no. 9, p. 096105, May 2010.

[159] Y. Wu, Y. Cui, L. Huynh, C. J. Barrelet, D. C. Bell, and C. M. Lieber, “Controlled Growth and Structures of Molecular-Scale Silicon Nanowires,” *Nano Lett.*, vol. 4, no. 3, pp. 433–436, 2004.

[160] Z. Huang, T. Shimizu, S. Senz, Z. Zhang, X. Zhang, W. Lee, N. Geyer, and U. Go, “Ordered Arrays of Vertically Aligned [110] Silicon Nanowires by Suppressing the Crystallographically Preferred <100> Etching Directions 2009,” no. 110, 2009.

[161] S. Plimpton, “Fast Parallel Algorithms for Short – Range Molecular Dynamics,” vol. 117, no. June 1994, pp. 1–42, 1995.

[162] J. Tersoff, “Empirical interatomic potential for silicon with improved elastic properties,” *Phys. Rev. B*, vol. 38, no. 14, pp. 9902–9905, Nov. 1988.

[163] F. de Brito Mota, J. F. Justo, and A. Fazzio, “Hydrogen role on the properties of amorphous silicon nitride,” *J. Appl. Phys.*, vol. 86, no. 4, p. 1843, Aug. 1999.

[164] P. B. Sorokin, A. G. Kvashnin, D. G. Kvashnin, J. A. Filicheva, P. V Avramov, A. S. Fedorov, and L. A. Chernozatonskii, “Theoretical Study of Atomic Structure Nanowires,” vol. 4, no. 5, pp. 2784–2790.

[165] K. Yashiro and M. Fujihara, “Molecular dynamics study on atomic elastic stiffness in Si under tension: homogenization by external loading and its limit,” *Model. Simul. Mater. Sci. Eng.*, vol. 20, no. 4, p. 045002, Jun. 2012.

[166] C. Y. Tang, L. C. Zhang, and K. Mylvaganam, “The mechanical properties of a silicon nanowire under uniaxial tension and compression 1 Introduction 2 Modelling,” no. December, 2007.

[167] K. Yamamoto, H. Ishii, N. Kobayashi, and K. Hirose, “Effects of Vacancy Defects on Thermal Conduction of Silicon Nanowire: Nonequilibrium Green’s Function Approach,” *Appl. Phys. Express*, vol. 4, no. 8, p. 085001, Jul. 2011.

[168] C. Abs da Cruz, K. Termentzidis, P. Chantrenne, and X. Kleber, “Molecular dynamics simulations for the prediction of thermal conductivity of bulk silicon and silicon nanowires: Influence of interatomic potentials and boundary conditions,” *J. Appl. Phys.*, vol. 110, no. 3, p. 034309, 2011.

[169] F. Fortuna, V. a. Borodin, M.-O. Ruault, E. Oliviero, and M. a. Kirk, “Synergetic effects of dual-beam implantation on the microstructural development in silicon,” *Phys. Rev. B*, vol. 84, no. 14, p. 144118, Oct. 2011.

[170] D. Roy, T. Keith, and J. Millam, “GaussView, Version 5,” *Semichem Inc. Shawnee Mission KS*, 2009.

[171] D. Yao, G. Zhang, G.-Q. Lo, and B. Li, “Impacts of size and cross-sectional shape on surface lattice constant and electron effective mass of silicon nanowires,” *Appl. Phys. Lett.*, vol. 94, no. 11, p. 113113, 2009.

[172] A. Henriksson, G. Friedbacher, and H. Hoffmann, “Surface modification of silicon nanowires via copper-free click chemistry,” *Langmuir*, vol. 27, no. 12, pp. 7345–8, Jun. 2011.

[173] S. Kim, M. Jo, S. Jung, H. Choi, J. Lee, M. Chang, C. Cho, and H. Hwang, “Improvement of interface quality by post-annealing on silicon nanowire MOSFET devices with multi-wire channels,” *Microelectron. Eng.*, vol. 88, no. 3, pp. 273–275, Mar. 2011.

[174] T. Tezukal, E. Toyoda, S. Nakaharai, T. Irisawal, N. Hirashital, Y. Moriyamal, N. Sugiyamal, N. Taoka, Y. Yamashita, M. Harada, T. Yamamoto, and S. Takagi, “Observation of Mobility Enhancement in Strained Si and SiGe Tri-Gate MOSFETs with Multi-Nanowire Channels Trimmed by Hydrogen Thermal Etching Mobility Characterization,” pp. 6–9, 2007.

[175] J.-M. Jancu, R. Scholz, F. Beltram, and F. Bassani, “Empirical spds* tight-binding calculation for cubic semiconductors: General method and material parameters,” *Phys. Rev. B*, vol. 57, no. 11, pp. 6493–6507, Mar. 1998.

[176] S. Datta, *Electronic Transport in Mesoscopic Systems (Cambridge Studies in Semiconductor Physics and Microelectronic Engineering)*. Cambridge University Press, 1997.